UNIVERSITÀ
DEGLI STUDI
FIRENZE

PhD in
Industrial Engineering, Curr. Science and Engineering of Materials

CYCLE XXXV

COORDINATOR Prof. Giovanni Ferrara

NANOSTRUCTURED CHIRAL MOLECULES AS SPIN FILTERS IN ELECTRON TRANSPORT PROCESSES

Academic Discipline (SSD) CHIM/03

Doctoral Candidate
Dr. Niccolò Giaconi

Supervisor
Prof. Matteo Mannini

Co-Supervisor
Prof. Lorenzo Sorace

Co-Supervisor
Dr. Lorenzo Poggini

Coordinator
Prof. Giovanni Ferrara

Years 2019/2022

Nanostructured Chiral Molecules as Spin Filters in Electron Transport Processes

October 2022, Niccolò Giaconi
PhD in Industrial Engineering, Cycle XXXV
Curr. Science and Engineering of Materials
Supervisor: Prof. Matteo Mannini
Co-supervisors: Prof. Lorenzo Sorace, Dr. Lorenzo Poggini

Università degli Studi di Firenze
P.zza San Marco 4, 50121, Firenze.

"[…] Qui, sul bordo di quello che sappiamo, a contatto con l'oceano di quanto non sappiamo, brillano il mistero del mondo, la bellezza del mondo, e ci lasciano senza fiato."

C. Rovelli, "Sette brevi lezioni di fisica", Adelphi, 2014.

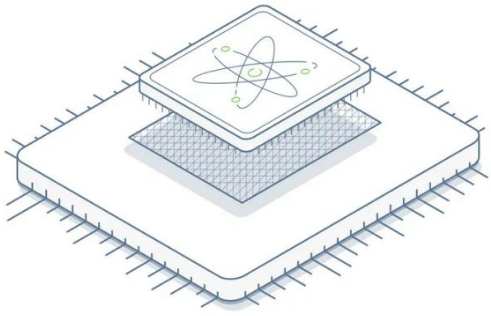

Contents

1 | Outline

The exponential growth of electronic silicon-based devices industry seen in the last decades[1] is reaching the physical limits of this technology, due to a continuous demanding of miniaturization of the devices and improvement of their performances.[2] In this scenario, moved by the need to find an alternative way to go beyond the silicon-based device limits, molecular spintronics[3] and molecular-based quantum technologies[4] have caught more and more interest. In contrast to conventional electronics, which only uses the electron's charge, spintronics processes and stores digital data using the spin as an additional degree of freedom. On the other hand, while classical informatics deals with a binary logics (*i.e.* storing and manipulating information as zero and one) the quantum computation revolution is now suggesting the possibility of using the richness of quantum states to boost data manipulation capabilities. Great expectations reside in exploiting magnetic and spin states of nanometric objects including individual molecules and atoms.[4] The initialization, control and detection of electronic spins are necessary for these new technologies.[5] In addition to inorganic materials that are employed in commonly used spintronics devices such as Hard Disk Drives,[6] also organic materials have been taken into con-

sideration due to their potential to reduce device size and to increase performances.[7,8] However, because of their relatively low efficiency for manipulating spin and charge, they were often exclusively used as spin transport channels rather than spin injectors or detectors.[9] This situation, however, has recently evolved thanks to the discovery in 1999 of the Chiral Induced Spin Selectivity (CISS) effect,[10] where effective spin conversion was detected in purely organic chiral materials. In the following years this revolutionary observation has been confirmed by several experiments and evidences, strongly indicating the presence of a connection between molecular chirality and electron's spin.[11] CISS effect may have a relevant impact considering that it might be applied in several fields such as water splitting process,[12] molecular spintronics and quantum technologies,[13] in addition to proving a possible explanation for the origin of life that is based on enantiopure biomolecules.[14] Despite a lot of efforts having been focused on this topic, much work is still needed to fully exploit the potential of CISS effect in new technologies and to have a comprehensive theoretical model capable of describing properly this phenomenon.

In this context, with this thesis I focused my attention on the preparation and characterization of nanostructured chiral molecular systems for their perspective use as spin filters. Specifically, the synthesis and the assembly on surface of compounds belonging to the class of thia[4]heterohelicenes, in both neutral and radical cation forms, were carried out with the aim of obtaining a stable molecular deposits to be studied in terms of spin selectivity of a flowing current. Spin polarization on an hybrid inorganic/organic chiral dyad was investigated as well, in order to attempt observing for the very first time the CISS effect at the molecular level. Consequently, with this work I aim to give

an insight on the CISS effect by investigating novel chiral systems featuring peculiar properties such as paramagnetism and photoinduced electron transfer processes. Results obtained in this thesis are top notch and very promising, in particular for the nanostructuration of chiral molecules and the efficiency of spin polarization attained. Those findings are fundamental to further increase the knowledge of the scientific community about CISS effect.

Chapter 2 of this thesis provides an introduction about the concept and the discovery of chirality; chirality is defined and an overview of the idea of chirality at the surface level, *i.e.* of how chirality can be imprinted on a surface, is given. Then, in Chapter 3, the state of the art about CISS effect is presented. The first observation of this effect is briefly discussed, in addition to an extensive overview on the most relevant studies reported in literature up to now. This is followed by a brief discussion of the theoretical models formulated so far to explain CISS effect, illustrating all the contributions that may give rise to this phenomenon. The general introduction reported in these chapters helps to put this PhD work in the context of current research and is conceived to ease the understanding of the key points of the experimental research described in the following chapters.

The first new results of the work are reported in Chapter 4, where the synthesis and the assembly on surface via physisorption of thia[4]helicene radical cations are described. Here, the chapter is focused on the description of the multi-technique surface characterization approach adopted. This approach uses complementary spectroscopic techniques to fully understand whether chemical structure and magnetic properties of this archetypal chiral organic radical, the synthesis of which was previously reported,[15] are retained after the deposition process. Re-

sults reported in this chapter constitute the first example of a chiral organic radical monolayer deposited on surface.
Giving continuity to the work illustrated in the previous section, Chapter 5 reports on the investigation of the spin selectivity properties of a novel thioacetyl derivative (in both neutral and radical cation forms) of the thia[4]helicene previously described. In the first part of this chapter, the synthesis procedure of this molecule is reported, followed by its deposition on a Au(111) surface to form a self-assembled monolayer chemically anchored to the metal substrate. Intriguing results regarding the occurrence of CISS effect were obtained from a collaboration with the research group of Prof. Ron Naaman at Weizmann Institute of Science in Israel, where I spent a visiting research period of 2 months. During my stay at the Weizmann Institute of Science, in addition to investigating the spin filtering behavior of these molecules, I conducted a comparative study between the neutral form and the radical cation one to investigate the role of unpaired electrons in the spin filtering process. Magnetic conductive-Atomic Force Microscopy and magnetoresistance measurements are reported in that chapter, demonstrating that high spin polarization percentages at room temperature can be achieved. The preliminary comparative studies conducted at low temperature on the radical form showed slight differences with respect to the neutral form that, however, are not sufficient to demonstrate the influence of unpaired electrons in the spin selectivity process. Further experiments are ongoing for this purpose.
Chapter 6 is devoted to the description of the first attempt to detect CISS effect at the molecular level exploiting a photoinduced electron transfer process occurring in a chiral donor-acceptor dyad. This research was realized within a collaboration between several research

groups belonging to different italian universities; my role has been here the assessment of the chemisorption of the chiral systems on the nanoparticles by performing an XPS spectroscopy characterization.
Finally, Chapter 7 briefly summarizes the obtained results and discusses the perspectives these may open.

2 | Chirality

2.1 | Origin of chirality

"*If its image in a plane mirror, ideally realized, cannot be brought to coincide with itself*"; with these words Lord Kelvin introduced for the first time the term *chirality* emphasizing the non-superposability of a chiral object and its mirror image.[16] The word *chirality* is derived from the greek $\chi\epsilon\iota\rho$ meaning "hand" and for an isolated object, for instance a molecule, that statement can be interpreted as being equivalent to requiring that the object possesses a mirror plane of symmetry or a center of inversion. Two left- and right- handed molecules feature identical physical properties (melting and boiling point, viscosity, etc.) and as long as they do not interact with a chiral system, their chemical properties are identical as well. They are identified as enantiomers of the same molecule. Traditionally, the best known type of chirality is the point chirality of a tetrahedral center with four different vertices (Figure 2.1a); there are however many potential alternative stereogenic elements that can induce chirality in molecular systems. Some examples are reported in Figure 2.1b: axial chirality, helicity (helical, propeller or inherent chirality), or desymmetrization of planar

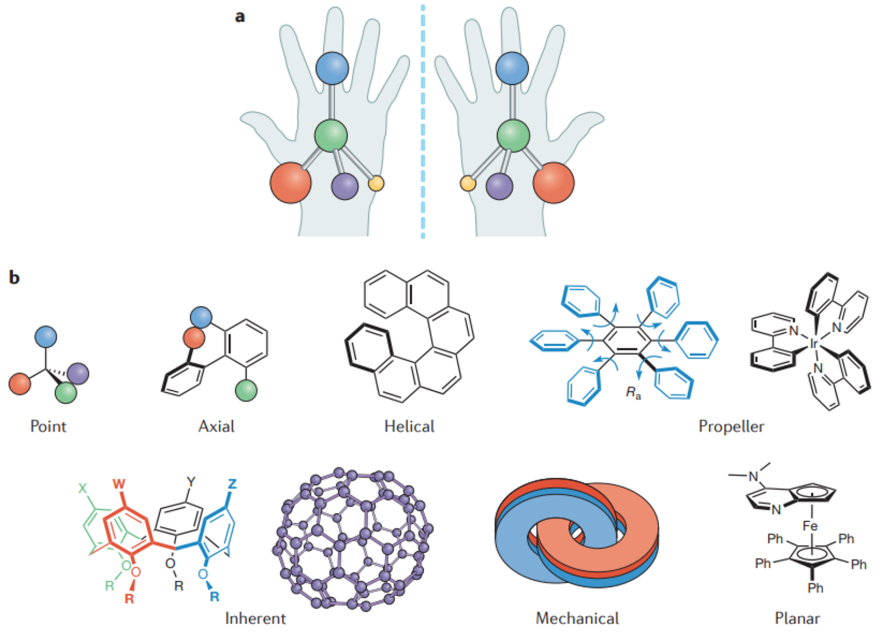

Figure 2.1: a) Point chirality in a tetrahedral center with four different vertices superimposed on hands. b) Examples of axial chirality. Reproduced from ref.[17]

system (mechanical and planar chirality).[17]

The first insight on the concept of handedness in molecular structure was provided by Louis Pasteur, who was able to find enantiomorphous crystals of tartaric acid salts. More interestingly, he observed that their solutions displayed opposite optical activity.[18] Indeed, linearly polarized light passing through a chiral medium gets rotated in opposite directions for two enantiomers, whereas the absolute value of the rotation angle is the same.[19] In quantum mechanical rotation, if we consider a linearly polarized light propagating along z axis, the initial

light state is $|\theta\rangle$, where θ is the angle of the propagation direction with respect to the x axis. Taking in consideration that any linearly polarized radiation can be written as superposition of left- ($|LCP\rangle$) and right- circularly polarized light ($|RCP\rangle$) we can describe it as follows:

$$|\theta\rangle = \frac{1}{\sqrt{2}}(e^{i\theta}|RCP\rangle + e^{-i\theta}|LCP\rangle) \tag{2.1}$$

In an optically active medium the speed of light is different for $|LCP\rangle$ and $|RCP\rangle$, thus there is a shift equal to 2δ between these components. The final beam can then be described as:

$$|\theta\rangle' = \frac{1}{\sqrt{2}}(e^{i(\theta+\delta)}|RCP\rangle + e^{-i(\theta+\delta)}|LCP\rangle) = |\theta+\delta\rangle \tag{2.2}$$

Hence, we obtain that the outgoing beam is rotated by an angle equal to δ. This is due to the interaction between the electric dipole moment of the molecule and the electric and magnetic components of the light. A dextrorotatory molecule (d isomer) promotes the flowing of the right-circularly polarized components of the light, changing the total rotation of the polarization, while the left circularly polarized component is favored by the l isomer (Figure 2.2).

Almost two centuries after Pasteur's experiment, chirality has been demonstrated to be extremely relevant in several disciplines such as chemistry, biology, biochemistry and physics[20–22] and, more generally, for several natural processes occurring on Earth, including life.[23] For instance, virtually all of the most important biomolecules are chiral, existing in enantiopure form and behaving differently. DNA is the most famous example being a right-handed helix, but also 19 of 20 natural aminoacids feature chirality and exist in the left form. The origin of

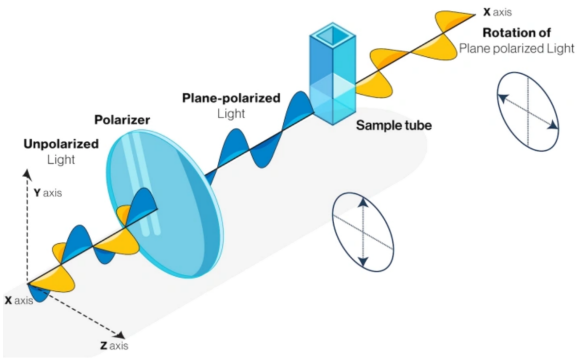

Figure 2.2: Linearly polarized light passing through a chiral medium (sample tube) gets rotated. The angle of rotation is of the same magnitude and opposite sign according to the enantiomer involved.

biological homochirality is still under open debate and a biochemical justification for the enantioselectivity of life is still missing.[24,25] At the same time, we know that two enantiomers of a given compound can feature relevantly different properties: this is *e.g.* the case of limonene, for which the *l* isomer is responsible of the smell of citrus fruit, while the *d* isomer is found in conifer, and similar differences are observed in related molecules. At the same time, chirality can affect the pharmacological activity of a molecule: this is the sad case of thalidomide. This molecule, during 50's-60's was prescribed to pregnant women as sedative. At that time it was not known that while the *l* enantiomer has the desired effect, the *d* enantiomer has a teratogenic effect, leading to malformation in embryos.[26] These are just two examples that help to emphasize the importance of the concept of chirality that indeed has been strongly promoted over the last 150 years in both organic and inorganic tridimensional systems.[27]

2.2 | Chirality on surface

In recent decades, in parallel with the development of nanotechnologies,[28] the need to study chirality at the surface level has arisen. Basically, there are several methods to imprint chirality to surfaces. At a first level a surface can be chiral simply because it is constituted by a chiral solid: this is the case of a few oxides or natural occurring minerals.[29] More interesting is the case where a chiral surface results from an achiral solid. In this case chirality may arise from superficial defects, such as specific vacancies, as well as from crystal planes that do not exhibit any mirror symmetry perpendicular to the plane, as in the case of calcite.[30] Although many metal surfaces possess symmetrical structures like face-centered (fcc), body-centered cubic (bcc) or hexagonal close-packed (hcp), chiral surfaces can be obtained by exposing planes that lack mirror symmetry. For instance, that is the case of Pt(643) or Ag(643) faces, which are chiral because of the asymmetric placement of kinks along step edges.[31,32] In a similar way this behavior has been observed also with Cu(643) which is ideally expected to feature chirality due to the presence of single atom kinks (Figure 2.3). Actually, due to the reconstruction of the surface to minimize the energy of the system, kinks and defects are particularly mobile; however by STM characterization a chiral terrace has been detected also experimentally.[33]

Efforts have been made also in imprinting chirality to a surface by building chiral nanostructures with chiral shape. As an example, Kosters *et al.*[34] developed a procedure to grow core-shell nano helices on ITO surface by electron beam induced deposition (EBID). In par-

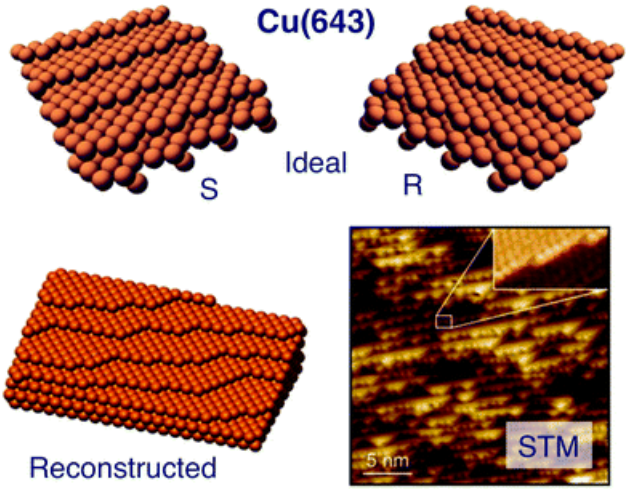

Figure 2.3: Top: ideal face-centered cubic (fcc) planes along (643) direction featuring *S*- and *R*- non-superimposable structures. Bottom: reconstruction of real surface and Cu(643) STM image. Reproduced from ref.[33]

ticular, they demonstrated that EBID is a very efficient method to fabricate complex three dimensional nanostructures with high resolution, controlling the radius and the height of the helices. In Figure 2.4a the experimental setup of the deposition technique is reported. It is based on a reaction occurring between a precursor gas and an electron beam that causes the precursor to dissociate into a volatile component and a non-volatile product which is deposited on the surface. Scanning the beam and varying the deposition parameters such as electron beam energy, current or its dwell time it is possible to control the size and the shape of the nanostructures. By performing a SEM characterization helical nanostructures are clearly visible on surface (Figure 2.4b) and it is possible to appreciate differences before and after the coating of gold performed by sputtering (Figure 2.4c). These kind of systems

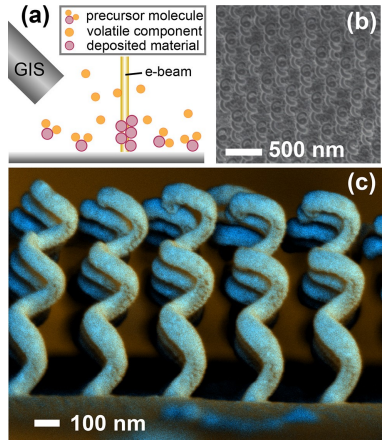

Figure 2.4: a) Representation of the EBID experimental setup. b) SEM image of nanoscale glass helices. c) SEM image of nanoscale helices coated with gold after the sputtering process. Reproduced from ref.[34]

exhibiting an enhanced local optical chirality are mainly exploited for (bio)sensing applications.

A further example of chiral nanostructures on surface has been presented by Gansel *et al.*,[35] who describe the synthesis on surface of helical structures by infilling, by electrochemical metal deposition, a polymer template made by direct laser writing (DLW). As shown in Figure 2.5 the first step of the synthetic process involves the deposition of a photoresist on a glass substrate covered with a 25 nm thin film of conductive indium-tin oxide (ITO). Then using DLW the resist is patterned with ordered helices and subsequently filled with gold by electrochemical method applying voltage between ITO and the anode immersed in the electrolyte (electroplating technique). Finally the photoresist is removed by plasma etching.

Moving toward a more "chemical" approach, chirality can be be-

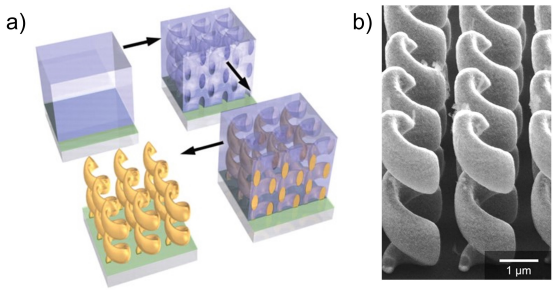

Figure 2.5: a) Synthetic route to obtain 3D gold helices on surface. A positive photoresist is placed on a glass/ITO substrate and an array of helices is printed by DLW. Then the matrix is filled with gold by an electrochemical deposition and the photoresist is removed by plasma etching to afford an array of free-standing gold helices. b) SEM image of gold helices after the removal of the polymer by plasma etching. Reproduced from ref.[35]

stowed on a surface through the adsorption of modifiers, *i.e.* molecules. Several types of systems have been studied for this purpose, like silanes, phosphonates, carboxylates, amines and thiols,[36,37] but also molecules of biological interest, such as DNA, enzymes or proteins.[38,39] In two-dimensions there are 17 space groups[40] and only five of them have no mirror symmetry perpendicular to the surface, thus admitting chirality. Moreover, because of the reduction of symmetry given by the presence of the surface, an achiral molecule in bulk phase can get a chiral nature when deposited on surface: as an example, Chen *et al.*[41] deposited glycine on a Cu(110) substrate. In a non-condensed phase, the rotation of the carboxylic group of glycine around the C-N bond has an energy barrier of 35 kJ mol^{-1}, which can be easily overcome at room temperature. As a consequence, glycine can be usually considered an achiral

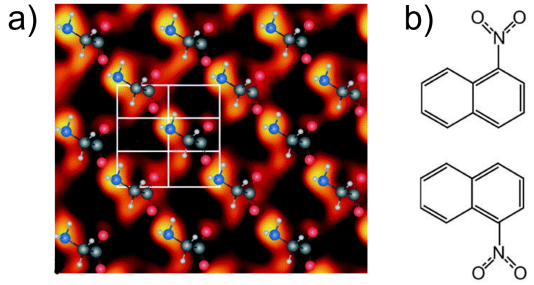

Figure 2.6: Examples of molecules that get chiral upon adsorption on surface. a) Homochiral unit cell of glycine on Cu(110) overlaying STM image. b) Nitronaphtalene configuration on substrate. Reproduced from refs.[41,42]

species. However, when adsorption takes place, "three-point" interaction with the surface via nitrogen and two oxygen atoms prevents the interconversion between the two enantiomers. Thus, a (3x2) unit cell is formed giving rise to a homochiral structure on surface (Figure 2.6a). A further example of a molecule that forms a chiral system after adsorption on surface is represented by 1-nitronapthalene.[42] Here, it is the reduction of degrees of freedom of the molecules which results in a chiral structure. Indeed, the simple combination of on-surface rotation and translation of two species does not allow a superposition. On the other hand flipping of the deposited molecules outside the plane would cause the inversion of the enantiomers (Figure 2.6b), but this cannot occur without desorption.

More easily, chirality can also be imprinted on surface by using directly chiral molecules as building blocks. An isolated molecule that features a chiral structure in bulk phase will be necessarily chiral once

assembled on surface, as long as the conformation and the structure are retained during the deposition process. The first example of a chiral molecule deposited on surface reported in literature dates back to 1978 when Somorjai *et al.* studied the adsorption of alanine on Cu(111) surface.[43] They observed that the handedness of the single enantiomer was transferred to the entire layer, therefore deducing that homochiral molecules form only one enantiomorphous domain, and the formation of the respective mirror image requires the other enantiomer. More recently another interesting example was reported by Fu and coworkers[44] on a Bis(phthalocyaninato) Tb^{3+} complex deposited on an Ir(111) surface. In this case chirality is induced by applying a bias voltage to the center of the upper Pc ligand with the STM tip, thus switching between an achiral and a chiral structure due to the misalignment between the upper and the lower ligands by an angle of ca. $\pm 4°$. Hence, it is possible to obtain both enantiomers depending on the sign of the rotation angle. In summary, they obtained a molecular switch based on a process of reversible chiralization, paving the way for what nowadays is an extremely intriguing topic, *i.e.* the correlation between magnetism and chiral structure.

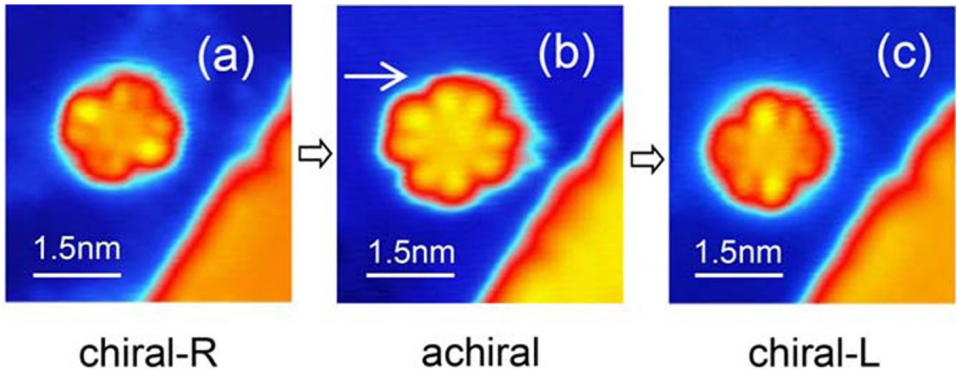

Figure 2.7: Chirality manipulation of $TbPc_2$ on Ir(111). STM images show the switching from chiral structure (a) to achiral structure (b) and a further switch toward the second structural configuration. Reproduced from ref.[44]

2.2.1 Assembly of helicenes on surface

Among all, helicenes proved to be excellent systems for investigating chiral molecules on surface as well as for chiral self-assembly at surface. As already discussed in Section 2.1, this class of compounds features as stereogenic element the helicity of the entire molecular structure. Thus, chirality is provided by the whole handedness of the molecule, while a stereogenic center is not present. This kind of molecules feature several interesting properties like optical activity and π-coniugated aromatic hydrocarbons structure that make them promising candidates for organic electronics devices. For this reason many examples of deposition on metal surface have been reported in the past. Due to the lack of polar functional groups, the deposition of helicenes on surface is often made by Ultra High Vacuum (UHV) sublimation by exploiting the interaction via van der Waals forces between molecules and the substrate.

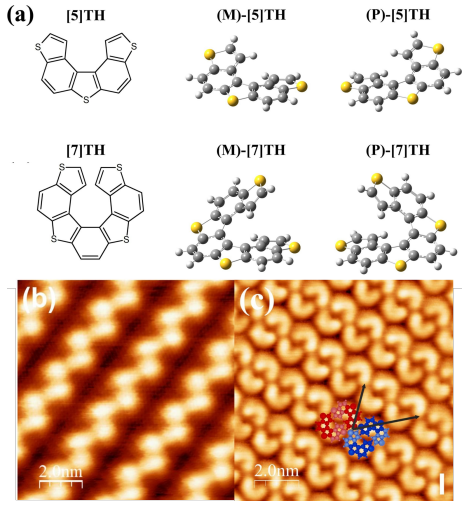

Figure 2.8: a) Molecular structure of [5] and [7] thiaheterohelicene. b) Zigzagged twin rows of rac-[7] helicene adsorbed on Ag(111). c) rac-[5] helicene forms homochiral dimers aligned on Ag(111). Reproduced from ref.[45]

As an example, recently Krukowski *et al.*[45] studied the deposition of racemic mixtures of [5] and [7] thiaheterohelicene molecules (Figure 2.8a) on Ag(111) observing the formation of highly ordered molecular monolayers. Besides, through a high resolution STM characterization they probed the handedness of the species on surface finding that depending on the number of aromatic rings of the helicene backbone, molecules assume a different pattern on surface (see Figure 2.8b for rac[7] helicene and Figure 2.8c for rac[5]helicene deposits). Indeed, [7]thiaheterohelicenes at the full coverage level tend to form just zigzagged twin rows surrounded by disordered molecular areas (Figure 2.8b). By contrast, [5]thiaheterohelicene molecules are organized predominantly into a few racemate polymorphic molecular domains at saturation coverage. The first structure is characterized by parallel rows with the preferential direction tilted from the $\langle 11\bar{2}\rangle$ direction of the Ag(111) surface by an angle of $15\pm1°$, whereas the second main structure is characterized by parallel molecular rows aligned with $\langle 11\bar{2}\rangle$ direction (Figure 2.8c). Further examples of carbohelicenes deposited on several substrates like gold, silver and copper were reported in literature[46,47] and disclosed a long range order at coverages close to the saturated monolayer. On all three (111) surfaces (Au, Ag and Cu) an STM characterization evidenced a typical three-dots appearance with symmetry *p3*-(P_3), where symbol in italics and the letter in brackets define the plane group and the enantiomeric helicene nature M- or P-, respectively. Each bright dot represents a single molecule (Figure 2.9). In the case of Cu(111) the formation of six molecules clusters, appearing either in clockwise or counterclockwise sense, nicely confirms the transmission of molecular handedness to the whole monolayer (Figure 2.9c).

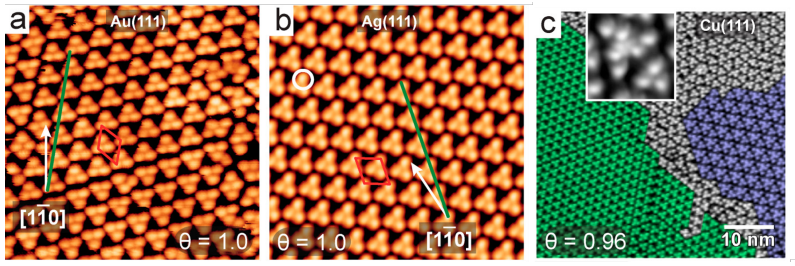

Figure 2.9: STM image (20 x 20 nm^2) of M-[7]carbohelicene monolayer on a)Au and b)Ag showing three-dots pattern. c)STM image (50 x 50 nm^2) of M-[7]carbohelicene on Cu showing the presence of six-molecules clusters pattern according to the molecular handedness. Reproduced from ref.[46,47]

While in literature there are many examples of deposition of helicenes by evaporation, only few examples of assembly from solution have been reported. For instance, Balandina *et al.*[48] investigated 5-amino[6]helicene on Au(111) deposited from a 1,2,4-trichlorobenzene (TCB) solution. In addition to observing the three-dots *p3*-(P_3) pattern for the *P* enantiomer, an homochiral long-range assembly could also be observed. At the same time the opposite enantiomer forms a mirror related *p3*-(M_3) assembly with a periodicity of (2.2 ± 0.1), identical for both enantiomers, but with inverted angles (θ) between the unit cell and the helicene trimers (Figure 2.10). In the same work the importance of the role of the solvent and of the surface in the assembly process is underlined. Indeed, a simple change of solvent from TCB to octanoic acid brings a relevant change in the molecular pattern that appears randomly distributed, without the clusters previously observed. This can be explained by the strong H-bonding occurring between the amino group of the helicenes and the carboxylic functional groups of the acid, that leads to Coulombic repulsion between charged helicenes.

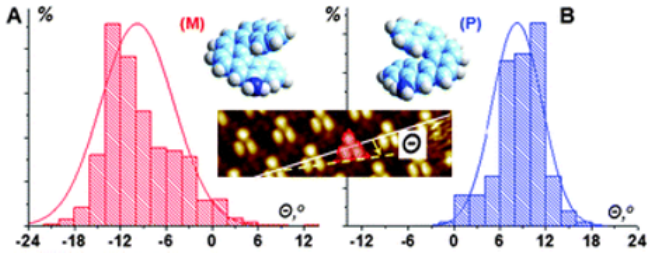

Figure 2.10: Distribution of tilt angles (θ) between the side of both a) M- and b) P-helicene trimers and the unit cell vectors.

The use of a non-metallic substrate induces the formation of disordered patterns, as well. In fact, the deposition of these molecules on HOPG gives non-stable self-assembly due to weak intermolecular interaction and low affinity with the substrate.[49]

A further example of monolayer of helicenes deposited on surface has been published by Kiran *et al.*[50] who have used a *wet chemistry* approach and a thioacetyl functional group on the helicene backbone to anchor molecules on gold (Figure 2.11a). In this case the morphological characterization does not show any ordered molecular pattern on surface. Nanolithography was used to scratch the surface and create a defined shaved area to be compared with a functionalized one, as shown in Figure 2.11b. Performing an AFM investigation, authors estimate the thickness of the adsorbate as 1.6 nm, completely comparable with the value expected for a molecular monolayer.

The importance of developing a good procedure for the deposition of chiral molecules on surface lies in the fact that to exploit all their fascinating properties it is often required to have available a well ordered system interacting with several kind of materials like metals, ferromagnets or semiconductors. Indeed, the presence of superficial

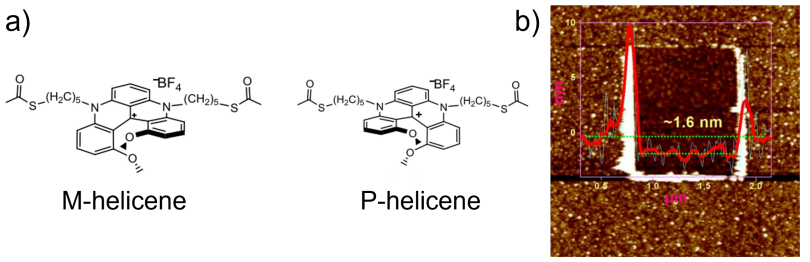

Figure 2.11: a) Molecular structures of thioacetyl functionalized M- and P-helicenes. b) AFM topography image of scratched surface with cross-sectional line profile, showing a thickness of the monolayer equal to 1.6 nm. Reproduced from ref.[50]

defects as well as the low density packing of molecules are expected to be detrimental for electron transport efficiency, in terms of current intensity and spin coherence. Among all of these properties, recently it has been observed that a chiral structure and electron spin strongly influence each other and are strictly correlated.[11] To further investigate this aspect, the assembly of molecular monolayers represents a fundamental step. This phenomenon, at the heart of this work, has been termed Chirality Induced Spin Selectivity (CISS) effect[51] and describes the capability of chiral molecules to act as spin filters for electrons discriminating these particles according to their spin state. CISS effect will be described in detail in the next chapter both from an experimental and theoretical point of view. State of the art of the research in this field will be described highlighting the results achieved so far and the major issues still outstanding in this regard.

3 | Chirality Induced Spin Selectivity

3.1 | Chirality and the electron spin

If mass and charge have been the protagonists of scientific theories in classical physics, it is only with the development of quantum mechanics that the spin or angular momentum of charged subatomic particles was recognized. Basically, for the case of electrons, the spin is associated with two states, degenerate in zero magnetic field, referred to as spin *up* or spin *down*. The degeneracy can be removed in presence of a magnetic field that splits these two states with an energy gap proportional to the magnitude of the applied field according to the Zeeman effect:[52]

$$\Delta E = g\mu_B B \tag{3.1}$$

where g is the electron Landé g-factor (2.0023), μ_B is the Bohr magneton ($9.274 \times 10^{-24} JT^{-1}$) and B is the applied magnetic field. In the field of quantum technologies, the electron spin has been thought to be exploited as data storage or computational unit. Indeed, superposition states of spin systems can be used for quantum information

and quantum computing technologies.[53] The potentiality of a quantum system for its application as qubit relies in the fact that it can be initialized in a superposition state of two basis levels ("0" and "1"). By consequence, it can be relevantly much more efficient with respect to a classical system working on a bit existing in just one state at a time.[54] However, the most critical aspect of quantum computation lies in obtaining a perfect isolation of the quantum system from the surrounding environment.[55] Any source of "noise", such as lattice vibrations, electric or magnetic fields, presence of nuclear spins or in general any uncontrolled interaction with the environment cause a loss of coherence and therefore of the processed information. The possibility to exploit the spin of electrons to store and transfer information is a fascinating perspective also from several other points of view such as low energy consumption and faster processes. A different approach to exploit electron spin for new technological applications aims to use a single spin as data storage system[56] with two states, *up* or *down*, analogous to memory units "1" and "0". Both these perspective goals require to maintain the superposition states of the spins for long distances or times, *i.e.* obtaining highly coherent spin polarized currents. Many efforts have been already done in this direction in the research field of spintronics, where the main goal is to add the electron spin as a new degree of freedom in addition to the charge to gain extra control on the system. Among all, the most common example is represented by the widely used magnetic memories, where the Giant Magneto Resistance (GMR) effect[57] is exploited to store information in nanodevices embedding ferromagnetic and non magnetic inorganic layers. Nowadays the best results in terms of performances have been obtained with inorganic materials, *i.e.* with materials having a very large spin-orbit

coupling. Although it has been demonstrated that these materials can be employed for this kind of application, an intensive research is focusing on the development of spintronic devices based on organic materials; this interest is mainly due to the inefficiency of the spin relaxation mechanism in this kind of materials.[58] Organic matter, being made by lighter elements such as nitrogen or carbon, features weak spin orbit coupling[59] and weak hyperfine interaction,[60] which are expected to be both detrimental for the spin coherence. As a consequence, the spin polarization of electrons is expected to be retained for longer times and longer distances in organic based materials than in purely inorganic ones. Further evolution has been done embedding molecules in the development of new molecular based electronic devices giving rise to the field of molecular spintronics.[61] Up to now, both organic materials and organic or metal-organic molecules have been exploited as medium to promote the transport of currents without altering their magnitude or direction.[62–64] However, in 1999 Naaman *et al.*[10] observed for the first time that chiral molecules are capable to interact with the electron spin influencing the spin polarization of a flowing current. Their discovery has opened the fascinating perspective to employ chiral organic molecules as spin filtering agents to reach values of spin polarization comparable with those obtained using inorganic materials.

3.2 | First observation of CISS effect

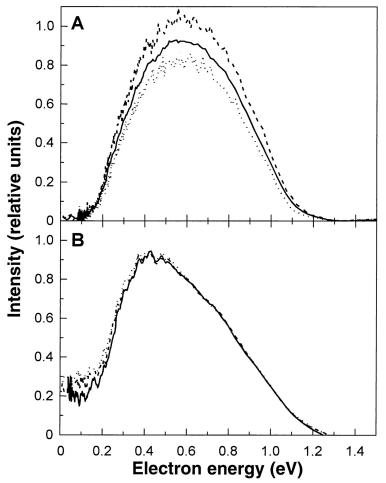

Figure 3.1: Photoemission spectra of five layers of a) L-stearoyl lysine and b) mix of D- and L-stearoyl lysine. Spectra were obtained using linearly polarized light (solid line), right (dashed line) and left (dotted line) circularly polarized light. Reproduced from ref.[10]

Naaman and coworkers investigated the asymmetric electron photoemission in a thin organized film of chiral molecules.[10] Their first study was based on L- or D-stearoyl lysine assembled on Au by Langmuir-Blodgett technique. Working on a deposit of about five monolayers, they used a laser beam at 247 nm wavelength to induce the ejection of electrons from the substrate through the stearoyl lysine. In Figure 3.1 the electron energy distribution for five layers of L-stearoyl lysine is compared with the one obtained for a mixture of D- and L-stearoyl lysine. It is evident that the yield of the electron transmission is cor-

related with the chirality of the α amino acids deposited on surface. Circularly polarized light induces a spin polarization of the photoelectron emitted by the substrate, whereas linearly polarized light does not.[65] The fact that spectra feature a different intensity of the signal by varying the polarization of the light indicates that a sort of filtering process is occurring at the interface between the metal and molecules. In particular, with L-stearoyl lysine the transport of spin up electrons is more efficient than that of the spin down electrons, being the intensity of the signal higher when right circularly polarized light is used to irradiate the sample. The spin polarization obtained in this case is about 18%. At the same time, the introduction of a minority fraction of D-stearoyl lysine in the system drastically reduces the spin filtering behavior of the molecular layer. This is due mainly to the long wavelength of the emitted electrons (ca. 2 nm for a 0.5 eV electron), which results in a coherent interaction with a large area of the sample and thus with many centers of different chirality.

3.3 | Experimental evidences of CISS effect

CISS effect has been detected initially using photoemission spectroscopy[10] and then confirmed exploiting several experimental setups.[66] The key experimental approaches used to observe CISS effect over the years will be briefly presented in the following paragraphs.

3.3.1 magnetic conductive - Atomic Force Microscopy (mc-AFM)

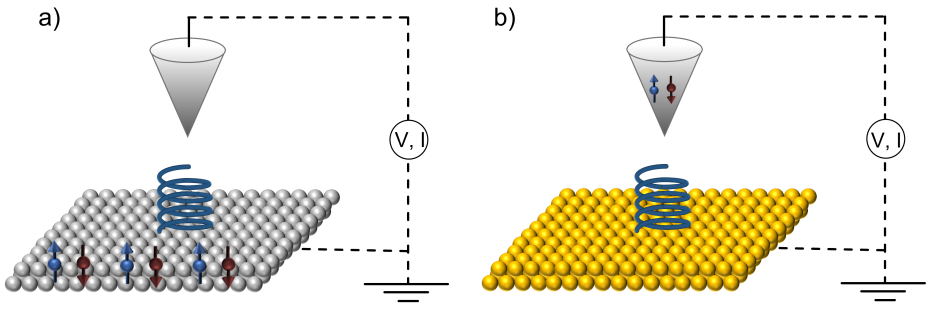

Figure 3.2: Schematization of the experimental setup of magnetic conductive- Atomic Force Microscopy (mc-AFM) with either magnetic substrate (a) or magnetic tip (b).

Magnetic conductive - Atomic Force Microscopy (mc - AFM) is one of the most common technique used to investigate the spin filtering behavior of molecular layer systems assembled on surface. Basically, this kind of experiments involves an AFM tip that is used to measure the current flowing through molecules adsorbed on a substrate either applying a negative or positive magnetic field.[67,68] The experimental setup in the studies present in literature usually involves systems with a ferromagnetic substrate (Ni) and a diamagnetic tip or conversely a diamagnetic substrate and a magnetic tip (Figure 3.2). The current vs voltage curves are measured with the magnetization pointing alternatively in both direction (up or down), aligned along the chiral axis of the molecules. What is usually observed with this type of measurement is that the intensity of the flowing current is correlated to the

magnetization direction of the substrate or of the tip, and varies its intensity according to the direction of the magnetic field.[69] Furthermore, the inversion of the handedness of the molecules causes an inversion in the intensity of the current as function of the magnetization direction as well. Essentially, molecules are acting as spin filters promoting the flowing of electrons in a certain spin state and minimizing the opposite one. In most of the cases, Ni was used as a ferromagnetic electrode. Despite being well known that, without further modification, it induces a spin polarization of about 20% at room temperature in the current,[70] in several cases the percentage measured with deposited chiral molecules was much higher, up to 80-90%. Such high values of spin polarization percentages arise from the formation of a new spin dependent interfacial coupling when depositing molecules on the substrate.[71] This spinterface[72] has new properties, which differ from the pristine separated systems. One of the first mc-AFM experiments on helicenes was reported in 2016 by Kiran *et al.*[50] In this case molecules were adsorbed on both Ni and HOPG substrates and a Fe tip was used (Figure 3.3a). In the latter case better results in terms of spin polarization percentage were obtained thanks to the higher uniformity of the deposited film.

As shown in Figure 3.3b and c the magnetization of the tip controls the conductivity of the system. A clear spin selectivity in the applied voltage range of $\pm 1V$ is evident from the different current intensity measured for different directions of the magnetic field. A direct confirmation of the CISS phenomenon was obtained by measuring the conductivity of the opposite enantiomer; here the magnetic field controls the conductivity in an opposite manner, indicating that chirality plays a role in the spin selectivity process. Further exam-

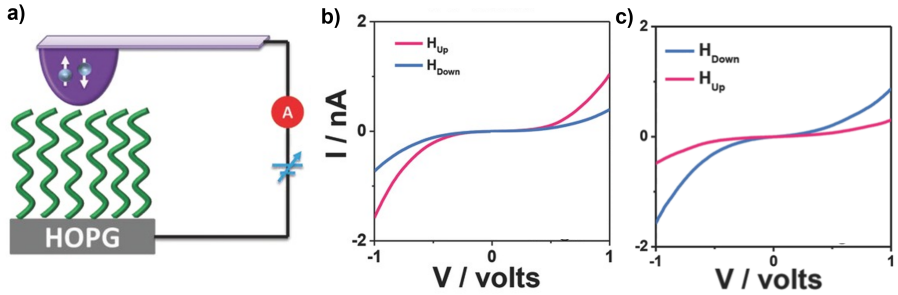

Figure 3.3: a) Schematic representation of mc-AFM experimental setup using HOPG substrate and Fe tip. b) M-Helicene and c) P-Helicene *I-V* curves obtained when tip is magnetized in up (pink) or down (blue) orientations. Reproduced from ref.[50]

ple of mc-AFM employed to investigate CISS effect was recently reported by Kulkarni *et al.*[73] on a helical π-coniugated material based on supramolecular nanofibers. They studied a supramolecular system based on coronene bisimide and tetra-amidated porphyrin cores appended with several functional groups. These building blocks are expected to form supramolecular nanofibers that exhibit helical chiral structure exploiting the π-stacking interactions between the aromatic rings. The studies were focused on these nanofibers deposited by dropcasting from diluted solution on a Ni/Au substrate. Interestingly here, mc-AFM allowed to demonstrate a strong correlation between the molecular structure of the materials, the chiral supramolecular assembly and the spin polarization efficiency. Kulkarni *et al.* demonstrated that spin selectivity can be detected on a chiral supramolecular assembly made of achiral building blocks (Figure 3.4c) and even more importantly, that the magnitude of the spin polarization is directly correlated to the optical activity of the nanofibers. In Figure 3.4b

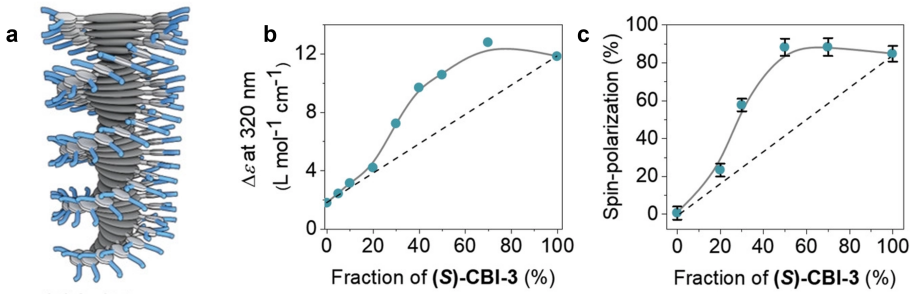

Figure 3.4: a) Schematic illustration of helical nanofiber. b) Molar circular dichroism $\Delta\epsilon$ as function of building block present in solution as measured by circular dichroism spectroscopy. c) Spin polarization percentage measured with mc-AFM at different fraction of building block. Adapted from ref.[73]

the molar circular dichroism ($\Delta\epsilon$) as a function of the supramolecular assembly in solution is reproduced; these results suggest a chiral "amplification" of the system during the process, thus indicating the growth of the helical structure. In Figure 3.4c the spin polarization percentage measured with mc-AFM on a dropcasted sample on a Au/Ni substrate is reported. A direct relationship is clearly evident between the dichroism and spin polarization trend indicating that the control on the growth of the chiral supramolecular structure can be exploited to tune the magnitude of spin polarization of helical nanofibers.

mc-AFM has proved to be a very effective technique to measure spin selectivity not only with molecular systems but also with single crystals (Figure 3.5a). For instance, Mondal *et al.*[74] measured spin dependent conduction through a copper phenylalanine crystal, Phe-Cu (Figure 3.5c). Interestingly here, what emerged from mc-AFM mea-

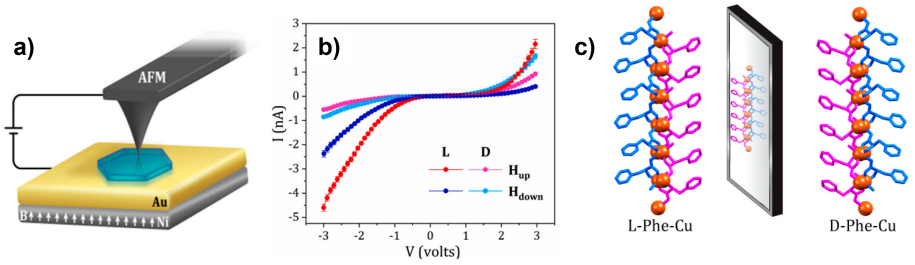

Figure 3.5: a) Experimental setup for mc-AFM measurements on Phe-Cu single crystal. b) Room temperature current-voltage measurements on L- and D-Phe-Cu single crystal as function of the applied magnetic field. c) Schematic representation of molecular structure of L- and D-Phe-Cu. Reproduced from ref.[74]

surements is the influence of the intrinsic magnetism of D-Phe-Cu and L-Phe-Cu crystals on the charge transport and spin filtering properties. Indeed, based on CISS effect the current intensity for L-enantiomer with magnetization pointing up should be equal to the intensity of D-enantiomer with magnetization pointing down. On the contrary, as shown in Figure 3.5b the current measured for L-enantiomer is generally higher with respect to the one measured for D-enantiomer. This is due to the magnetic properties of the Phe-Cu crystals. In fact, the preferred spin transport depends on the magnetization direction of the molecular magnet as well as on the chirality of the framework. Hence, the higher value of the current occurs only when both effects support the same spin preference. This aspect is interesting in the perspective of combining chirality with magnetic properties to have greater control over the spin polarization of the current.

3.3.2 Magnetotransport measurements

Molecular electronics exploits the possibility of transporting electronic charges through molecular media. The use of molecules instead of inorganic materials results in some advantages like flexibility, tunability, scalability and addressability.[75] Furthermore, by embedding molecules in an inorganic device new organic/inorganic heterojunctions can be designed. Those new architectures might feature new physical properties opening interesting perspectives for new functional devices.[76,77] In spintronics, an additional degree of freedom represented by the electron spin is introduced. Since the energy required to manipulate it is much less than that required to drive the motion of electrons, molecular spintronics[78] emerged as a new discipline, given the increasing needs for a reduction of energy consumption and, in parallel, the potential increase in the performances of new technologies based on flexibility and tunability of molecules. In traditional spintronic devices spin polarized currents are generated by ferromagnetic materials under an applied external magnetic field, making this process energetically expensive and not efficient. CISS effect thus might represent a fascinating solution to overcome this issue. Indeed, as discussed above, the use of chiral molecules can result in pure spin currents and achieve highly efficient spin injection without the need of ferromagnetic electrodes or an external magnetic field.[79] For this reason, CISS effect has been widely studied also by assembling chiral molecule-based devices for magnetoresistance measurements. The aim is to further understand the mechanism behind this phenomenon and to create a promising new generation of spintronic devices without magnetic components. Several examples are reported in literature demonstrating that chiral molecules

play an active role in influencing the magnetoresistance of the device in which they are embedded; the most recent and significant examples will be reported below. Suda *et al.*[80] studied a magnetoresistance device, *i.e.* a vertical spin valve, based on a light-driven molecular switch capable of changing the spin selectivity according to external stimuli such as light and temperature. In particular they used an overcrowded alkene (OCA, Figure 3.6a) as a molecular motor placed in a device with a ferromagnetic Ni bottom electrode and diamagnetic poly(3,4-ethylenedioxythiophene):poly(styrenesulfonate) (PEDOT/PSS) top electrode (Figure 3.6b). OCA manipulation gives rise to four switching states and two corresponding spin selectivities. In Figure 3.6c the magnetoresistance at different irradiation times with visible light is shown. At short times a clear antisymmetric curve is observed with a negative slope. As the system is irradiated an inversion of the curve occurs indicating a photoisomerization switching and thus an inversion in the spin selectivity. A similar behavior was observed with a thermal induced isomerization of OCA, obtaining an inversion of the magnetoresistance curve before and after the heating process and after light irradiation at 435 nm (Figure 3.6d).

A second example of CISS-based spintronic device involving supramolecular [6]helicene systems was recently reported by Rodriguez *et al.*,[81] who confirmed the occurrence of CISS effect by magnetoresistance measurements. In addition, this work highlights the peculiar temperature dependence of CISS effect. Rodriguez *et al.*[81] studied thick films of two different chiral supramolecular compounds (Figure 3.7a), spin coated in between Ni and Au electrodes. A typical four probe measurement in a crossbar configuration setup was then performed and the magnetoresistance curves are reported in Figure

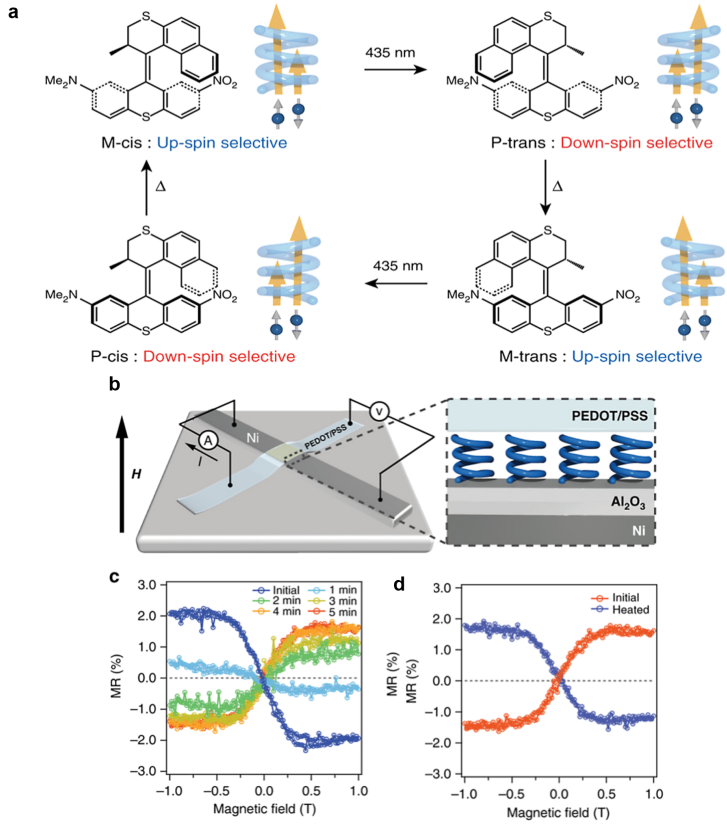

Figure 3.6: a) Molecular structure of OCA and rotation cycles with four times chirality inversions. b) Schematic representation of OCA-based device for magnetoresistance measurements. c) Magnetoresistance curves of M-cis isomer as at different irradiation time with visible light. d) Magnetoresistance curves for device with P-trans isomer before and after thermal treatment at 80° C for 12 h.Reproduced from ref.[80]

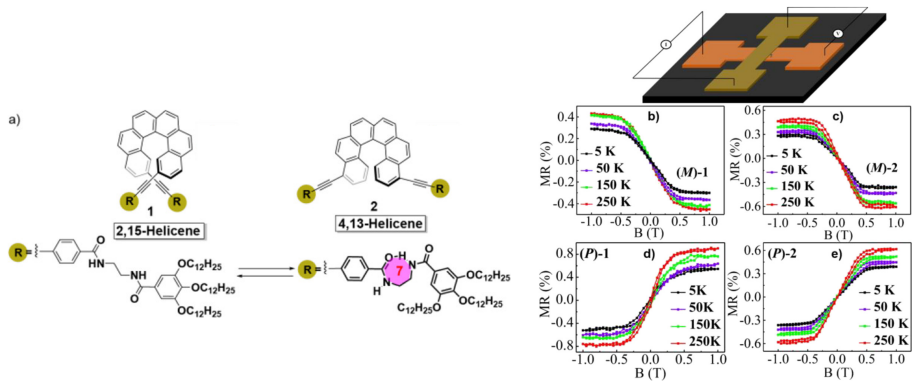

Figure 3.7: a) Molecular structure of 1,15-Helicene (1) and 4,13-Helicene (2). b) and c) Temperature dependent magnetoresistance of (M)-1 and (M)-2. d) and e) Temperature dependent magnetoresistance of (P)-1 and (P)-2. Reproduced from ref.[81]

3.7b-e. They were obtained by applying a constant current of 0.1 mA and calculating the magnetoresistance percentage as function of the applied magnetic field in the range ±1 T. It is evident that the curves are asymmetric with respect to the magnetic field and that the asymmetry depends on the handedness of the molecules involved. A step forward of this work resides in the study of the magnitude of the spin polarization as a function of the temperature: by increasing the temperature an enhancement of the spin polarization percentage was observed. This behavior was already recorded and confirmed experimentally in the past;[82–84] however, a theoretical model that properly explains and reproduces the experimental data is still lacking. In fact, the temperature dependence of CISS effect contrasts with the behavior of traditional devices that use solid-state magnetic materials, where magnetoresistance increases with decreasing temperature.

A first explanation to justify the trend observed in CISS devices considered that the conformational changes of molecules influence the conductivity of the system, when switching between secondary and tertiary structures.[85] However, this hypothesis is valid only if proteins are involved as components of the device architectures. Therefore, Sang *et al.*, after studying a Ru-modified azurin,[86] proposed that vibronically activated electronic exchange interactions could be responsible for the enhancement of the spin selectivity at room temperature. This alternative explanation introduced the concept that vibrational contribution could have a strict connection with CISS; following this, several models involving electron-phonon interaction have then been proposed. One of the most recent has been published by Fransson *et al.* in 202.,[87] In this paper it is suggested that molecular vibrations generate electron correlations that modify the electronic structure of the molecules, while interactions between electrons give rise to exchange interactions between spin channels in electron transport. In Fransson's model it is shown that electron-phonon assisted spin-orbit interactions have a relevant effect on the spin selectivity of an electron in chiral structures, making thermally activated molecular vibrations significant for the occurring of CISS.[13]

3.4 | Hall device

Another type of device that has been used to monitor the CISS effect is the Hall device. The Hall device is tipically made of GaN/AlGaN structure with a two-dimensional electron gas interface layer. This architecture is commonly used to measure the magnetic field. Indeed, once a constant current is applied between the source and the drain in

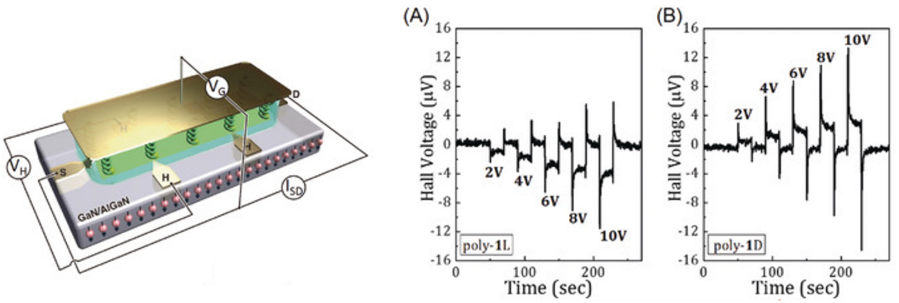

Figure 3.8: Scheme of the experimental setup of the Hall device. Hall potential recorded for a) L-polyphenylacetylene and for b) D-polyphenylacetylene. Reproduced from ref.[88]

presence of a magnetic field perpendicular to the surface of the device, due to the Lorentz force, electric potential can be measured perpendicular to the source-drain current and to the magnetic field. In their work, Mishra *et al.*[88] exploited an Hall device in absence of an external magnetic field, but with chiral polymers adsorbed on the surface (Figure 3.8). Using a gold top electrode as gate to apply an electric field the polymers get charged polarized and thus spin polarized. Therefore a magnetic field get generated and can be detected by Hall probes. Figure 3.8a and 3.8b show the Hall voltage measured as a function of the time for both the handedness of the polymer. When pulses of different voltages are applied between the gate and the Hall device, an Hall potential arises with an intensity proportional to the applied voltage. More interestingly, the sign of the Hall potential depends on the handedness of the polymers, indicating that molecules are playing a crucial role in the spin polarization process of the current.

3.4.1 Spin-dependent electrochemistry

Further experimental setup used to monitor the CISS effect in molecular monolayer is the spin-dependent electrochemistry (SDE).[89] Basically, a Au/Ni substrate functionalized with a chiral molecular layer is used as working electrode (WE) in a standard three electrodes setup for electrochemical cell with a Pt sheet and a Saturated Calomel Electrode (SCE) used as counter electrode(CE) and as reference electrode (RE), respectively. Thus, the ferromagnetic electrode coated with chiral molecules is magnetized by placing a permanent magnet underneath the substrate during the electrochemical measurement (Figure 3.9a). The spin filtering phenomenon can be then appreciated by acquiring a cyclic voltammogram (CV). By way of illustration, in Figure 3.9b the CV curves acquired by Mondal *et al.* with an electrode coated with either D- or L-Cys-TBO (cysteine-toluidine blue O) are reported.[90]

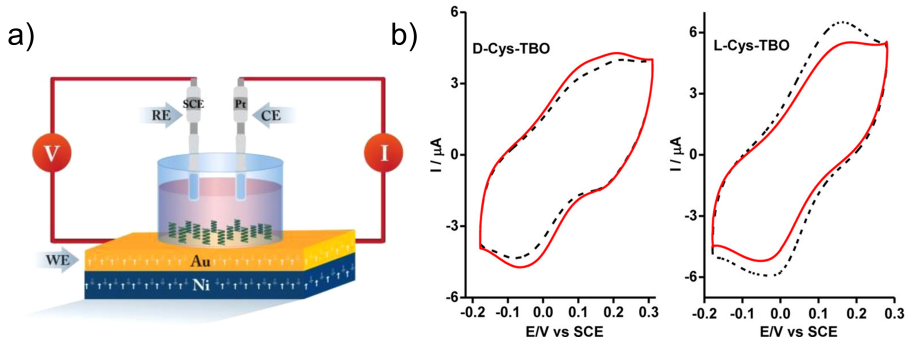

Figure 3.9: a) Schematic diagram of the SDE experimental setup. b) Cyclic voltammograms for D- and L-Cys-TBO monolayer assembled on a Ni/Au substrate. Reproduced from ref.[90]

In the first case, when the magnetization of the Ni is pointing up, toward the monolayer/solution interface, the intensity of the current is lower than when the magnetization is pointing down. On the contrary, switching the chirality of the molecular layer, the intensity of the two curves changes leading to a completely opposite behavior. This observation reveals that the electrochemical current depends on both the chirality of the cysteine linker and the magnetic field direction.
Another CISS-related electrochemical experiment worth mentioning is the one reported by Ghosh *et al.*[91] in which a chiral CuO electrode is used to reduce the formation of H_2O_2 during the water splitting process. It is well known that CuO features (photo)electrocatalytic properties for water splitting reaction.[92] In this work it was observed that a chiral CuO surface might be more efficient than achiral CuO due to the initial formation and stabilization of spin specific reaction intermediates that favor the formation of oxygen. In particular, as reported in Figure 3.10, when the spin of the OH species are parallel, can be combined to form triplet O_2 molecules. On the other hand, if they have their spin antiparallel they could combine to form either H_2O_2 or singlet O_2 species. The presence of chiral film of CuO on the electrode promotes the alignment of the spin of the OH species because of CISS effect enhancing the product of triplet species.

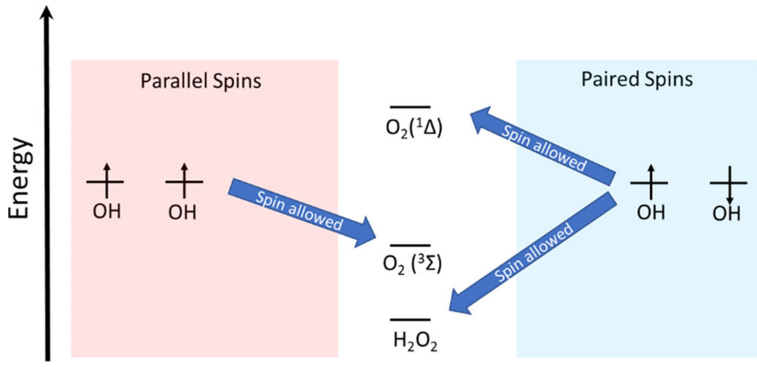

Figure 3.10: Energy diagram of the possible reactions between the hydroxyl groups on the CuO surface. Reproduced from ref.[91]

3.5 | First theoretical interpretation of CISS effect

The first theoretical model that gives a preliminary interpretation of the CISS effect was published only several years after its first experimental observation.[93] This first model considered that an electron moving along a chiral molecule experiences the electrostatic potential of the molecule, which is chiral as well. In the electron's frame, the current generates a magnetic field $\vec{B}$ that removes the degeneracy of the two spin states (Equation 3.2).

$$\vec{B} = \frac{\vec{v}}{c^2} \times \vec{E}_{chiral} \tag{3.2}$$

where $\vec{v}$ is the velocity of the electron, c is the speed of light and $\vec{E}_{chiral}$ is the electric field acting on the electron while it is moving through the chiral molecule. The term of the Hamiltonian for the spin orbit coupling can be written as:[94]

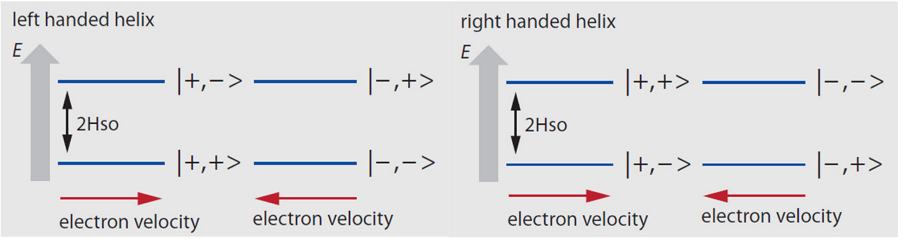

Figure 3.11: Energy scheme of an electron moving within chiral potential in both left and right handed helix. Reproduced from ref.[93]

$$H_{SO} = \lambda \vec{\sigma} \cdot (\vec{p} \times \vec{E}_{chiral}) \tag{3.3}$$

in which $\lambda = \frac{(e\hbar)}{4m^2c^2}$ is the spin-orbit coupling constant, $\vec{p}$ is the electron linear momentum, m is the mass of the electron and $\vec{\sigma}$ is a vector whose components are the Pauli matrices σ_x, σ_y and σ_z. Equation 3.3 expresses that the linear momentum and the spin of the electron are coupled, and this plays a crucial role in terms of efficiency of charge transport. Indeed, the propagating electron can be schematized as a four-states system. Each state is described by $|\vec{p}|s\rangle$ (Figure 3.11), while the energy gap between the ground and the first excited state is equal to $2H_{SO}$.

For instance, moving an electron in a left-handed helix along the positive (+) direction stabilizes the spin up state (+) while the opposite spin lies in a higher energy state. Furthermore, the $|+|+\rangle$ state is degenerate with the $|-|-\rangle$ state which corresponds to moving the electron with the opposite spin in the opposite direction. Hence, a backscattering event requires a change in both parameters, making it less probable. Since this analysis is performed considering the system

at room temperature, thermal distribution must be considered as well to evaluate the backscattering probability of electrons. Indeed, for an electron to be backscattered while retaining its spin orientation, it will have to acquire an energy that exceeds the value of $2H_{SO}$ in order to populate the first excited state. The probability that a backscattering event occurs is calculated by Equation 3.4.

$$P_{bs} = exp(-\frac{2H_{SO}}{k_B T}) \tag{3.4}$$

As an example, in DNA oligomers the H_{SO} value is of the order of 0.5 eV and only about 5% of the population will have enough energy to access to the excited state, making backscattering without spin-flipping highly improbable.

3.6 | Advanced theoretical model for CISS effect

A full theoretical comprehension of CISS effect has not yet been reached. However during the last decades several models for the spin polarization mechanism have been proposed aiming to understand the process in much greater depth if compared to the basic theoretical model described in Section 3.5. These models involve several approaches such as empirical or tight-binding Hamiltonians or in few cases DFT-based spin-dependent transport calculations.[95,96] Besides, each of them takes into account different physical contributions that may affect CISS effect. These include symmetry-breaking (time-reversal and space-inversion), intermolecular interactions, molecular spin-orbit coupling and the role of coherence in spin-polarized electron transmission. Nevertheless, a fully unifying model that includes the cooperation of all these effects

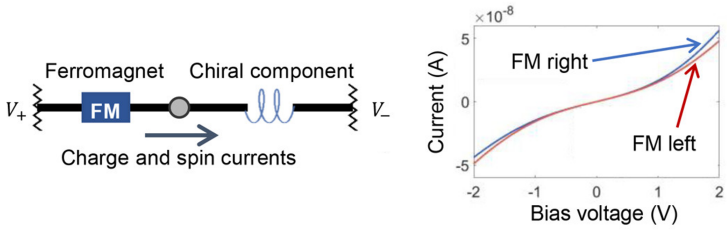

Figure 3.12: Schematic example of a two-terminal chiral-based spintronic device and spin selectivity process occurring when a bias voltage is applied. Reproduced from ref.[97]

has not been developed, yet. Below, the main contributions to the occurrence of CISS effect will be briefly described.

Symmetry breaking effects CISS effect requires the absence of both spatial and time-reversal symmetry. Indeed, the preferred spin promotion does not depend just on chirality but also on the direction of the flowing current. In addition, the spin-orbit interaction which has been demonstrated to be fundamental for CISS does not break time-reversal symmetry.[13] For these reasons, in a simple system with two leads separated by a helical structure we should not be able to observe CISS mechanism. However, as demonstrated by Yang *et al.*[97] spin selectivity can arise in a two-terminal chiral device (Figure 3.12) if the symmetry is broken leading to preferential spin direction in a chiral molecular system, and this can occur in presence of external perturbations such as an applied magnetic field, a bias voltage,[98,99] by assuming the leakage of electrons to the environment[100] or by preselection of angular momentum of injected electrons.[101]

Role of spin-orbit interaction Chiral molecules commonly studied for CISS effect are made up of light atoms, characterized by a weak spin-orbit coupling, on the order of few meV. In fact, all the models that involve spin-orbit coupling predict spin polarization percentages one order of magnitude lower than observed experimentally. Both in the gas phase and in ordered monolayers assembled on surface, the theoretical results propose up to a few percent of spin asymmetry, whereas experiments show spin polarization values above 90%. On the other hand, an experimentally confirmed prediction[102] evidenced the existence of an optimal energy windows to maximize the action of spin-orbit coupling on CISS.[103] Although experimental evidences confirm that spin-orbit coupling is a crucial ingredient for the spin polarization and its length dependence, in organic molecules it should not be sufficiently large to explain the observed spin polarization percentage. This point is one of the inconsistencies that has still to be clarified and fully understood.

Intermolecular interactions Chemical environment, and thus intermolecular interactions, can strongly influence the occurrence and the magnitude of CISS effect. It clearly comes out that relevant differences are present when gas-phase molecules are compared with high density films. In the former case, the observation of spin selectivity has been reported only once, in molecules containing heavy atoms with large spin-orbit coupling.[104] On the contrary, the organization of molecules in high density ordered films seems to increase their ability to spin filter electrons. This can be due to a delocalization of electron's wave function all over the molecular layer during the charge transport through the film. As reported in literature,[13] intermolecular

interactions are expected to act on different factors: dissipation and decoherence of the system, electron leakage to the environment and spin polarization mechanism in different regimes (*e.g.* tunneling *vs.* hopping). Medina *et al.*[105] confirmed that increasing the overlap of molecular orbitals when assembling molecules on surface could bring an enhanced spin-orbit interaction. In addition, it was recently observed that closed shell peptide helices (polyglycine $\alpha-$helix) can be readily spin polarized when assembled on a magnetized substrate in a well-packed pattern, unlike when they are isolated on surface.[106] Although this aspect is not entirely clear, it represents a key point to consider for the design and miniaturization of an efficient quantum device.

Molecule-electrode interface effect As described above, the origin of the high percentage of spin polarization observed with chiral organic molecules despite their weak spin-orbit coupling is still under open debate. Recently Liu *et al.* developed a model that takes into account the role of the substrate and of the spinterface, introducing the new concept of Orbital Polarization Effects (OPE) and proposing that the large spin-orbit coupling of the metallic electrode converts orbital polarization in spin polarization.[107] OPE means that a chiral molecule can act both as an orbital polarizer and as an orbital filter. As shown in Figure 3.13, when electrons move from a chiral molecule into the lead an orbital polarization occurs: the spin-orbit coupling therefore transform this in spin polarization. At the same time orbital filtering occurs when electrons flow from the lead into the chiral molecule because chirality filters the orbital and hence the spin through spin-orbit coupling. In summary, a helical chiral molecule which connects two leads acts as both orbital/spin polarizer and orbital/spin filter (Figure

3.13a-i). Thus, when electrons are injected in the right lead the orbital polarization induces the spin polarization (Figure 3.13a-ii). On the contrary, when electrons are injected in the chiral molecule by the left lead the orbital filter promotes the flowing of one orbital polarization and forbids the opposite one (Figure 3.13a-iii). Being the spin prelocked to the orbitals, transmitted electrons become spin polarized. Another model that involves the role played by the substrate in the spin selectivity process has been reported by Alwan and coworkers.[108] They suggest that due to an interplay between the spin-orbit coupling of the electrode and of the molecules, a solenoid field arises from electrons flowing along a chiral structure. Indeed, this field is added to the large spin-orbit coupling and interface orbital magnetization of the metallic lead, thus slightly tilting the magnetization. The tilt induces a spin torque that further tilts the magnetization. The sum of solenoid field and spin torque field yields the spin filtering phenomenon (Figure 3.13b).

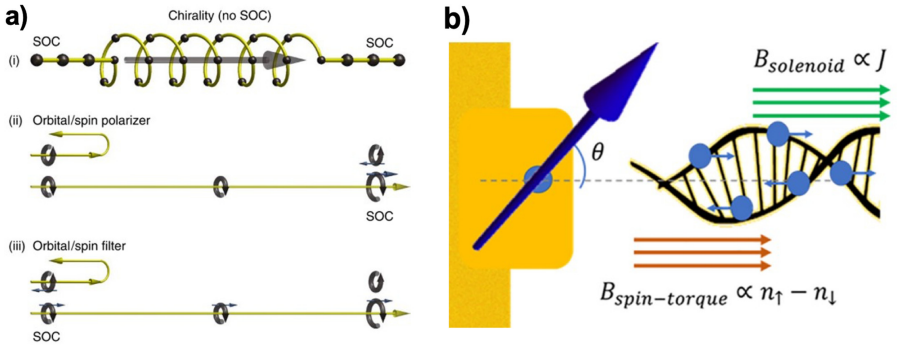

Figure 3.13: a) Thick arrows represent the $\pm L_z$ orbitals, thin arrows represent the spin. Schematization of orbital/spin polarizer and filter occurring in a system with two metallic electrodes connected by chiral bridge. b) Scheme of chiral molecule anchored on a metallic substrate. The interface orbital magnetization (blue arrow) feels two effective magnetic fields: the solenoid field and the spin-torque field. Thus, being the effective field on average nonzero it induces a Zeeman splitting and therefore a spin current through the junction. Reproduced from refs.[107,108]

The relevant studies presented in this chapter are just a minority part of the experimental evidences and theoretical models that are reported in literature about the CISS effect. Based on these and other works I planned my thesis project to enrich the current knowledge about this fascinating phenomenon and contribute to a deeper understanding of some issues still outstanding in this regard. In the next chapter the initial step that involved the nanostructuration of chiral molecules in a molecular monolayer deposited on surface will be thoroughly illustrated.

4 | The assembly of thia[4]hetero helicene radical cation

This chapter is focused on the study of the deposition of an organic radical belonging to the class of thia[4]hetero helicenes. Indeed, open-shell organic molecules constitute a remarkable platform both for the study of their fundamental properties and for applied research. Their nanostructuration is of the utmost importance for controlling and exploiting their properties at the nanoscale, either as individual objects or as an ensemble regularly arranged in 2D structures. Organic radicals have been proposed as building blocks for several multifunctional devices[109,110] and, in particular, as spin filters in molecular spintronic devices[64,111–116] because of their relatively long spin coherence length. The use of helicene radicals can bring further versatility being the paramagnetic character associated with the structural chirality of the single molecule. This opens the possibility of exploiting CISS effect to boost spin filtering efficiency as well as of modulating the CISS effect with the paramagnetic character of the radical. Herein, the synthetic route

to obtain the molecules will be illustrated first. In a second step, the bulk characterization of radical cations will be reported, in both powder and single crystal forms, exploiting Electron Paramagnetic Resonance (EPR). Finally, the development of a deposition procedure of these molecules at (sub-)monolayer coverage will be described. An extended surface sensitive characterization based on complementary techniques such as X-ray Photoelectron Spectroscopy (XPS), Time of Flight-Secondary Ion Mass Spectrometry (ToF-SIMS) and X-ray Absorption Spectroscopy (XAS) has been performed to confirm the correct assembly of molecules on surface and to demonstrate the retention of the paramagnetic properties as well as of the chiral structure after deposition on surface. The results reported in this chapter have been published in a peer-reviewed journal.[117]

4.1 | Synthesis of thia[4]hetero helicene radical cation

3,7,11-trimethylbenzo[5,6][1,4]thiazino[2,3,4-*kl*]phenothiazine radical cation (**RadE**) has been synthesized following the procedure outlined in literature by Menichetti and coworkers[15,118] and reported in Figure 4.1. This synthesis has been carried out in collaboration with Menichetti team of the Department of Chemistry "Ugo Schiff" (DICUS) of the University of Florence. The reaction of tri-*p*-tolyl amine **1.4** with two equivalents of phthalimidesulfenyl chloride (PhtNSCl) gives a bisulfenylation in *ortho* to the amine nitrogen atom (**2.4**). The electrophilic character of the sulfenamide sulfur in *N*-thiophtalimides can be increased using a Lewis acid. Indeed, by reacting derivative **2.4**

with $AlCl_3$ an intramolecular attack of the aromatic ring by the adjacent sulfur atom occurs, thus affording product **3.4** in racemic form. The one-electron chemical oxidation is then performed using $AgSbF_6$ as oxidizing agent. The reaction of **3.4** with $AgSbF_6$ in slight excess leads to the formation of metallic silver, filtered out, and the radical cation **RadE** (see Appendix A for the experimental details).

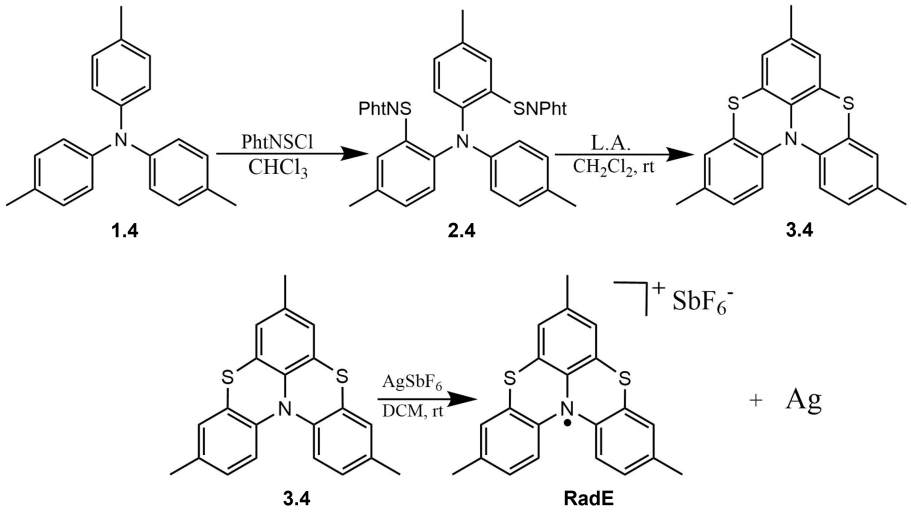

Figure 4.1: Scheme of the synthesis of thia[4]hetero helicene radical cation. Adapted from refs.[15,118]

All the following *in-house* characterization were performed on the racemic mixture of **RadE**. Enantiopure compound was used solely for the XAS characterization reported in Section 4.7.

4.2 | EPR bulk characterization

Powder and solution The X-band EPR spectra acquired on **RadE** powders features a single absorption signal with a lineshape typical of a quasi-isotropic spin 1/2 paramagnetic system (Figure 4.3a). Exchange interactions between paramagnetic centers smear out all the spectral features related to the hyperfine coupling of the unpaired electrons with nuclear spins. On the contrary, spectra acquired on a fluid solution of **RadE** in CH_2Cl_2/toluene 3:1 shows a complex hyperfine structure due to the coupling with nitrogen and hydrogen nuclear spins, as already reported in literature.[15] In Figure 4.3b the spectra obtained at 200 K and the corresponding simulation are reported. Below the freezing point of the solvent the molecules are no longer free to rotate and the line shape of the spectra evolves showing an anisotropic g tensor. The mean value, obtained by averaging the three principal values, is comparable with the observed isotropic g value in fluid solution. The spectral simulations were performed using the software *EasySpin*.[119] Hyperfine coupling between the unpaired electron and the nuclear spin of the surrounding ^{14}N (I=1) and ^{1}H atoms (Figure 4.2) were fixed adapting the values calculated in ref.,[15] while an isotropic g factor was used.

In the case of frozen solution, three components of g were used in the simulation, disregarding any hyperfine coupling which was only considered as a source of line broadening. The parameters which best reproduce the experimental spectra are reported in Table 4.1. The slight mismatch between the average of the three g components of frozen solution and the isotropic one of the fluid solution might be to

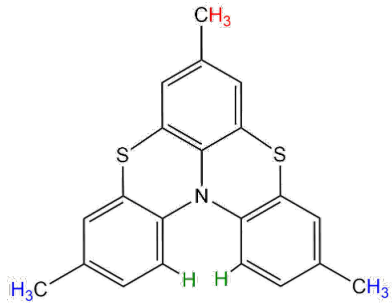

Figure 4.2: Hydrogen nuclei featuring the hyperfine coupling considered for the simulation of the fluid solution EPR spectrum

the temperature at which the latter has been acquired. Indeed, at 200 K the solvent mix CH_2Cl_2/toluene is not fully fluid, thus slowing down the motion of molecules hindering an appropriate averaging of the g tensor.

Table 4.1: g and hyperfine coupling values used for the simulations of EPR solution spectra of **RadE**. Fluid solution features an isotropic g and the spectral contribution of hyperfine coupling (color code agrees with Figure 4.2),[15] while below the freezing point any hyperfine interaction is ruled out and an anisotropic g arises.

Fluid solution g=2.0072		
Nucleus	Equivalent nuclei	A (MHz)
N	1	22.14
H	6	6.97
H	3	5.79
H	2	3.26
Frozen solution		
g_x	g_y	g_z
2.0175	2.0080	1.9935

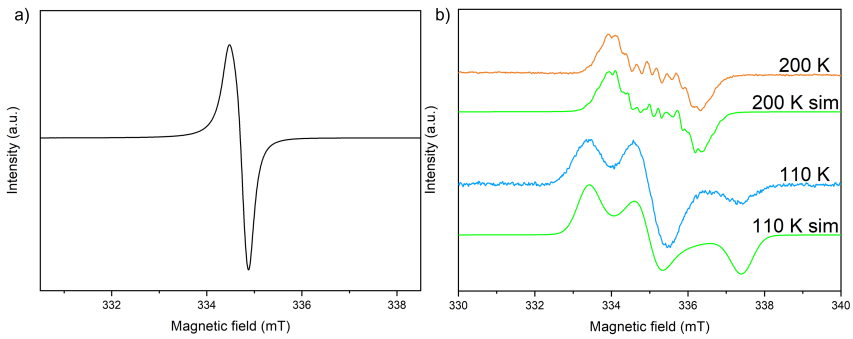

Figure 4.3: a) EPR spectrum of **RadE** powder at room temperature. b) EPR spectra of a solution of **RadE** in CH_2Cl_2/toluene 3:1 above and below the freezing point.

Single crystal Single crystals of **RadE** were grown by diffusing vapors of heptane in a solution of **RadE** in CH_2Cl_2. This allowed us to collect single crystal X-ray diffraction data: the molecules crystallize in the $P2_1/n$ monoclinic space group (Table 4.2) and the resolved molecular structure is reported in Figure 4.4.

Single crystal EPR characterization was performed with three successive rotations of a single crystal of **RadE** along three orthogonal axes xyz, with $y = b$ and x, z in the ac* plane with x rotated by -53° with respect to a; applied magnetic field was kept orthogonal to the rotation axis of the crystal (see Figure 4.5). The line shape of the spectra features a single absorption signal completely comparable with the powder spectra, thus confirming a strong exchange interaction between the paramagnetic centers also in the crystal lattice. The values of g^2 as function of the angle between the unit cell axis and the applied magnetic field, are reported in Figure 4.5. An angular dependence of g factor is clearly present for all three axes of rotation. Furthermore, the

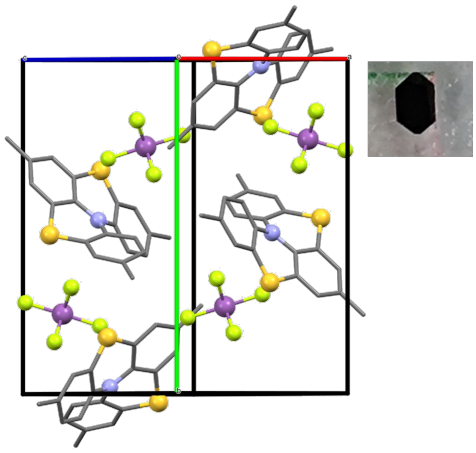

Figure 4.4: RadE crystal structure

$P2_1/n$	
a 8.40	α 90°
b 15.47	β 94°
c 16.19	γ 90°

Table 4.2: Cell parameters

symmetry of the angular dependence clearly follows the symmetry of the crystal, indicating that the magnetically nonequivalent contributions are averaged out by the exchange interactions. From this analysis it emerges that one principal direction of g lies along b' axis of the crystal lattice, as expected in monoclinic system, while the other two principal directions are forming an angle of ca. -35° with respect to the a and c* axes. Experimental data were fitted using Equations 4.1 to afford the non-diagonal g tensor expressed in the xyz reference frame.

$$\begin{aligned} g_1^2 =& g_{xx}^2 cos^2(\theta) + g_{yy}^2 sen^2(\theta) \\ &+ 2g_{xy}^2 cos(\theta) sen(\theta) \\ g_2^2 =& g_{xx}^2 cos^2(\theta) + g_{zz}^2 sen^2(\theta) \\ g_3^2 =& g_{yy}^2 cos^2(\theta) + g_{zz}^2 sen^2(\theta) \end{aligned} \tag{4.1}$$

Its principal values are $g_1 = 2.0038(2)$, $g_2 = 2.0047(3)$ and $g_3 = 2.0063(1)$ with principal directions in the xyz frame expressed by the matrix 4.2 of the direction cosines (see Figure 4.5 for a graphical representation of the orientation of the g tensor with respect to ab'c*). g_x and g_y values measured in the single crystal are lower if compared with those found in the frozen solution, whereas g_z is higher. As consequence we can deduce that the exchange interaction in the single crystal averages these components. A deeper analysis about the direction of the exchange interaction would require to know the exact orientation of the g tensor into the single molecule.

$$\begin{pmatrix} 0.3497 & 0 & 0.9368 \\ 0 & 1.000 & 0 \\ -0.9368 & 0 & 0.3497 \end{pmatrix} \tag{4.2}$$

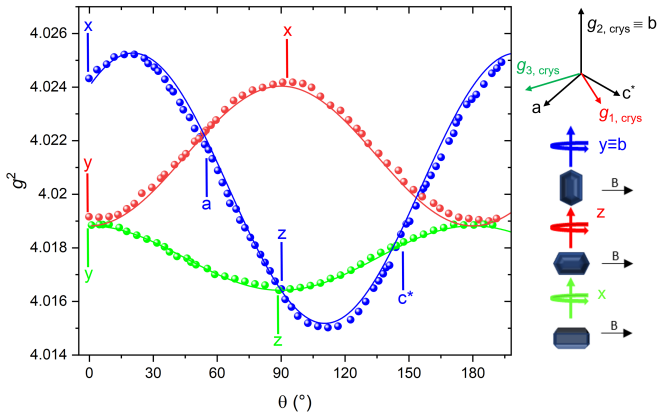

Figure 4.5: Angular dependence of g^2 value of single crystal of **RadE**.

4.3 | Assembly of RadE on thiophenol-templated Au(111)

RadE molecules were assembled on the surface using a *wet-chemistry* approach. Non-covalent interactions between molecules and substrate lead to the formation of a hierarchically self-assembled monolayer.[120,121] The substrate was obtained evaporating 120 nm of gold on a muscovite mica slab followed by hydrogen flame annealing to induce the reconstruction of the Au(111)surface.[122] After that, molecules were assembled on surface following the procedure depicted in Figure 4.6.

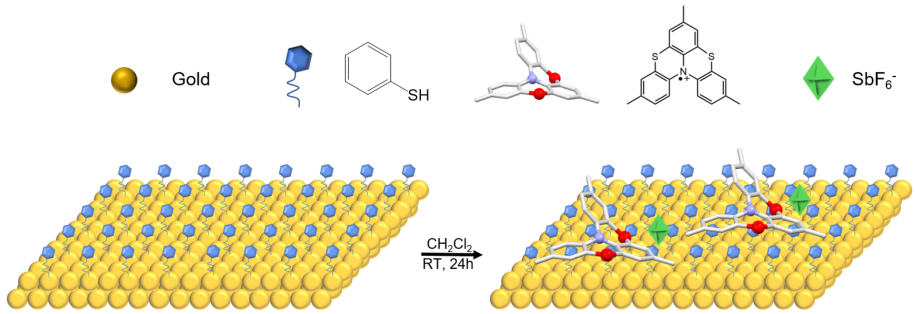

Figure 4.6: Deposition of **RadE** on thiophenol-templated Au(111). The monolayer was assembled exploiting electrostatic interactions between the positive charge of the radical cations and the electron density of the aromatic rings of the template. Color code: sulfur, red; nitrogen, violet; gold, yellow; carbon, light grey; hexafluoroantimonate, green.[117]

The first step involves the incubation of the clean substrate in a 2 mM solution of thiophenol in dry ethanol for 24 hours at room temperature to induce the formation of the thiol self-assembled monolayer.

After that, the sample is rinsed several times with clean ethanol aiming to remove molecules in excess of physisorbed material left on surface. Subsequently, the substrate is incubated again in a 2 mM solution of **RadE** in dichloromethane for additional 24 hours at room temperature. Finally, the sample was rinsed with pure CH_2Cl_2 to guarantee the correct formation of a sub-monolayer of **RadE** directly interacting with thiophenol layer. Pre-functionalization with thiophenol is here adopted to avoid the direct interaction of the helicenes with the gold surface, which was found to be detrimental.[123]

4.4 | XPS characterization of RadE assembled on Au(111)

XPS characterization of samples has been used to verify the retention of the expected chemical composition after the deposition process. The following experiment was performed on samples assembled starting from a racemic mixture of **RadE**. The most crucial information about the molecular assembly can be extracted by the analysis of the S2p XPS region (Figure 4.7) performed on bulk **RadE**, on a thiophenol monolayer (TP@Au) and on helicene radical cation assembled on the thiophenol monolayer (**RadE**_TP@Au).

RadE bulk spectra show a major component at 163.5 eV attributable to sulfur atoms of the helicene structure. On the other hand, to fit TP@Au spectra two major components are needed: one at 161.3 eV corresponding to sulfur atoms covalently bound to gold atoms of the substrate, and another one at 162.2 eV arising from physisorbed molecules left on the surface even after the rinsing procedure (ca. 32%).

A signal at higher binding energy (ca. 168 eV) is also present. This can be attributed to a minor fraction of oxidized molecules (ca. 15%), produced either during the deposition process or after exposure to the air during sample manipulation. Spectra of **RadE**_TP@Au features all the components described above. Indeed, in addition to the components attributable to thiophenol monolayer, a signal at 163.5 eV is shown confirming the presence of **RadE** on the templated surface. Using thiophenol S2p signal as an internal standard it was possible to estimate the number of molecules on the surface, thus the density packing of **RadE** monolayer. Literature reports[124] indicate a packing density of 4.3 molecule/nm^2 for a monolayer of thiophenol on Au(111). Considering that each **RadE** molecule contains two sulfur atoms and that the integral ratio of the two signals is about 5:1, we estimated a **RadE** coverage of 0.43 molecule/nm^2. According to crystallographic data,[15] each **RadE** molecule occupies a surface area of about 1.0 nm^2, thus confirming that the adopted procedure led to a sub-monolayer deposit.

N1s region was investigated as well. Nevertheless, from a qualitative point of view, this analysis did not provide any relevant information because of the sensitivity of the radical moieties to X-rays in the molecular monolayer.[125,126] The presence of nitrogen atoms in different oxidation states after exposure to X-rays and secondary electrons is indeed confirmed by the several components needed to properly fit the experimental data.

For the semi-quantitative analysis S2p, N1s and F1s regions were considered to estimate the chemical composition of **RadE** once deposited on the surface. In Table 4.3 the experimental percentages of these elements are reported. Considering the experimental error of the

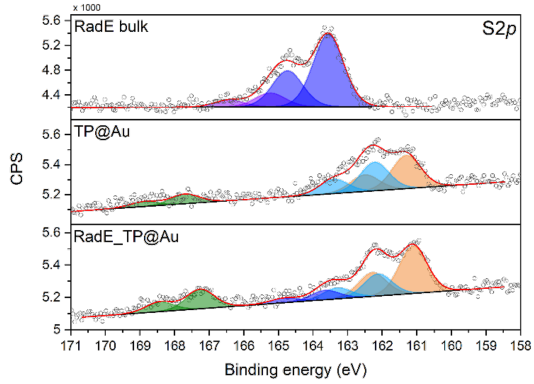

Figure 4.7: S2p XPS region of bulk **RadE**, TP@Au and **RadE**_TP@Au. Assignment of best-fitting components: S atoms of the helicene backbone: blue; S-bound Au substrate: orange; S atoms of thiophenol molecules physisorbed on the surface: cyan; S atoms oxidized after exposure to the air: green. Each signal is accompanied by its spin-orbit-coupled S2$p_{1/2}$ component shifted by 1.2 eV.[117]

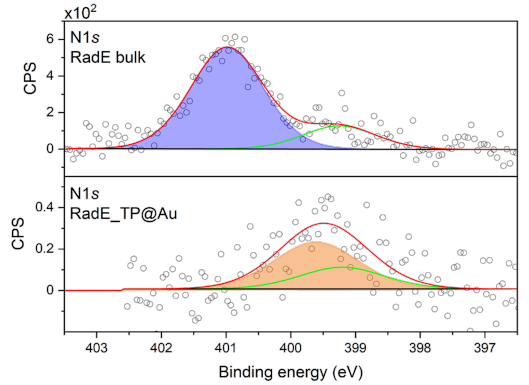

Figure 4.8: N1s regions of bulk **RadE** and **RadE**_TP@Au. After the exposure to x-rays we can observe a shift of the main nitrogen component toward lower binding energy.

XPS technique we have confirmed that the procedure adopted for the deposition preserves the molecular structure.

Table 4.3: Elemental analysis of **RadE** assembled on thiophenol-templated Au(111).

Sample	S2p [%]	N1s [%]	F1s [%]
Expected composition	22.2	11.1	66.7
Bulk	25.4 ±1.3	11.6 ±0.6	63.0 ±3.2
RadE_TP@Au	24.2 ±1.2[a]	13.5 ±0.7	62.2 ±3.1

[a] Only the contribution from **RadE** at 163.5 eV (blue component in Figure 4.7) has been included to properly evaluate the stoichiometry of the physisorbed material on top of the thiophenol monolayer.

4.5 | ToF-SIMS characterization of RadE assembled on Au(111)

To corroborate the efficiency of the deposition procedure developed and to confirm the presence of intact molecules on surface, Time of Flight- Secondary Ion Mass Spectrometry (Tof-SIMS) characterization has been performed. In a similar way to what has been done with XPS, measurements were carried out on three samples: bulk **RadE**, TP@Au and **RadE**_TP@Au. The most relevant information has been obtained by analyzing the positive ion spectra. Figure 4.9 displays the region between 300 and 360 m/z, which is expected to contain the most significant signals. In the bulk sample a high intensity main peak is present at 347 m/z, corresponding to the radical cation. Its isotopic distribution is in perfect agreement with the theoretical one. TP@Au

spectrum features a signal at 306 m/z consistent with the fragment $[C_6H_5SAu]^+$, thus confirming the formation of covalent bonds between sulfur and gold atoms. In the **RadE**_TP@Au sample, fragmentation is more pronounced than in the bulk sample and a larger number of signals are present. In particular, the spectrum is dominated by signals at high m/z values, due to the fluorine-containing fragments related to the counterion. It is important to highlight here that, despite their lower intensity, peaks related to **RadE** and TP@Au are still detectable, thus confirming that the helicene and the pristine passivating agent of the gold surface are intact. Table 4.4 summarizes the assignment of positive-ion peaks.

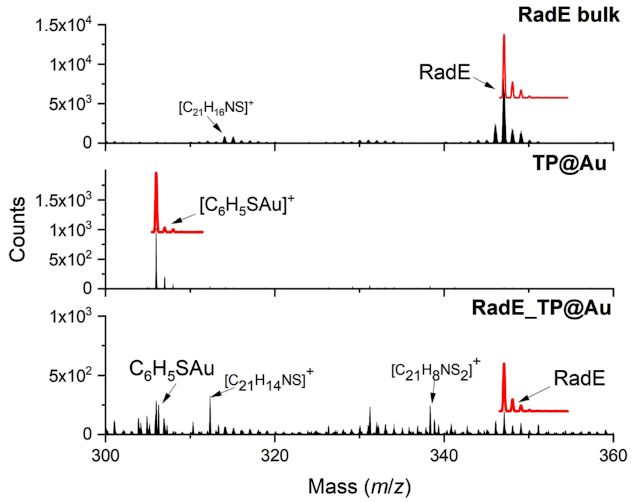

Figure 4.9: ToF-SIMS positive-ion spectra of bulk **RadE**, TP@Au and **RadE**_TP@Au in the region m/z=300 to 360. Red lines above the experimental data represent the theoretical isotopic distribution of the most significant peaks.

Table 4.4: Most relevant peaks in positive-ion ToF SIMS spectra recorded on bulk **RadE**, TP@Au and **RadE**_TP@Au.

Assignment	Bulk	Int.	TP@Au	Int.	**RadE**_TP@Au	Int.
$[C_6H_6S]^+$			110	*w*	100	*m*
$[C_7H_5S]^+$	121	*vw*				
$[C_{14}H_{11}NS]^+$	225	*vw*			225	*m*
$[C_{14}H_{10}NS_2]^+$	256	*vw*			256	*w*
$[C_6H_5SAu]^+$			306	*s*	306	*w*
$[C_{21}H_{14}NS]^+$					312	*w*
$[C_{21}H_{16}NS]^+$	314	*w*				
$[C_{20}H_{12}NS_2]^+$	330	*m*			330	*w*
$[C_{21}H_8NS_2]^+$					338	*w*
$[C_{21}H_{17}NS_2]^+$	347	*s*			347	*w*
$[C_{21}H_{17}NOS_2]^+$	363	*w*				
$[C_{21}H_{15}NS_2F]^+$					364	*w*
$[C_{21}H_{15}NO_2S_2]^+$	377	*vw*				
$[C_{21}H_{15}NS_2F_2]^+$					383	*w*
$[C_{22}H_{15}NS_2F_2]^+$					395	*w*
$[C_{19}H_{13}AuNS_2]^+$	516	*vw*				
$[C_{21}H_{17}AuNS_2]^+$	544	*vw*				

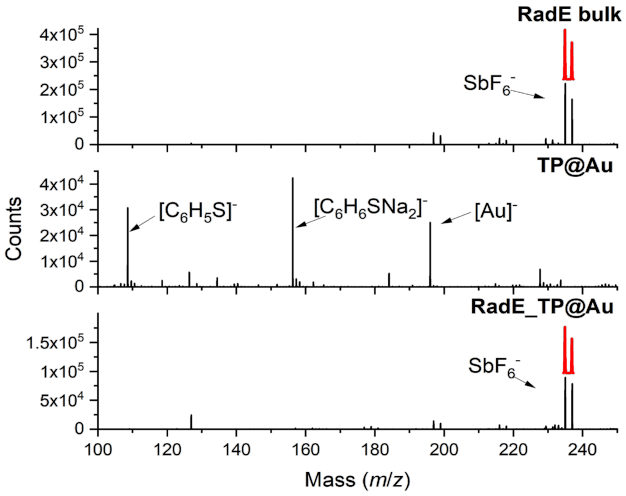

Figure 4.10: ToF-SIMS negative-ion spectra of bulk **RadE**, TP@Au and **RadE**_TP@Au in the region m/z=100 to 250. Red lines above the experimental data represent the theoretical isotopic distribution of the most significant peaks.

Relevant information can be extracted from the negative-ion spectra as well (Figure 4.10). In bulk sample only an intense signal is detected at 234 m/z, assigned to the counterion SbF_6^-. For the TP@Au sample, in agreement with a previous report[127] on a thiophenol self-assembled monolayer, signals arising from clusters with the general formula $[(C_6H_5S)_nAu_{n-1}]^-$ (n=1-4) are observed. **RadE**_TP@Au spectrum shows only one significant peak of SbF_6^- at 234 m/z. The observation of both counterion and radical cation peaks in negative- and positive-ion spectra, respectively further confirms the presence of **RadE** assembled on top of thiophenol layer.

4.6 | EPR characterization on RadE assembled on Au(111)

Cw-EPR spectroscopy at X-band was exploited to verify the retention of paramagnetic properties of **RadE** once assembled on surface and to obtain information about the interactions among unpaired electrons within the monolayer. Despite the low amount of material (ca. 10^{13} spins), which is close to the sensitivity limit of the technique, it has been possible to collect meaningful spectra at low temperature. In the spectra acquired on **RadE**_TP@Au sample, one intense absorption signal is present, closely resembling the EPR spectrum of the powder sample (Figure 4.11a). Both the EPR spectrum of a fluid solution of **RadE** (described in Section 4.2), featuring a complex hyperfine structure, and that of a frozen solution, characterized by a well-resolved g anisotropy, strongly differ from the one observed here. This indicates that, when the molecules are assembled in the monolayer, the 2D intermolecular exchange interaction is strong enough to smear out the hyperfine structure and average out the anisotropic features.[128] The similarity with powder spectra suggests a comparable magnitude of intermolecular exchange interactions in the solid state and on surface. On the other hand, angular-dependent measurements of the SAM spectrum did not provide any evidence of a clear variation with field orientation (Figure 4.11b). Since single crystal spectra of the pure sample shows the persistence of angular dependence, any long-range structural order in the SAM can be ruled out.

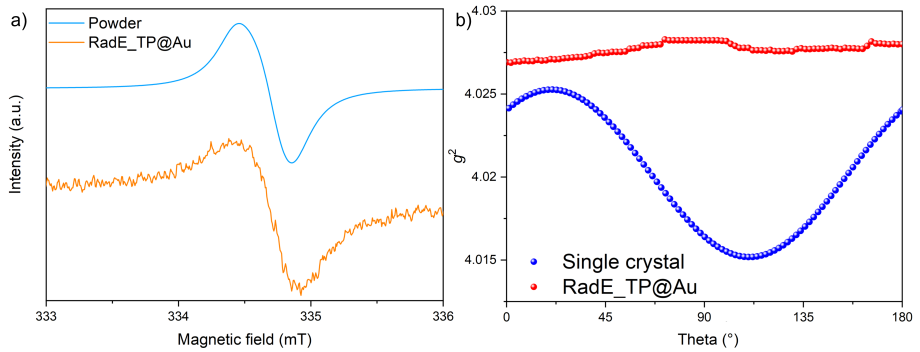

Figure 4.11: a) X-band cw-EPR spectra of **RadE** powder (blue) and **RadE**_TP@Au (orange) at 30 K. b) g^2 angular dependence of **RadE** single crystal around monoclinic b axis and of **RadE**_TP@Au.

4.7 | XAS characterization of RadE assembled on Au(111)

Once the feasibility of **RadE** assembling on surface was demonstrated, the same procedure was adopted to deposit enantiopure compounds, namely (P)- and (M)-**RadE** (see inset Figure 4.12b), obtained by separation using HPLC equipped with chiral stationary phase.[129] To demonstrate the retention of molecular chirality on surface, the prepared samples were investigated by exploiting large scale facilities, *i.e.* synchrotron light. In particular, an X-ray Natural Circular Dichroism (XNCD) experiment was performed. This technique has turned out to be an excellent choice to investigate chirality at the nanoscale.[130] Indeed, the selectivity of the core electron excitation allows investigation of the contribution of each element to the chirality of the molecule.

Furthermore, the high surface sensitivity allows to investigate very small amounts of molecules. Here, absorption spectra were acquired at the carbon K-edge since the chiral character of **RadE** lies mainly in the carbon atoms that constitute the helical structure of the molecule. From literature reports on other chiral systems,[131] we expected to obtain different absorption contributions under circularly polarized light according to the handedness of the helix. The isotropic XAS spectra has been obtained by averaging the circular absorption cross-section of left (σ^L) and right (σ^R) circularly polarized light for both enantiomers. All the measurements were performed at 100 K to minimize the radiation damage. From Figure 4.12a it is possible to appreciate spectral features attributable to both the C1$s\rightarrow$ σ^* transition at about 289.4 eV and to the C1$s\rightarrow$ π^* transition at lower energy. In Figure 4.12b the XNCD signal, evaluated as $\sigma^L - \sigma^R$, is reported. To remove the contribution of the adventitious carbon present in the beamline optical path, each signal was normalized by using a reference XAS spectrum acquired on a freshly sputtered gold substrate. Thus, each measurement was repeated twice, first monitoring the I/I_0 on the real sample and then repeating the same measurements on the Au single crystal. Finally, a ratio between the spectra acquired on the sample and on the gold reference has been adopted as the final spectrum for each polarization. It is evident that the two samples prepared by using the two different enantiomers show a dichroism of the same magnitude and opposite sign. This indicates that the handedness of molecules is retained on surface, in agreement with the relatively high racemization barrier reported in literature.[118,129] In addition, the most intense signals at about 284 eV and 286.2 eV show a surprisingly high percentage of XNCD accordingly to the normalization procedure described

above. We can hypothesize that such high dichroism might be due to the chiral character being spread all over the molecular structure of the helicene,[130] in contrast to systems where chirality is limited to a single stereogenic center.[131] The occurrence of this strong effect could be due also to a spin filtering process caused by selective electron emission induced by the chiral structure, in a similar way to what was reported by Dor *et al.*[132] for a polypeptide monolayer embedded in a hybrid system with quantum dots on a Ni surface. Although a complete understanding of this phenomenon will require further investigation, here the major result is the unambiguous detection of chirality at the submonolayer level.

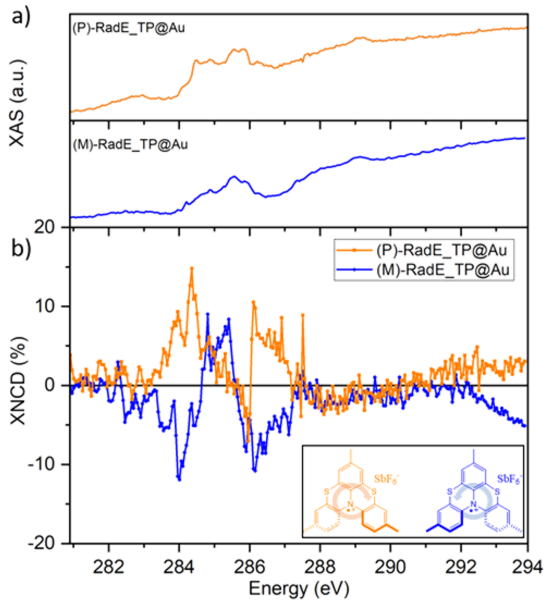

Figure 4.12: a) Isotropic XAS spectra at 100 K at the carbon K edge of (P)- and (M)-**RadE**_TP@Au. b) XNCD spectra of the two enantiopure samples. Inset: molecular structures of (P)- and (M)-**RadE**.[117]

In conclusion, the study reported in this chapter has led to the development of a deposition procedure of a monolayer of paramagnetic enantiopure thia[4]helicene radical cations on surface. A thorough characterization of a (sub-)monolayer of these molecules assembled on thiophenol-templated Au(111) has been presented demonstrating the retention of the chemical structure and the magnetic properties after the deposition process. By exploiting complementary characterization techniques such as XPS and ToF-SIMS the integrity of the helicenes on surface was confirmed, while the proof of the persistence of the radical character was provided by EPR characterization. Finally, an unprece-

dented use of X-ray Natural Circular Dichroism (XNCD) technique to probe chirality has been reported, detecting chiral structure on a sub-monolayer deposit. This in-depth investigation thus demonstrated the success of the assembly procedure of chiral radicals with specific handedness on surface. These results open novel perspectives in the use of organic radicals for the development of molecular-based spintronic devices and represent a fundamental step in the rational design of a new spinterface, the active interlayer in molecular spintronic devices, in which chiral paramagnetic molecules are embedded to gain extra control over spin injection processes.

5 | Thioacetyl thia[4]hetero helicene chemisorbed on surface

The results reported in Chapter 4 proved the stability of the helicene radical **RadE** on surface, with regard to both its chirality and paramagnetic properties, when it is deposited on a templated layer.[117] The following step has been directed toward the understanding of the spin filtering properties of this class of compounds. In this perspective, a neutral thioacetyl derivative of the previous molecular system has been synthesized, to allow the chemical anchoring of the helicene on surface and thus to obtain an even more stable system. A self-assembled monolayer has been prepared by using the deposition procedure developed for the system described in the previous chapter. The obtained sample has been characterized by XPS to confirm that it is feasible to assemble these molecules on surface via covalent interactions. After this, I went for a visiting research period at Weizmann Institute of Science in Israel where, hosted in Prof. Ron Naaman's group, I studied the spin selectivity properties of the helicene monolayer by magnetic-conductive

Atomic Force Microscopy (mc-AFM) and by magnetoresistance measurements on a molecular-based spintronic device. In both experiments the electron conduction proved to be highly dependent on the handedness of molecules involved, proving the active role played by chirality in the spin selectivity process. Furthermore, in the case of mc-AFM experiment, a surprisingly high value of spin polarization percentage has been detected in an incredibly small range of applied voltage.
Besides, a chemical oxidation using $AgSbF_6$ has afforded the corresponding radical cation of the helicene, analogously to **RadE** species. Thus, an EPR characterization has been performed on the bulk radical form before depositing it on surface for XPS measurements. Finally, aiming to understand if the presence of unpaired electrons can influence the spin polarization process by exchange interaction with the conducting electrons, the same experiments have been performed on the corresponding enantiopure radical cation monolayer. Two manuscripts reporting results illustrated in this chapter are in preparation to be submitted in peer reviewed journals.

5.1 | Synthesis of thioacetyl of thia[4]hetero helicene

The neutral thioacetyl derivative of thia[4]hetero helicene has been synthesized according to the procedure reported in Figure 5.1. Hydroxy-substituted thiahelicene **1.5** was obtained as product of a Buchwald-Hartwig reaction[133] between 4-bromo-2-methoxy-1-methylbenzene (previously protected) and 3,7-dimethyl-phenotiazine. Thus **1.5** was reacted with 16-bromo-hexadecanoic acid in presence of diisopropylcar-

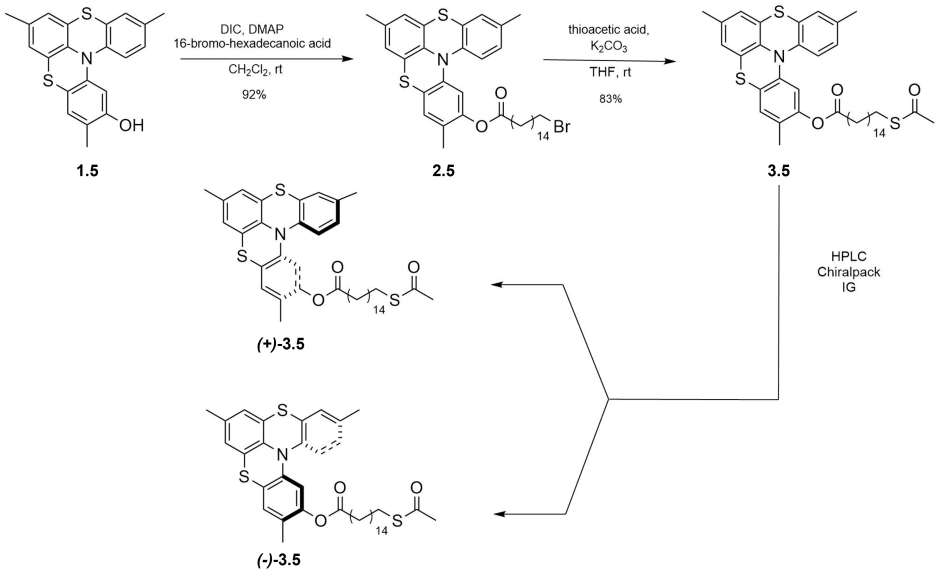

Figure 5.1: Scheme of the synthetic route to obtain enantiopure **(+)-3.5** and **(-)-3.5** compounds.

bodiimide (DIC) and *N,N*-dimethylamino pyridine (DMAP) in dry CH_2Cl_2 to give ester **2.5** isolated in 92% yield. Compound **2.5** was then reacted with thioacetic acid and K_2CO_3 in dry THF affording thioester **3.5** in 83% yield. Helicene **3.5** was resolved through semi-preparative HPLC on chiral stationary phase affording **(+)-3.5** (first eluted, $[\alpha_D^{25} + 180°]$, c=$5 \cdot 10^{-3}$, CH_2Cl_2) and **(-)-3.5** (second eluted, $[\alpha_D^{25} - 180°]$, c=$5 \cdot 10^{-3}$, CH_2Cl_2) both with e.e. $\geq$ 99%. The absolute configuration of the single enantiomer of derivative **3.5** has been assigned as (P)-(+) and (M)-(-) by comparison of previous results[118,129,134] on helicenes of type **3.5** (see Appendix A for experimental details).

5.2 | Thioacetyl helicene monolayer characterization

5.2.1 Assembly of thioacetyl helicene on Au(111)

Aiming to investigate the spin filtering properties, a monolayer of **3.5** has been assembled on a gold surface by exploiting the thioacetyl functionalization. The procedure adopted here is the same as the one used in the second step of the deposition of the system described in the previous chapter. A hydrogen-flame annealed Au foil on mica substrate was incubated in a diluted solution (2mM) of **3.5** in CH_2Cl_2 overnight at room temperature to induce the formation of a molecular layer. At the end of the deposition procedure several cleaning cycles with pure solvent were performed to ensure the removal of excess molecules left physisorbed on the surface.

5.2.2 STM characterization of thioacetyl helicene assembled on Au(111) surface

STM images were recorded to evaluate the morphology of the molecular monolayer assembled on the metallic substrate. The annealed bare gold surface reported in Figure 5.2a is characterized by atomic terraces and a periodic herringbone reconstruction pattern can be appreciated resulting from the spontaneous formation of "stress domains".[135] The molecular monolayer was assembled on the so treated surface and in Figure 5.2b a 150x150 nm^2 image is reported. In addition to the gold terraces, that are still visible and indicate a homogeneous growth of the molecular deposit, pinholes are present as expected when a self as-

sembled monolayer of thiols is formed on gold.[136] Measuring the profile at the edge of the pinholes, the height of the molecular monolayer was estimated as ca. 0.4 nm, which might be indicative of a lying arrangement of **3.5** on surface. Increasing the magnification of the scanned area (Figure 5.2c and d) it is possible to appreciate the presence of disordered dots whose lateral dimensions might be consistent with those of lying molecules (ca. 1.7 nm according to preliminary theoretical calculations). A statistical analysis was performed on the 45x45 nm^2 image and an average diameter of 1.8 nm was extracted as the peak of a lognormal distribution (Figure 5.2e).

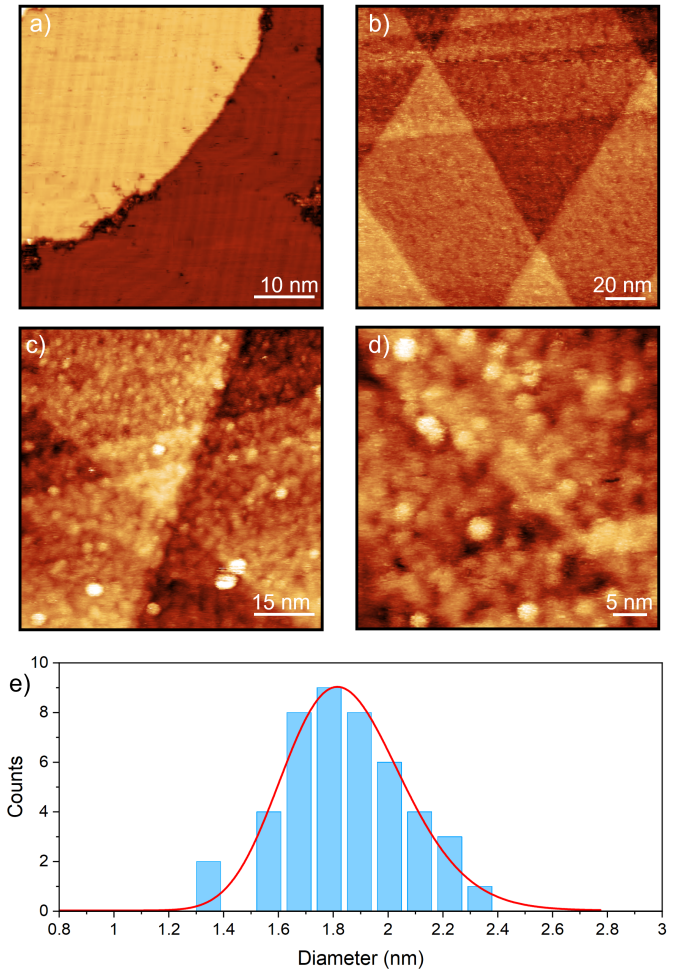

Figure 5.2: a) STM image of bare annealed Au/mica substrate recorded at room temperature (50x50 nm^2, V=2 V, I_t=200 pA). STM images of thioacetyl helicene monolayer assembled on Au(111) surface. b) 150x150 nm^2, V=0.1 V, I_t=300 pA; c) 75x75 nm^2, V=1.2 V, I_t=2 pA; d) 45x45 nm^2, V=1.2 V, I_t=2 pA. e) Statistical analysis extracted from image d).

5.2.3 XPS characterization of thioacetyl helicene assembled on Au(111) surface

The assembly of a monolayer of **3.5** from solution was verified by XPS. N1*s*, C1*s* and S2*p* regions were considered to perform a qualitative as well as a semi-quantitative analysis of the sample comparing the results with those obtained from a drop cast sample considered as the bulk reference of the starting **3.5** molecules. N1*s* XPS spectra of bulk **3.5** (Figure 5.3a top) features one component at 399.8 eV corresponding to the nitrogen atom present in the molecule.[137] This component is found in the N1*s* XPS spectra of **3.5**@Au as well (399.9 eV, Figure 5.3a bottom).[138,139] The analysis of C1*s* region of both bulk and **3.5**@Au samples (Figure 5.3b) suggests the presence of one main component at 284.3 eV attributed to C-C/C=C species and another one at 285.4 eV assigned to C-S/C-N. In addition, spectra feature two minor components at higher binding energy due to the presence of C-O/C=O functional groups that might come from environmental contamination.[140]

The most significant information about the assembly of **3.5** on the surface can be extracted by analyzing the S2*p* region (Figure 5.4). **3.5** bulk sample features a single major component, and its spin-orbit related one, at 163.4 eV; this is attributable to sulfur atoms in the helicene backbone and in the terminal thioacetyl group. In the S2*p* region of the monolayer a significant change in the line shape of the spectrum is noticed, due to processes occurring during the deposition procedure. Indeed, to reproduce the experimental data three components are needed. The component already detected in the bulk sample at 163.4 eV given by sulfur atoms in the helicene structure, plus a new

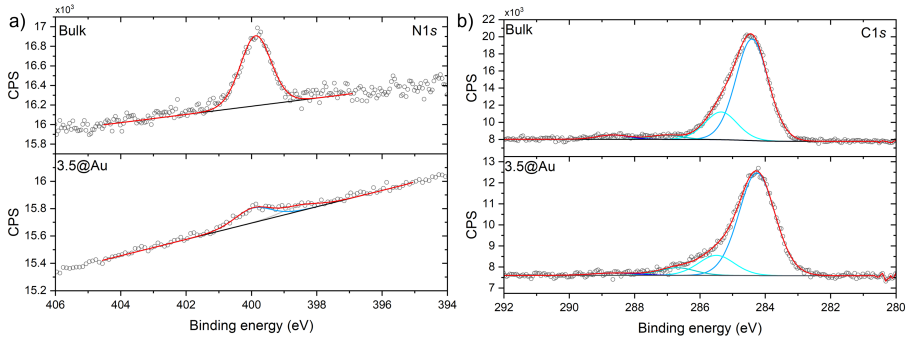

Figure 5.3: a) N1*s* XPS region of **3.5** bulk sample (top) and of **3.5**@Au (bottom). b) C1*s* XPS region of **3.5** bulk sample (top) and of **3.5**@Au (bottom).

component at 162.2 eV arising from the formation of covalent bonds between gold substrate and deprotected sulfur atoms of thioacetyl groups. The assembly of molecules on surface is further corroborated by the ratio between these two components, which is comparable with the theoretical one (2:1). Indeed, in case of chemisorption of the molecular monolayer, the two sulfur atoms belonging to the helicene backbone are expected to provide a higher binding energy signal with respect to the single sulfur atom bound to surface. We noticed an additional component present at lower binding energy (ca. 161.3 eV) due to a partial cleavage of carbon sulfur bond that leaves atomic sulfur adsorbed on the gold surface, as already known from literature.[141–143] Nevertheless, it is important to stress here that this partial degradation of molecules on surface can be considered as a part of defects of the molecular monolayer and it is assumed to be irrelevant for the CISS experiments that will be described in the next sections. Based on the previous fitting analysis, a semi-quantitative evaluation of the

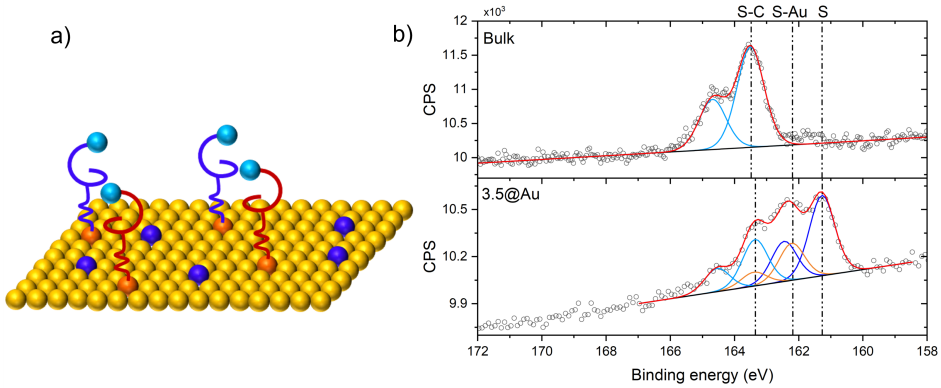

Figure 5.4: a) Scheme of monolayer of **3.5** assembled on Au. Spheres represents sulfur atoms in a different chemical environment: bound to Au surface (orange), in the helicene backbone (cyan) and atomic sulfur (blue). b) S2p regions of **3.5** bulk sample (top) and of **3.5**@Au monolayer (bottom). Color codes of the best fitting components are the same as in a). Each signal is accompanied by its spin-orbit coupled S2$p_{1/2}$ component shifted by 1.2 eV.

elemental composition of both bulk and monolayer samples has been obtained (Table 5.1). Considering the experimental error of the XPS technique the measured percentages are in good agreement with theoretical values.

Table 5.1: XPS semi-quantitative analysis of **3.5** bulk sample and of **(±)-3.5**@Au.

Sample	S2p[%]	N1s[%]	C1s[%]	S/N
Expected composition	7.1	2.4	90.5	3
Bulk	6.5±0.3	2.2±0.1	91.4±4.6	3
Expected SAM composition	75	25	–[b]	3
3.5@Au	74.5±3.7[a]	25.5±1.3	–[b]	2.9

[a] The contribution from atomic sulfur at 161.4 eV (blue component in Figure 5.4) has been excluded to properly evaluate the composition of the chemisorbed material on top of the gold substrate. [b] The contribution of carbon for semi-quantitative analysis of SAM has been excluded due to the presence of environmental carbon.

5.2.4 mc-AFM measurements on thioacetyl helicene monolayer

A first attempt to measure the spin filtering properties of the helicene monolayer was made by performing magnetic-conductive Atomic Force Microscopy (mc-AFM). This technique is a well-known method that has been proved to be excellent to measure the spin dependent conductivity through molecular layers assembled on surface[67] (several examples have been reported in Section 3.3.1). Molecules were assembled on a silicon wafer with on top a bilayer constituted by Ni/Au (100 nm and 8 nm thickness, respectively). Measurements were performed as a function of the magnetic field (±0.5 T) applied perpendicular to the surface. This allows to vary the magnetization direction of the ferromagnetic substrate either pointing up or down and, therefore, to align

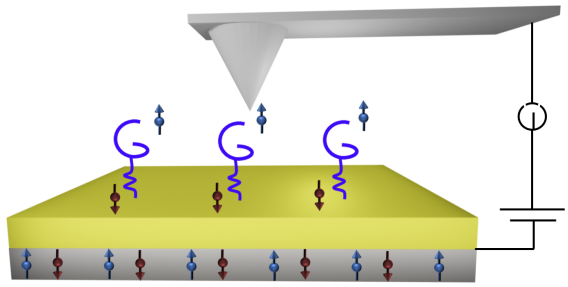

Figure 5.5: Experimental setup of mc-AFM. The injection of spin polarized electrons from the substrate into the enantiopure molecular layer is influenced by the handedness of molecules that promote a certain spin state and minimize the flow of electrons in the opposite spin state.

the spins of Ni substrate either parallel or antiparallel with respect to the direction of the flowing current. Besides, an electrical potential was applied so that the substrate is biased relative to the tip, which is at ground. The current flowing through the molecular monolayer was measured using a Pt-coated tip put in contact with the sample (further experimental details are reported in Appendix B). In Figure 5.5 a schematization of the experimental setup is reported.

Data shown in Figure 5.6a and Figure 5.6b represent the average *I-V* curves acquired on both enantiomers. At least 150 curves were scanned for each point and several points were investigated all over the surface for a proper statistical analysis. The trend of these curves clearly indicates that one spin state is favored when electrons flow from the substrate to the tip. Vice-versa, transmission of electrons in

the opposite spin state is promoted when current flows in the other direction. In addition, a correlation between the intensity of the spin current and the applied magnetic field is present. Indeed, with **(+)-3.5** a higher value of current occurs with a negative magnetic field, while the opposite behavior is observed with **(-)-3.5**, where a higher current is registered when applying a positive magnetic field. This behavior can be attributed to the chiral molecular monolayer acting as spin filtering agent. It is worth highlighting that the spin filtering process in this system occurs in a surprisingly narrow range of applied voltage. Indeed, contrary to previous studies reported in literature[67,73,81,144] involving DNA, porphyrins or helicenes, where the CISS effect was detected above ±1.5-2 V, here it is possible to appreciate a relevant difference in electron conduction within a ±0.3 V range. This allows a high spin polarization at very low potentials. The spin polarization percentage has been calculated for both enantiomers using the following equation $SP(\%) = \frac{I_{up}-I_{down}}{I_{up}+I_{down}} \times 100$, where I_{up} and I_{down} are the intensities of the current measured applying positive and negative magnetic field, respectively. As shown in Figure 5.6c, both systems exhibit a high spin polarization percentage of ca. 60%, with opposite sign for the two helicenes enantiomers. The degree of polarization is higher than reported in literature[50,145–147] for self-assembled monolayers of several chiral molecules, including helicenes. Furthermore, it is important to underline that the latter systems present chirality extended to the whole supramolecular structure, whereas in our case the chiral core is limited to the terminal part of molecules and the achiral alkyl chain does not play any role in the spin filtering process. This is even more relevant considering that several studies have shown that the percentage of spin polarization is proportional to the length of the

chiral structure.[73,148,149] A further interesting aspect is represented by the presence of a short circuit current in both samples. Indeed, curves feature the zero current value at 40 ±1.8 mV and 41 ±1.5 mV for **(+)-3.5** and **(-)-3.5**, respectively (Figure 5.6a and b, blue line). We may hypothesize that this behavior originates a reversible redox process these molecules may undergo.[15] We might speculate that a photoinduced process in the molecular monolayer could occur as a result of exposure of substrate to the laser light used in the mc-AFM experimental setup to detect the deflection of the tip. Another guess might ascribe the zero-shift to the surface potential arose as consequence of the deposition of the molecules. Further investigations are needed to fully explain the origin of this experimental observation.

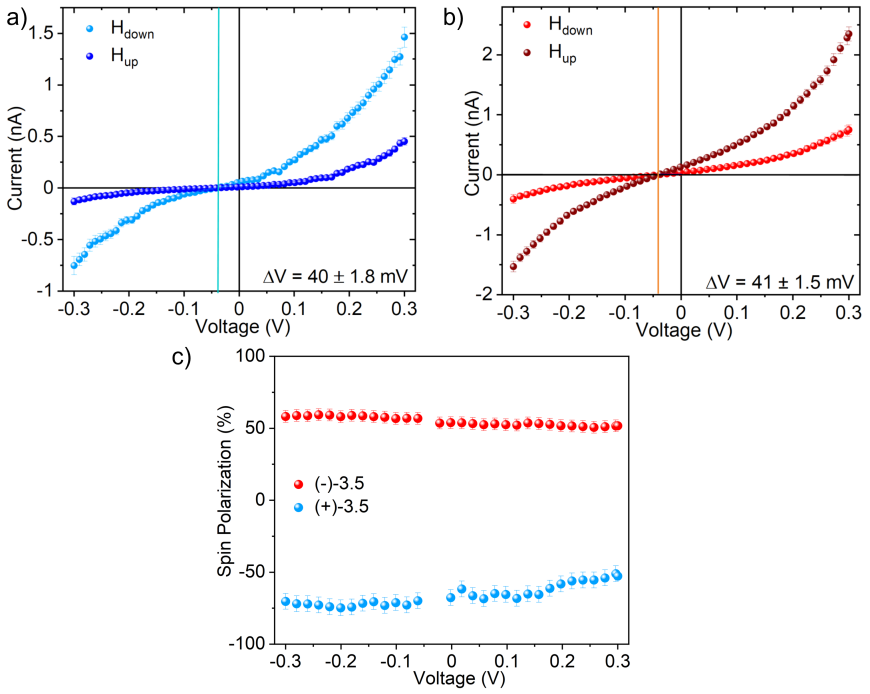

Figure 5.6: *I-V* curves acquired on a) **(+)-3.5**@Au and b) **(-)-3.5**@Au over a -0.3 V to 0.3 V bias window; blue and red plots correspond to measurements in −0.5T and +0.5 T applied fields, respectively. Vertical lines indicate the zero current point c) Spin polarization percentage extracted from a) and b) *I-V* curves.

5.2.5 Magnetoresistance measurements on thioacetyl helicene monolayer

Spin filtering properties of **3.5** were additionally investigated assembling a vertical multilayer molecular-based spintronic device to per-

form magnetoresistance (MR) measurements. A scheme of the device is shown in Figure 5.7a. Self-assembled monolayer of chiral molecules was deposited on a gold bottom electrode, then on top of the helicene layer a 2 nm insulating buffer layer of MgO was deposited, followed by Ni and Au (further details on the device fabrication are reported in Appendix B). The current flowing through the molecular layer was studied by varying the magnetic field, perpendicular to the substrate, between -1 T and +1 T using a standard four-probe measurement setup and applying a constant current of 0.5 mA. Figure 5.7b and Figure 5.7c report the MR percentage as function of applied magnetic field for **(+)-3.5** and **(-)-3.5**. The MR(%) was defined as follows: $MR(\%) = \frac{R_B - R_0}{R_0} \times 100$, where R_B is the resistance measured at magnetic field B and R_0 is the resistance measured at zero-magnetic field. Qualitatively, the results are consistent with those obtained with mc-AFM characterization. Indeed, an asymmetric trend of MR is clearly detected as a function of the magnetic field and an inversion of the signal occurs depending on the enantiomer involved. However, although a spin polarization induced by chiral molecules embedded in the device has been detected, in this case the percentage of spin polarization is much lower than found in mc-AFM measurements. This is because, at variance with what happens in mc-AFM, in MR measurements all the electrons flowing through the device are collected. These include both electrons passing through the molecular layer and electrons that are not filtered by the deposited molecules because they pass through pinholes. On the contrary, the experimental setup of mc-AFM allows to perform experiments by exploiting a local probe, which makes it possible to only collect electrons passing through the deposited molecules which act as spin filter. The resulting percentage of spin polarization is

therefore higher in mc-AFM than in MR. In Figure 5.7 the temperature dependence of MR is also reported. Analogously to what has already been observed on other chiral systems the percentage of MR increases approaching room temperature.[73,81,82] Although a theoretical model that reproduces and explains quantitatively these experimental results is still lacking, it has recently been hypothesized that phonon-enhanced spin-orbit coupling could play a crucial role.[87,150] Furthermore, it has been demonstrated that molecular vibrations give rise to molecular charge redistribution that could promote the spin polarization when chiral molecules are coupled to a non-magnetic metal.[151] Summarizing the work reported by Fransson *et al.*[87,150,151] it is possible to write the single electron Hamiltonian as Equation 5.1.

$$H = \frac{p^2}{2m_e} + V(\boldsymbol{r}) + \xi(\nabla V(\boldsymbol{r}) \times \boldsymbol{p}) \cdot \frac{\hbar}{2}\boldsymbol{\sigma} \tag{5.1}$$

where m_e is the mass of electron, $V(\boldsymbol{r})$ is the effective confinement potential and the last term defines the spin-orbit coupling contribution in terms of the orbital and the spin degrees of freedom $\boldsymbol{L} = \xi\nabla V \times \boldsymbol{p}$ and $\boldsymbol{S} = \hbar\boldsymbol{\sigma}/2$. The confinement potential $V(\boldsymbol{r})$ is defined in the vibrational coordinates $\boldsymbol{Q} = \boldsymbol{r} - \boldsymbol{r_0}$, where $\boldsymbol{r_0}$ is the equilibrium position. The orbital component of the spin-orbit coupling $\boldsymbol{L} = \xi\nabla V \times \boldsymbol{p}$ can thus be written as $\boldsymbol{L}(\boldsymbol{r}) = \boldsymbol{L_0} + \delta\boldsymbol{L}(\boldsymbol{Q}(\boldsymbol{r}), \boldsymbol{r})$, where

$$\begin{aligned} \boldsymbol{L_0} &= \xi \lim_{r\to r_0} \nabla V(\boldsymbol{r}) \times \boldsymbol{p} \\ \delta\boldsymbol{L}(\boldsymbol{Q}(\boldsymbol{r}), \boldsymbol{r}) &= \xi \lim_{r\to r_0} \nabla(\boldsymbol{Q} \cdot \nabla V(\boldsymbol{r}) + ...) \times \boldsymbol{p} \end{aligned} \tag{5.2}$$

From the contribution of the static spin-orbit coupling $\boldsymbol{L_0} \cdot \boldsymbol{S}$ there

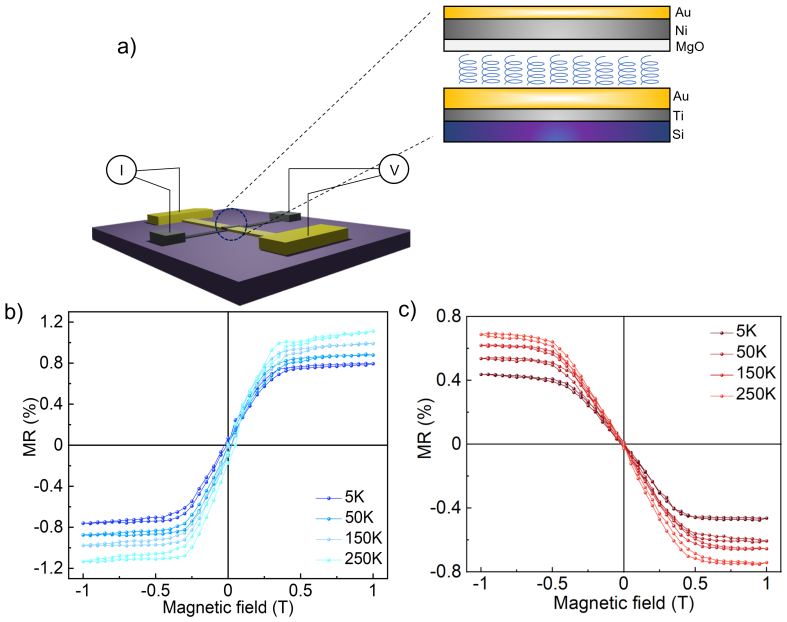

Figure 5.7: a) Scheme of four-probe MR device setup with details on cross junction structure. Temperature dependent magnetoresistance percentage as fuction of the applied magnetic field for b) **(+)-3.5** and c) **(-)-3.5**.

is no temperature dependence emerging. In contrast, the correction term $\boldsymbol{\delta L \cdot S}$ represents a vibrationally assisted process which provides a temperature dependence arising from the coupling between the electrons and the nuclear vibrations.

5.3 | Synthesis of thioacetyl thia[4]hetero helicene radical cation

Thia[4]hetero helicenes are suitable for one-electron oxidation, which afford the corresponding radical cations (**RadESAc**). In this work we performed a chemical oxidation of both enantiomers of **3.5**, using $AgSbF_6$ to obtain the organic chiral radicals to deposit on surface. The aim was to investigate CISS effect in comparison with the non-radical species to understand if unpaired electrons can influence the spin filtering process. After carrying out the enantiomeric resolution by semi-preparative HPLC on chiral stationary phase, one electron oxidation on both enantiomers of **3.5** was performed using a stoichiometric amount of $AgSbF_6$ in CH_2Cl_2 at room temperature. The corresponding radical cations (P)-**RadESAc** and (M)-**RadESAc** were isolated as dark purple solids, in 80% yield, after filtration of the formed Ag^0, evaporation of the solvent and recrystallization from CH_2Cl_2/hexane. In Figure 5.8 the synthesis of **RadESAc** is schematized (see Appendix A for experimental details).

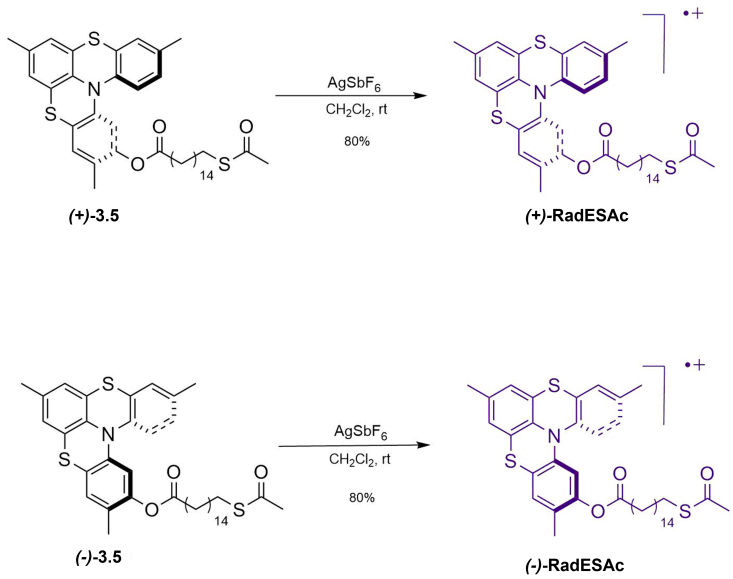

Figure 5.8: Scheme of the synthesis to obtain enantiopure RadESAc.

5.4 | EPR bulk characterization

The paramagnetic properties of **RadESAc** have been investigated by EPR spectroscopy both on a powder sample and in solution. In Figure 5.9a the EPR spectrum acquired on a powder sample of **RadESAc** is reported. It features a single absorption signal attributable to a S=1/2 paramagnetic system and, as expected, is comparable with the spectrum obtained on **RadE** (see Chapter 4), being the helicene structure identical. The hyperfine structure is not visible due to the intermolecular exchange interactions. On the other hand, spectra acquired on a solution of **RadESAc** (0.1 mM in CH_2Cl_2/toluene, Figure 5.9b) above and below the freezing point exhibit different line shapes. Indeed, at

200 K the solution is still fluid and the hyperfine substructure is clearly visible due to the interaction between unpaired electrons and nuclear spins, while in the frozen solution an anisotropic g factor is detectable. To best reproduce the experimental spectra the parameters reported in Table 5.2 were used for the simulations performed using the software *EasySpin*, as already explained for **RadE** in Chapter 4.[119] As expected, the g values and the magnitude of hyperfine interactions do not differ much from those obtained for **RadE**, being the helicene backbone identical.

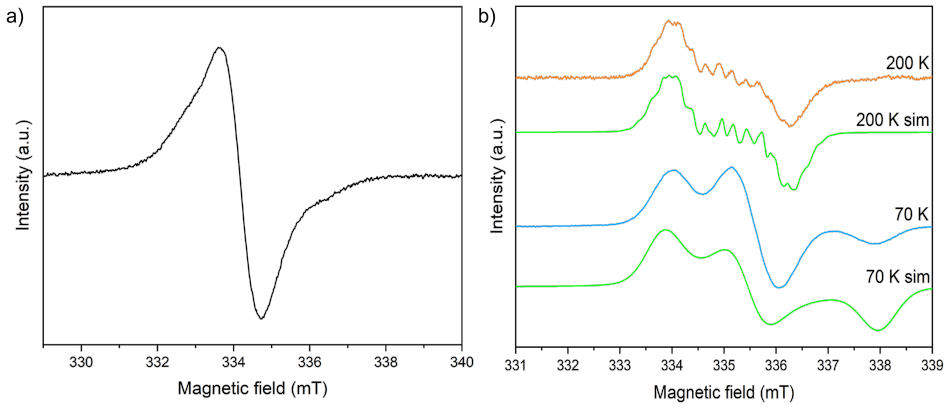

Figure 5.9: a) EPR spectrum of **RadESAc** powder at room temperature. b) EPR spectra of a solution of **RadESAc** in CH_2Cl_2/toluene 3:1 above and below the freezing point.

Table 5.2: g and hyperfine coupling values used for the simulations of EPR solution spectra of **RadESAc**. Fluid solution features an isotropic g and the spectral contribution of hyperfine coupling, while below the freezing point any hyperfine interaction is ruled out and an anisotropic g arises.

Fluid solution g=2.0071		
Nucleus	Equivalent nuclei	A (MHz)
N	1	22.08
H	6	6.84
H	3	5.77
H	2	3.11
Frozen solution		
g_x	g_y	g_z
2.0171	2.0073	1.9923

5.5 | Thioacetyl helicene radical cation monolayer characterization

5.5.1 Assembly of thioacetyl helicene on Au(111)

The procedure adopted to deposit a monolayer of **RadESAc** on surface (**RadESAc**@Au) provided the formation of covalent bonds between the deprotected terminal sulfur atoms and the gold surface. Thus, after an hydrogen flame annealing treatment, the Au on mica substrate was incubated overnight in a diluted solution of **RadESAc** (1mM in CH_2Cl_2) at room temperature to induce the formation of a well ordered molecular layer. At the end of the deposition procedure several cleaning cycles with pure solvent were performed to ensure the removal of the molecules physisorbed on the surface.

5.5.2 XPS characterization of thioacetyl helicene radical cation assembled on Au(111)

The correct assembly of **RadESAc** on the surface has been verified performing an XPS characterization both on dropcasted sample (used as reference) and monolayer samples. N1s, C1s, F1s and S2p regions have been investigated to obtain qualitative and quantitative information on samples. For the bulk sample, as already observed for **RadE**, N1s region does not allow the extraction of qualitative information due to the radiation damage that occurs when organic radicals are exposed to X-rays. Indeed, three components at 399.6 eV, 401.1 eV and 402.2 eV are needed to fit the experimental data (see Figure 5.10a). The signal at lower binding energy is attributable to nitrogen atom of neu-

tral species as observed for **3.5**, whereas the other major component is due to oxidized nitrogen atom of radical cation species. The signal occurring at higher binding energy corresponds to *shake-up* transition of the aromatic system.[137–139] Radiation damage due to the exposure to X-rays is even more relevant in the monolayer sample, where the major component is the one at 399.6 eV, assigned to the neutral form. The other two components at higher binding energy, coming from radical cation species and *shake-up* transition, are still present, although very weak in intensity. The C1*s* region of the bulk sample features four components, as reported in Figure 5.10b: one main component at 283.9 eV, another component at 285.1 eV and two minor components at higher binding energy. The main signal can be attributed to C-C/C=C species of the helicene,[140] whereas the second one is assigned to C-N/C-S groups.[152] The minor components are due to the presence of C-O/C=O functional groups that might come from environmental contamination,[153] since samples have been exposed to the air and manipulated during the preparation. C1*s* spectrum acquired on the monolayer is also characterized by four components, which are comparable with those observed for the bulk phase. Indeed, there is a major component at 284.1 eV, plus three additional signals at 285.1 eV, 286.2 eV and 288.3 eV attributable to the same species described above. The F1*s* XPS spectrum of the bulk sample shows, as expected, one single component at 685 eV attributable to fluorine atoms of SbF_6^- anion (Figure 5.10c).[154] The same signal is observed in the F1*s* region of the spectrum acquired on the monolayer sample, which thus confirms the presence of the counterion after the deposition process. Nevertheless, as demonstrated by the semi-quantitative analysis discussed below, the amount of fluorine is lower than expected based on the

bulk composition. This experimental evidence agrees with a previous literature report,[155] where it was observed that charged molecules deposited on surface can lose partially or totally their counterions due to the stabilization given by the electron density of the metallic surface. In addition, the lower percentage of fluorine with respect to the expected value could be ascribed to the formation of neutral species due to the radiation damage, thus leading to the partial loss of counterions on surface. S2p XPS region is fundamental to confirm the formation of covalent bonds between sulfur atoms and the gold surface. In the bulk sample, just one component at 163.2 eV (and its relative spin-orbit coupled one), assigned to sulfur atoms of the helicene structure, is needed to properly fit the data (Figure 5.10d, top). On the contrary, in the monolayer sample an additional component at lower binding energy (161.8 eV) is found, demonstrating S-Au bond formation (see Figure 5.10d, bottom). Furthermore, the ratio between these two components, equal to 2:1, is consistent with the expected theoretical value. These data are in contrast with those obtained on the neutral helicene, where another component in the S2p region was found at 161.4 eV, ascribable to elemental sulfur. We might hypothesize that the positive charge of the radical cations influences the molecular surface organization with repulsive intermolecular interactions, stabilizing the system and avoiding any cleavage of C-S bonds.

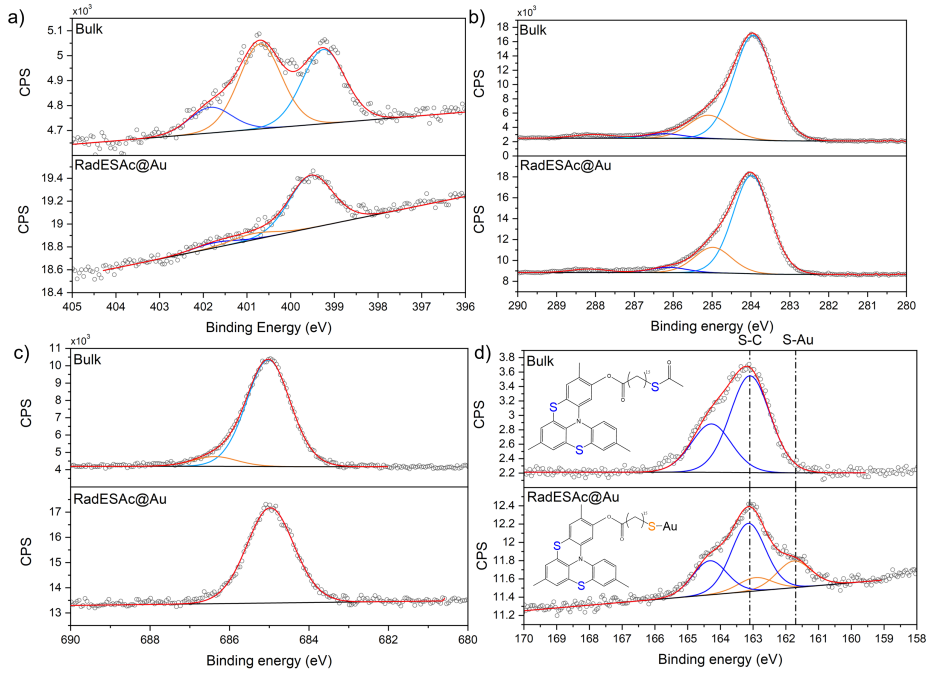

Figure 5.10: a) N1*s*, b) C1*s*, c) F1*s* and d) S2*p* XPS regions acquired on **RadESAc** bulk sample and on **RadESAc**@Au monolayer. Inset: molecular structure of **RadESAc** before and after the deposition process (color code is in according to the components).

The four XPS regions were exploited also to extract a semi-quantitative analysis and used as a tool to estimate the elemental composition of molecules once assembled on the substrate. Considering the experimental error of the XPS technique, the values reported in Table 5.3 corroborate the correct assembly of **RadESAc** on gold. This is at variance with the results of XPS analysis on **3.5**, where a partial degradation of molecules was detected given the presence of elemental sulfur on the gold surface (see Section 5.2.3).

Table 5.3: XPS semi-quantitative analysis of **RadESAc** bulk sample and of **RadESAc**@Au.

Sample	S2p[%]	N1s[%]	C1s[%]	F1s[%]	S/N	F/N
Expected bulk composition	6.3	2.1	79.2	12.5	3	6
Bulk	6.4±0.3	1.8±0.1	84.5±4.2	7.3±0.4	3.7	4.1
Expected SAM composition	6.5	2.2	78.3	13	3	6
RadESAc@Au	6.8±0.3	2.2±0.1	83.9±4.2	7.1±0.3	3.2	3.3

5.5.3 EPR characterization of thioacetyl helicene radical cation assembled on Au(111)

Once the composition on surface was confirmed, EPR technique was exploited to investigate the paramagnetic properties of **RadESAc**@Au monolayer. This investigation aimed at understanding whether the radical nature is retained even after the deposition process and the formation of covalent bonds between molecules and the surface. As shown in Figure 5.11 the EPR spectrum acquired on **RadESAc**@Au sample is clearly comparable with that obtained on powder. Thus, it confirms the persistence of paramagnetism at the monolayer level. In addition, since the sub-structure is also absent, the intermolecular exchange interactions must be of comparable magnitude to those occurring in a powder sample.

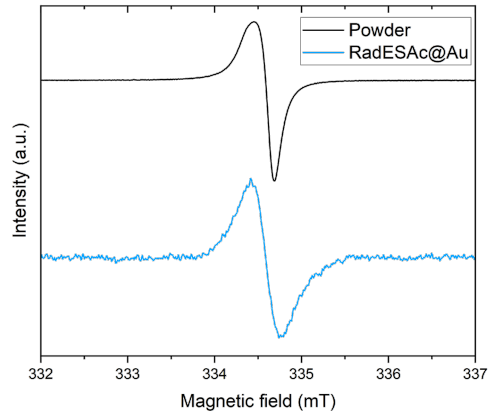

Figure 5.11: EPR spectra on **RadESAc** powder and on **RadESAc**@Au monolayer at 30 K.

5.5.4 mc-AFM measurements on thioacetyl helicene radical cation monolayer

Once the presence of intact radical cations on surface was demonstrated a characterization similar to that of the neutral form was performed aiming to investigate the effect of paramagnetic species on CISS. Indeed, as demonstrated by Torres-Cavanillas and coworkers[156] studying chiral metallopeptides embedding paramagnetic Tb^{3+} or diamagnetic Y^{3+} ions the presence of unpaired electrons enhances the spin polarization of the current. Hence, a monolayer of **RadESAc** was assembled on a Ni/Au substrate for mc-AFM measurements. In Figure 5.12 *I-V* curves acquired on both enantiopure monolayers are reported. The intensity of the current varies as a function of the direction of the magnetic field. Furthermore, an opposite behavior is observed for opposite handedness of the molecules. This experimental observation confirms that CISS effect occurs also for monolayers of radical cations. The

only difference with respect to the neutral form lies in the shape of the curves: in **RadESAc** a more linear trend than in neutral compound is observed; further, the conductivity of samples is higher, as expected for an organic radical.[157] As already observed in the neutral species (see Section 5.2.4) a short circuit current is detected. Furthermore, the magnitude of the shift is almost the same as in the neutral form, being 41 ±1.3 mV and 42 ±1.6 mV for (P)-**RadESAc**@Au and (M)-**RadESAc**@Au, respectively (to be compared with 40±1.8 and 41±1.5 in the neutral form). We might again hypothesize that molecules assembled on surface undergo a charge separation process; however, this aspect must be further clarified. The spin polarization percentage extracted for both enantiomers does not show any relevant difference with respect to the neutral form, being about 60%. Nevertheless, this kind of characterization cannot exclude that the unpaired electrons influence the spin filtering process. Indeed, at room temperature the Zeeman splitting in a 0.5 T field is very small with respect to k_BT (ca. 1:400) and exchange interaction between the unpaired electron of the radical and the flowing current might not be strong enough to enhance the spin polarization.

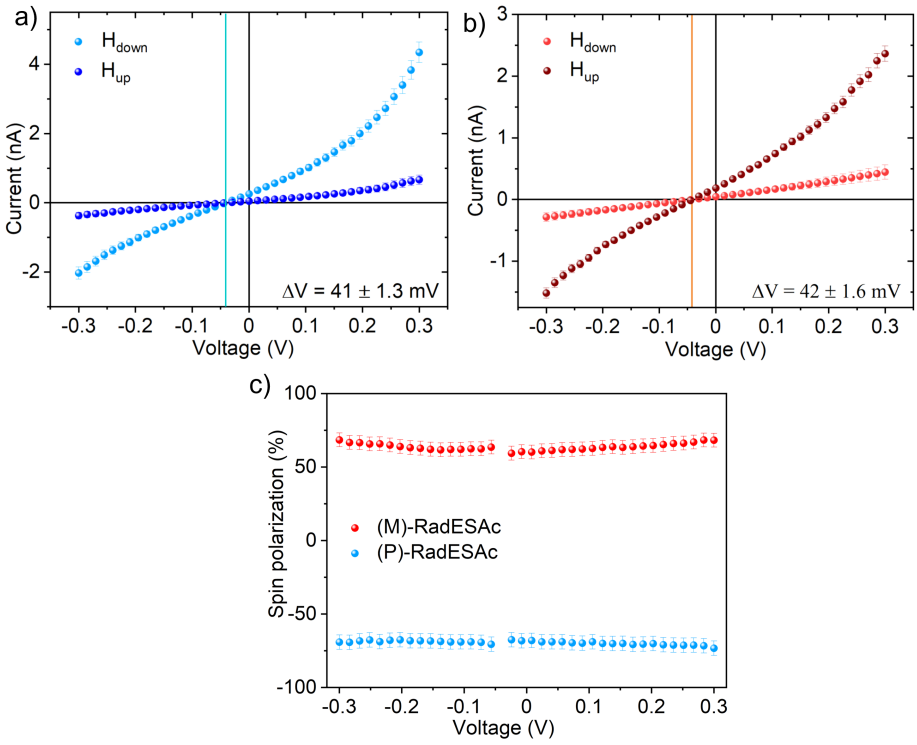

Figure 5.12: *I-V* curves acquired on a) (P)-**RadESAc**@Au and on b) (M)-**RadESAc**@Au over a -0.3 V to 0.3 V bias window; blue and red plot correspond to measurements in −0.5 T and +0.5 T applied fields. Vertical lines indicate the zero current point. c) Spin polarization percentage extracted from a) and b) *I-V* curves.

5.5.5 Magnetoresistance measurements on thioacetyl helicene radical cation monolayer

Analogously to what has been done with the neutral helicene, also **RadESAc** was used as active chiral layer in a molecular-based spintronic device to perform magnetoresistance measurements. The device was assembled following the same procedure adopted for the neutral compound (see Section 5.2.5 and Appendix B) and magnetoresistance curves were acquired according to the same experimental procedure, thus with a standard four probe setup applying a constant current of 0.5 mA. Qualitatively the results are coherent with mc-AFM characterization as well as with the results obtained with the neutral compound. Indeed, spin filtering behavior is detected also using the radical form, given the asymmetric trend of MR and the occurrence of an inversion of the signal according to the handedness of the embedded helicene (Figure 5.13a and b). It is possible to appreciate also the temperature dependence of the signal. As found with the neutral species, the MR percentage is enhanced with temperature due to phenomenon briefly summarized in Section 5.2.5.

Although **RadESAc** clearly exhibits the occurrence of CISS effect, it is not so clear if the unpaired electrons of the organic radicals are playing a role in the spin selectivity process. A slightly enhancement of the spin polarization percentage can be appreciated at low temperature (50 K and 5 K), by analogy with what was observed by Poggini *et al.*[64] studying a monolayer of nitronyl nitroxide radicals embedded in an organic spin valve. In their work, they find that the magnetoresistance of the device below 25 K is influenced by the ferromagnetic interaction between the LSMO substrate and the unpaired electrons of

the radicals in the monolayer. However, in this preliminary phase of the work on **RadESAc**, it is difficult to unambiguously ascribe the enhancement of spin polarization to the presence of paramagnetic species on the surface. Furthermore, even if the spin polarization percentage extracted is mildly higher, it could be due to the higher homogeneity of the molecular assembly, as confirmed by the XPS characterization (see Section 5.5.2). Therefore, though some differences are present, further investigations are needed to better understand and quantify the influence of paramagnetism on the spin polarization of the flowing current.

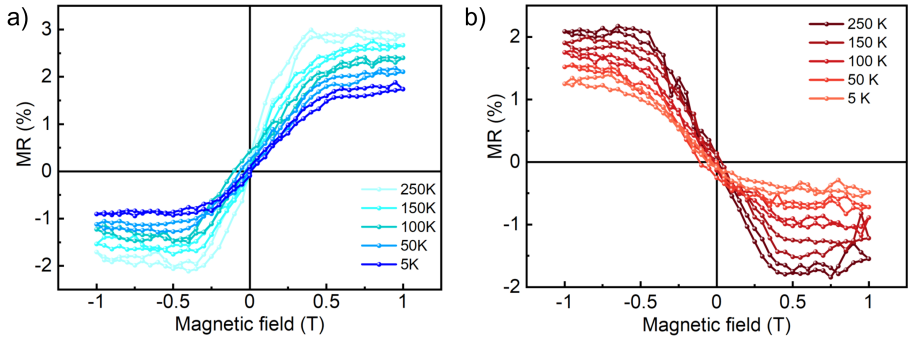

Figure 5.13: Temperature dependent magnetoresistance percentage as function of the applied magnetic field for a) (P)-**RadESAc** and b) (M)-**RadESAc**.

In summary, in this Chapter5 thia[4]helicene chemically anchored on surface showed a high efficiency as a spin filtering agent and was hence identified as possible candidate for the development of new chiral spintronic devices. Besides, the possibility to obtain the corresponding radical cation by chemical oxidation opens an additional fascinating

perspective to merge chiral structure and paramagnetic properties in a unique compound introducing new parameters capable of influencing the spin polarization of electrons. Nowadays our efforts are focused in this direction.

6 | CISS in QD-χ-C_{60} system

Almost all the experimental studies on CISS effect involve chiral molecules deposited on a metallic/ferromagnetic substrate. As discussed in Chapter 3, the substrate operates as the reservoir for electrons in different experiments including mc-AFM, molecular-based devices, electrochemistry measurements and photoemission spectroscopy among others. On the other hand, a study on a system that exhibits CISS effect without comprising chiral molecules supported on substrate was still lacking. Furthermore, only a few attempts to implement CISS using light have been performed.[158–160] In this type of experiments, a charge transfer has been induced and probed indirectly by studying competitive non-radiative and radiative relaxation processes as function of the applied magnetic field, light polarization or molecular handedness.[158] In the last part of my PhD thesis I have had the chance to collaborate with a group of researchers including members of the Universities of Florence, Torino, Bologna and Parma working in this scenario. Here, slightly deviating from what has been described in the previous chapters, I will briefly summarize our results focused on the evaluation of a molecular

photoinduced CISS in a donor-chiral bridge-acceptor (D-χ-A) system. For that purpose, a CdSe quantum dot (QD) was exploited as electron donor, thus an electron localized reservoir, and an organic molecule, *i.e.* fullerene C_{60}, was used as an electron acceptor. Finally, a short polypeptide was selected as chiral bridge between the two units. The *dyad* so drawn has been engineered to optimize the charge transfer process. Indeed, the energy level alignment of CdSe QD and of fullerene has been properly adjusted to promote the electron transfer toward the fullerene after excitation of the donor with light. Furthermore, the structure of the chiral bridge has been designed to obtain a good compromise between the stability of the system and its rigidity to prevent the folding of C_{60} on the surface of the QD. The system (QD-χ-C_{60}) was synthesized via a ligand exchange approach by Prof. Tomasini and coworkers at the University of Bologna, and characterized in bulk phase via optical spectroscopies. Then, I performed the XPS experiments aimed to confirm the correct assembly of the *dyad*. Thus, at the University of Turin, by exploiting time-resolved EPR (tr-EPR), a spin polarized state generated by a photoinduced charge transfer (CT) from QD to C_{60} has been detected, a phenomenon compatible with the presence of CISS effect.

The confirmation of chemisorption of molecules on the surface of QD was not trivial due to several issues: i) ^{31}P-NMR could not be used to verify the presence of P-based capping molecules on top of QDs surface due to the fast relaxation process induced by the presence of CdSe nanoparticles;[161] ii) AFM resolution was not high enough to appreciate changes in the thickness of QD after the exchange reaction between capping molecules and χ-C_{60}. On the contrary, XPS experiment clearly demonstrated the correct assembly of QD-χ-C_{60}, corroborating all the

results obtained with the tr-EPR measurements. Results reported in this chapter have been published in a peer-reviewed journal.[162]

6.1 | QD-χ-C_{60} system synthesis

The QD-χ-C_{60} system used in this work is reported in Figure 6.1a. CdSe QDs were prepared following the hot injection method reported in literature,[163] obtaining nanoparticles with an average diameter of ca. 5 nm. The fullerene-functionalized polypeptide was obtained through liquid phase synthesis. First of all, the polypeptide was obtained following the reaction path reported in literature,[164] and then coupled with fullerene C_{60} functionalized via Prato reaction[165] to afford *N*-2-aminoethyl-fulleropyrrolidine. Finally the S-protecting trityl group was removed[166] and **1** was isolated as a pure compound. The ligand exchange reaction exploited the strong affinity of thiols for the CdSe surface and it was performed by stirring trioctylphosphine oxide (TOPO) capped CdSe QDs and **1** in a solution of $CHCl_3$. Once QD-χ-C_{60} species is formed, a relevant change in solubility occurs due to a drastic reduction of colloidal stability, thus inducing the precipitation of the species.

Components of this system were chosen for their energy level diagram compatible with the charge transfer that is expected to occur (Figure 6.1b). Indeed, CdSe QDs have tunable light absorption wavelength according to their dimension. Literature reports[167] indicate that the conduction and valence band energies of CdSe QDs with a diameter of 5 nm are respectively -3.1 and -5.4 eV. On the other hand, C_{60} has frontier energy levels at -4.0 and -6.2 eV. With this energy level arrangement, after photoexcitation of the QD, an electron is expected

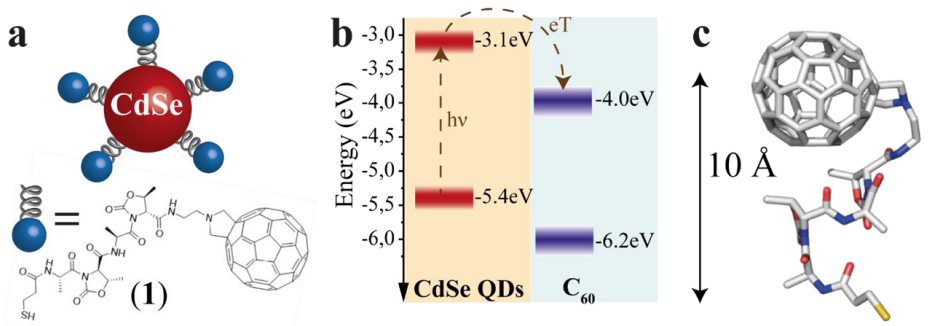

Figure 6.1: a) Schematized structure of QD-χ-C_{60} system. b) Energy level diagram of CdSe QD and C_{60}. Arrows represent the charge transfer process after light absorption. c) DFT-optimized structure of the ligand **1**. Reproduced from ref.[162]

to move towards the fullerene moiety. Also the chiral linker was carefully chosen looking for a good compromise between CT efficiency and effective chiral potential for the CT process. A DFT geometry optimization was performed to estimate the structural conformation of **1** once assembled on the CdSe surface (Figure 6.1c). This model suggested that the geometry of the pristine chiral bridge is preserved when attached to fulleropyrrolidine because its structure is rigid thanks to the presence of intramolecular hydrogen bonds.

6.2 | Chemical characterization of QD-χ-C_{60}

Optical measurements Optical measurements were carried out to investigate the ligand-exchange reaction. In Figure 6.2a the UV-Vis absorption spectra and the photoluminescence (PL) spectra are reported for QD-χ-C_{60} and bare CdSe QDs. The UV-Vis spectra of QD-χ-C_{60} can be interpreted as the sum of two contributions: CdSe QDs around

600 nm, in analogy with the pristine nanoparticles, and C_{60} broad signal up to 700 nm, typical of fullerene derivatives.[168] In addition, the PL spectra of both species reported in the inset of Figure 6.2a show a quenching of the emission of QD-χ-C_{60} system compared with the pristine QDs. This can be ascribed to the trapping of the photogenerated hole on the thiol molecules. Indeed, the energy of the valence band of CdSe QDs is lower with respect to the standard potential level of the thiol; thus, an hole trapping occurs avoiding the recombination of the exciton pair and decreasing the luminescence.[169] The correct assembly of the system was investigated also by performing time-resolved photoluminescence (tr-PL) decay measurements. The luminescence decay follows a tri-exponential decay kinetics. This can be rationalized by analyzing the different relaxation paths that an hole-electron pair exciton can follow. The most direct one is the recombination of the electron-hole pair and the radiative relaxation to the ground state. In addition, hole-electron located in shallow trap states can follow two further different paths: they can repopulate the conduction band or thermalize into deeper trap states. The former path contributes to the longer PL lifetimes, whereas the latter path contributes to nonradiative mechanisms. The union of these three mechanisms can be modeled with the Equation 6.1.

$$PL(t) = a_1 exp(-\frac{t}{\tau_1}) + a_2 exp(-\frac{t}{\tau_2}) + a_3 exp(-\frac{t}{\tau_3}) \qquad (6.1)$$

Thus, Equation 6.2 was used to compare the PL lifetimes $\langle\tau\rangle$ of the QDs before and after the ligand-exchange reaction .

$$\langle\tau\rangle = \sum_i a_i \tau_i^2 / \sum_i a_i \tau_i \qquad (6.2)$$

Values obtained are $\langle\tau\rangle = 29.0 \pm 0.5$ ns and $\langle\tau\rangle = 2.6 \pm 0.5$ ns for CdSe QDs and QD-χ-C_{60}, respectively. The faster nonradiative decay is induced by the presence of the thiols on the surface, hence confirming the success of the exchange reaction.

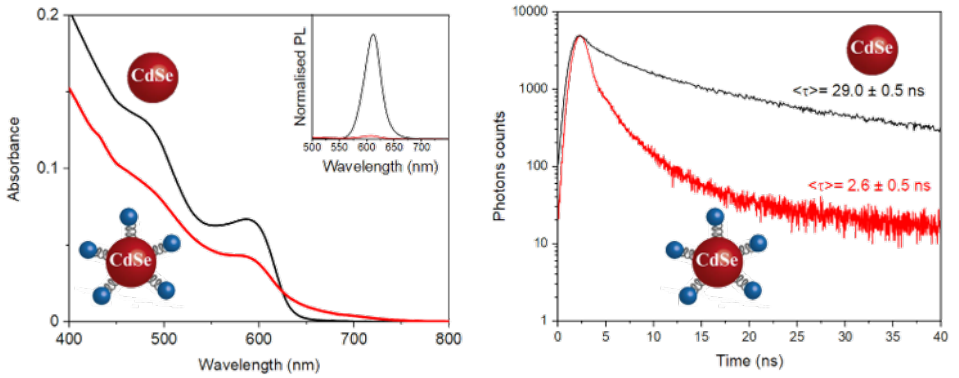

Figure 6.2: a) UV-Vis absorption spectra of bare CdSe QDs (black) and QD-χ-C_{60} (red) in 1,2,4-trichlorobenzene solution. Inset: PL spectra excited at $\lambda_{ex} = 400$ nm. b) Photoluminescence decay curves recorded at $\lambda = 610$ nm with $\lambda_{ex} = 370$ nm. Reproduced from ref.[162]

XPS measurements To further corroborate the success of the assembly of QD-χ-C_{60} system an XPS characterization was carried out. In this case the advantage with respect to optical measurements is the element sensitivity that allows to understand the chemical environment as well as the oxidation state of the investigated atoms; most relevant are C1s and S2p/Se3p regions. In Figure 6.3a the C1s regions of QD-χ-C_{60} system and of bulk phases of the individual building blocks are reported. While in the C_{60} spectrum only an intense signal at 285 eV arising from C=C species is observed,[170] in the χ bulk sample four components are needed to properly fit the experimental data. The

four components correspond to C-C (284.6 eV), C-N/C-O (286.5 eV), COOR (288.4 eV) and *shake-up* transition (290.3 eV).[152] The same components can be detected also in the χ-C_{60} sample, except for the one at lower binding energy, which is obscured by the intense component at 285.1 eV attributable to the C sp^2 atoms of the fullerene moiety. In the spectrum of pristine CdSe QDs the main component at 284.3 eV is attributed to aliphatic carbon atoms of the TOPO ligand, while the minor component at 285.8 eV is assigned to adventitious carbon.[171] Finally C1*s* region acquired on QD-χ-C_{60} sample features all the components observed in the previous systems confirming the coexistence of both χ-C_{60} and TOPO molecules after the exchange reaction. However, a decrease of the latter component occurs. This observation demonstrates that TOPO molecules are a minority part of the system and most of them have been lost during the exchange reaction. Further confirmation of the presence of both ligands on the surface of QDs is given by the P2*p* XPS signal (132.4 eV) detectable on samples before and after the reaction (Figure 6.3b).

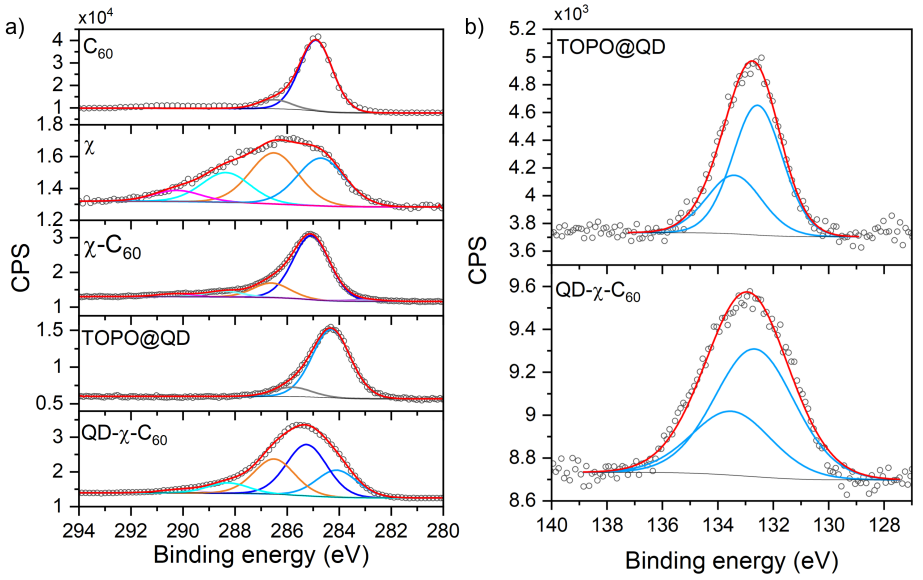

Figure 6.3: C1s and P2p XPS regions acquired on C_{60}, χ, χ-C_{60}, TOPO@QD samples and on QD-χ-C_{60} system.

Crucial insight regarding the assembly of molecules on the surface of QDs can be deduced by the analysis of S2p/Se3p region (Figure 6.4). In the spectra of bulk χ and χ-C_{60} samples, a component attributable to thiol groups at 163.5 eV is present,[172] accompanied by its relative spin orbit signal at higher binding energy (+1.18 eV). In addition, a negligible component at ca. 167 eV is present due to a partial oxidation of sulfur atoms.[173] In pristine CdSe QDs, a sulfur signal is obviously not observed, while a Se3$p_{3/2}$ signal (159.7 eV) and its relative spin orbit component (+5.7 eV) are clearly visible.[174] In QD-χ-C_{60} sample, due to the overlap of Se3p and S2p contributions, we observed a change in the line shape originating from the simultaneous presence of selenium and of an additional component at 161.8 eV attributable to

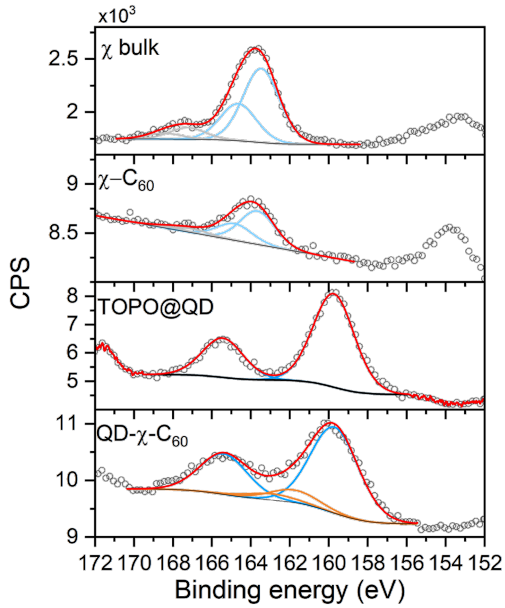

Figure 6.4: S2p/Se3p XPS regions acquired on χ, χ-C_{60}, TOPO@QD samples and on QD-χ-C_{60} system.

sulfur atoms bound to the surface of QDs.[175] Furthermore, the spectrum does not feature signals at 163.5 eV and at ca. 167 eV, which are characteristic of S-H and S-O_n groups, thus excluding the presence of physisorbed or oxidized species.[173]

6.3 | Spin polarized photoinduced charge transfer

Once confirmed the correct assembly of the QD-χ-C_{60} system the photoinduced CT was investigated by performing tr-EPR characterization. The experiment was performed by Chiesa and coworkers at the University of Turin. This technique gives access to information about spin polarized states showing signals in enhanced absorption and emission.

For clarity, up to now in this text the expression "spin polarization" has been used to describe a current which has an unbalance of spin states of the electrons. At variance, in tr-EPR community, this expression is referred to a system which is out of the Boltzmann equilibrium due to an external stimulus such as light irradiation. Hereafter, in this paragraph, this expression will be used with the latter meaning. tr-EPR investigation was performed at 40 K on a solution of QD-χ-C_{60} and on a solution of QD-χ + C_{60} (7.8 μM in 1,2,4-trichlorobenzene) using an excitation wavelength of 450 nm. In Figure 6.5a the tr-EPR spectra acquired at 1 μs after the excitation are reported. In both samples a broad signal between 335 and 358 mT is visible. This signal is due to the C_{60} triplet state which forms *via* intersystem crossing (ISC) from a photogenerated singlet excited state in C_{60} that does not undergo electron transfer.[176] However, we can appreciate here a first difference between the two samples. The QD-χ-C_{60} spectrum shows more pronounced shoulders than in the spectrum of the separated systems. This might be due to the different environment of fullerene molecules, which might more easily undergo ISC when linked to the CdSe QDs. The most significant difference arises at ca. 346 mT, where an intense absorption signal is present in the spectrum of QD-χ-C_{60}, while it is not present in the spectrum of the separated systems. This signal can be attributed to a C_{60} radical anion formed by electron transfer from CdSe QD to C_{60} upon light irradiation. On the other hand, in agreement with a previous literature report,[177] it was not possible to appreciate the signal of the hole left on the QD, due to the fast spin relaxation process induced by the large spin-orbit coupling of Cd atoms. It is also worth highlighting the time evolution of spin polarization in the first μs after the irradiation (Figure 6.5b). Indeed, the C_{60} signal

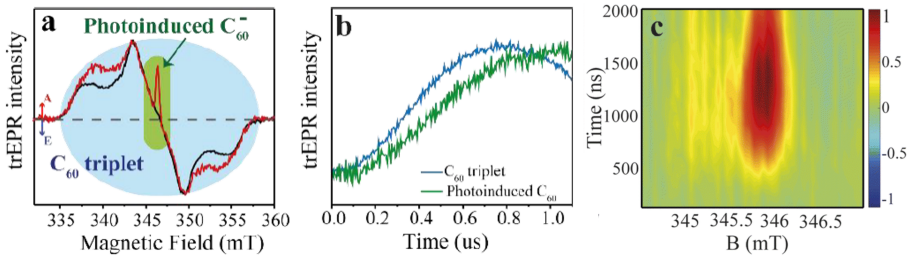

Figure 6.5: a) Tr-EPR spectra acquired at 40 K on QD-χ-C_{60} (red) and on QD-χ + C_{60} (black) at 1 μs after the 450 nm laser pulse. Only red spectrum features a sharp signal occurring at ca. 346 mT and attributable to the radical anion species. b) Normalized tr-EPR transient centered at 343 and 346 mT for triplet state and radical anion, respectively. c) 2D experimental trEPR contour plot of the charge transfer signal acquired after 450 nm laser pulse. Reproduced from ref.[162]

rises slowly with respect to the C_{60} ISC triplet signal, reaching its maximum after at 1 μs. This contrasts with what is theoretically expected, being the ET one order of magnitude faster with respect to the ISC relaxation.

To better understand the ET process occurring in the QD-χ-C_{60} system, tr-EPR spectra were simulated focusing on the magnetic field region relevant for the charge transfer signal (radical anion peak) and excluding the triplet state that is independent from CISS effect phenomenon. Simulation has been performed describing the initial state as a density matrix $\rho(0)$ containing the four singlet and triplet initial states, and using a spin Hamiltonian (Equation 6.3) to account for the dipolar and Zeeman interactions, while neglecting the isotropic exchange coupling.

$$H = \mu_B \boldsymbol{B_0} \cdot (g_D \boldsymbol{S_D} + g_A \boldsymbol{S_A}) + \boldsymbol{S_D} \cdot \boldsymbol{D}(\Omega) \cdot \boldsymbol{S_A} - \hbar\omega_0 (g_D S_z^D + g_A S_z^A) + \mu_B B_1 (g_D S_x^D + g_A S_x^A) \tag{6.3}$$

Here g_D and g_A are the isotropic g-factors of the donor and the acceptor species, $\boldsymbol{B_0}$ is the static magnetic field, $\boldsymbol{D}$ is the spin-spin interaction tensor, $\omega_0/2\pi = 9.69$ GHz is the microwave frequency and $B_1 = 0.02$ T is the microwave field strength. Using the $\rho(\Omega, t)$ obtained for each time and magnetic field value, the tr-EPR spectra have been extracted by using the Equation 6.4.

$$EPR(t) = \int Tr\{(g_D \hat{S}_y^D + g_A \hat{S}_y^A)\hat{\rho}(\Omega, t)\} d\Omega \tag{6.4}$$

Since ISC relaxation within the donor QD occurs very fast (few picoseconds), the electron could move toward the acceptor either from the excited singlet state or from the triplet state of the QD. For this reason, three different situations were considered with three different initial states: a pure singlet state (S), a pure triplet state (T) and a mixture of singlet and triplet states (ST) with all four levels equally populated (Figure 6.6).

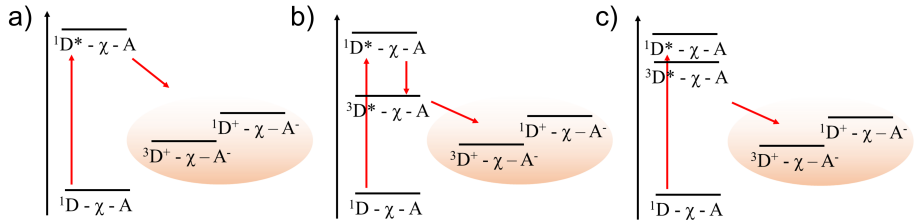

Figure 6.6: Energy level diagrams of a) pure singlet, b) pure triplet and c) mixed singlet and triplet initial states after the laser irradiation.

Furthermore, calculations were performed also considering the presence of CISS effect, modeling it as a "filter" which ideally keeps the spin component parallel to the chiral bridge axis. This issue influences the final tr-EPR spectra. For a better comparison, in Figure 6.5c, the 2D experimental trEPR acquired at 10 K is reported. From the analysis of Figure 6.7 it is possible to appreciate how CISS effect affects the tr-EPR spectra, resulting in relevantly different features in the case of singlet or triplet initial states. Conversely, in the case of mixed singlet and triplet states the spectra do not significantly change introducing CISS effect in the ET process; both simulations reproduce almost perfectly the experimental spectra obtained on the QD-χ-C_{60} system. Even though these experimental and theoretical analyses do not allow to distinguish between a standard CT and a CISS-mediated CT, they do not exclude the occurrence of a spin filtering phenomenon during the process. To overcome this problem and clearly demonstrate the presence of CISS effect, a new dyad is needed featuring a larger separation between the initial excited singlet state and the triplet state, so as to avoid an initial ST mixed state. A larger splitting may be

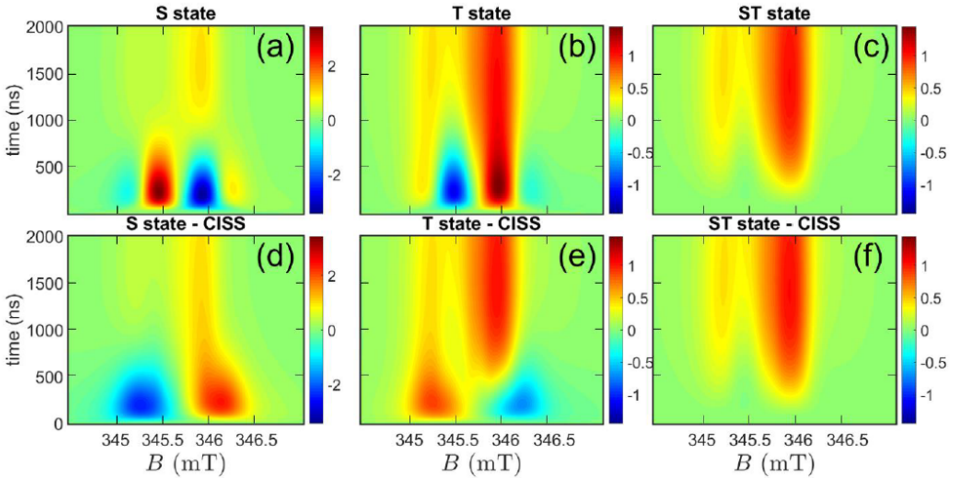

Figure 6.7: Panels (a,b,c): tr-EPR spectra simulated for S, T and ST initial states in absence of CISS effect. Panels (d,e,f): tr-EPR spectra simulated for S, T and ST initial states in presence of CISS effect. Reproduced from ref.[162]

achieved changing the size of the CdSe QDs or introducing a shell to increase the electron confinement.[177] An alternative solution could be represented by the engineering of a fully organic dyad where both the donor and the acceptor are organic moieties with well-defined energy states.

In conclusion the work illustrated in this chapter, even though not yet conclusive, shows a first promising attempt to observe photoinduced CISS effect through a direct spectroscopic investigation. A system comprising a CdSe QD as a donor and a C_{60} derivative as acceptor linked by a rigid chiral bridge has been assembled and chemically characterized by optical spectroscopy and XPS to confirm the correct assembly of the system. The results obtained by XPS characterization were fundamental to demonstrate unambiguously the achievement of

the desired nanostructured chiral system, therefore corroborating results obtained during the next phase of the work. A tr-EPR investigation has been performed to demonstrate that a photoinduced charge transfer generates a radical anion localized on the fullerene moiety, also showing a peculiar spin polarization evolution in the first μs after the laser irradiation. The tr-EPR signal has been then modeled considering both cases: a standard charge transfer and a CISS-mediated one. Simulations confirm that the experimental data could be compatible with the occurrence of CISS effect. Although several aspects must be modified to reach the perfect model in terms of charge transfer as well as of spin filtering efficiency, these results suggest that QD-χ-A dyads containing organic acceptors are very promising in the perspective of exploiting them as tools for the development of molecule-based quantum information processing. Indeed, this kind of systems could serve as building blocks of quantum computing architectures in which the spin polarization generated by CISS is used to initialize/readout qubits or implement quantum gates. Since with CISS effect it is possible to reach a high value of spin polarization at high temperature, this preliminary work could pave the way for room temperature operation of a molecular quantum processor.

7 | Conclusions and perspectives

The work carried out during the three years of this PhD period involved the preparation of chiral molecular deposits, and their characterization through the most widely used surface science techniques. The molecular building blocks were properly designed with the perspective to be used for the development of new quantum technologies based on Chirality Induced Spin Selectivity effect, which is deeply described in Chapter 3. I mostly focused my research activity on the characterization of three different systems (thia[4]helicene radical cation and its thioacetyl derivative both in neutral and radical cation forms) in terms of assembly on surface and spin selectivity properties. For the latter part I spent a visiting period at Weizmann Institute of Science in Israel where I had access to facilities that allowed me to perform electron transport measurements on the systems developed at the University of Florence. In the last period of my PhD, I started to investigate the behavior of a QD-χ-C_{60} dyad, a molecular spin selector candidate.
Many efforts of the scientific community in this field have been focused on gaining control over the spin state of electrons, and CISS

effect is representing a new fascinating and promising way. In this scenario, the main part of my project was concentrated on the synthesis and assembly on surface of compounds belonging to the class of thia[4]hetero helicene radical cations. These molecules meet all the requirements to be of great interest in the field of molecular spintronics as they feature several captivating properties: *i*) absence of heavy elements, thus low spin-orbit coupling, *ii*) chiral structure to induce CISS effect and *iii*) paramagnetic properties. Thus, the first part of the work focused on the development of a deposition procedure affording a monolayer of these chiral molecules, aiming to retain both their chiral structure and their paramagnetic properties after the assembly process. A thiophenol-templated Au(111) surface was chosen as substrate and a multi-step *wet chemistry* approach was adopted to induce the formation of a Self-Assembled Monolayer of helicenes on top of it. Subsequently, a comprehensive surface sensitive characterization of the sample was performed exploiting complementary techniques. Chemical characterization was carried out by performing XPS and ToF-SIMS studies, which confirmed the retention of chemical structure on surface and allowed to estimate the density of the sub-monolayer coverage. In addition, EPR measurements performed on the sub-monolayer sample, despite the presence of only a small amount of molecules (close to the sensitivity limit of the technique) detected a signal ascribable to the persistence of organic radicals on surface. Finally, X-ray Natural Circular Dichroism was observed at the carbon K-edge at the sub-monolayer level. This demonstrated unambiguously that chirality persists on surface and that no racemization occurs upon deposition of enantiopure radicals. This result represents a rare example of observation of X-ray Natural Circular Dichroism at the carbon edge on molecular assem-

blies. In summary, this study demonstrated for the very first time a successful attempt in depositing a chiral organic radical on surface.
In the second part of this thesis work, a novel synthetic procedure was developed to introduce a thioacetyl functional group in the helicene backbone. The idea was to obtain a more stable molecular system capable of forming covalent interactions between sulfur atoms and the metallic substrate with the aim of performing electron transport studies. Surface chemical investigation showed that molecules assembled on surface retain the expected composition. However, a partial degradation occurs during the deposition process since atomic sulfur is detectable on surface, because of the cleavage of C-S bonds. This behavior might be due to the solvent used for the deposition process or to the excessive length of the alkyl chain. Further improvements in this direction could be obtained by refining the method employed for depositing molecules. This might imply varying the incubation solvent, that strongly influences the dynamics and the final stability of the molecular deposits, as well as reducing the length of the carbon chain to minimize the degrees of freedom of molecules once packed in the monolayer. Despite the potential for improved performances, these molecules already proved to be very efficient as spin filters: high percentages of spin polarization were obtained by performing magnetic conductive AFM measurements. The unbalance in the spin population between the two enantiomers was found to be comparable with values observed with inorganic materials. In addition to this, CISS effect was observed in a surprisingly narrow applied potential window. On the other hand, CISS effect persists once molecules are embedded in a spintronic device, the spin polarization percentage decreases relevantly due to the inhomogeneity of the molecular monolayer with

respect to the punctual AFM measurement. Thus, in the perspective to develop a real molecular-based device, further studies are needed to improve the quality of the molecular deposit. In order to understand if the presence of paramagnetic species can influence the spin filtering process, an analogous study was carried out on the corresponding radical cation, obtained by performing a chemical oxidation on thioacetyl helicenes. At variance with the neutral compound, the radical cation assembles on surface without any detectable degradation, suggesting that the positive charge of the molecules plays a crucial role in guiding their organization at the monolayer level. Further, the results of mc-AFM characterization at room temperature were similar to those found investigating the neutral compound.

The only difference that can be traced back to the presence of unpaired electrons in the molecular deposit, is the higher electrical conductivity observed in the radical compared to the neutral form. Although the occurrence of CISS effect was detected and the active role of chiral molecules in the spin selectivity process was confirmed for the radical species, the use of a paramagnetic organic radical in place of neutral molecules provided almost the same spin polarization percentage, which is however very high and comparable with that obtained using inorganic materials. Preliminary results of magnetoresistance measurements, besides validating the presence of CISS effect, showed a slight difference in trend of magnetoresistance at low temperature between neutral and radical forms, in addition to a mildly higher percentage of magnetoresistance. However, these experimental observations are not sufficient to confirm that the paramagnetism is influencing the process. The higher spin polarization observed for the radical on surface might indeed be due to the better quality of the

molecular assembly with respect to the neutral species, as confirmed by XPS. Therefore, further experiments are planned to better understand if a layer of organic radicals is more suited to provide spin selectivity.
In the last part of the thesis, slightly deviating from the systems described above, the work was focused on the observation of CISS effect at the molecular level by studying a hybrid inorganic/organic dyad composed by a CdSe QD and a C_{60} fullerene connected by a chiral peptide bridge. After an extensive chemical characterization by optical measurements and XPS to confirm the correct assembly of the dyad, a tr-EPR study was carried out. This was aimed at observing the spin polarization arising in an electron transfer process with charges moving from the QD donor toward the fullerene acceptor through the chiral bridge. The spectroscopic characterization evidenced the arising of an EPR absorption signal ascribable to the radical anion formed on the C_{60} moiety. A deep theoretical investigation demonstrated that the experimental evidences of a radical anion signal arising from the electron transfer within the dyad could be consistent with a CISS mediated-electron transfer process.
In conclusion, the nanostructuration and the spin selectivity properties of several chiral molecules were presented. All the systems described in this thesis featured interesting properties both in terms of assembly on surface and spin filtering behavior.
In this scenario, in view of the promising results obtained with the systems studied in this thesis, there is plenty of room for improvement. As an example, the length of the alkyl chain can be modified to tune the interactions of the molecules with the surface and to improve the quality of the deposit. Further detailed studies are also necessary to properly investigate the role of paramagnetism coupled to CISS. On

the other hand, with regard to the chiral dyad, replacing the donor CdSe QD with an organic moiety (*e.g.* thia[4]helicene itself) would make it possible to unambiguously confirm the occurrence of CISS effect also in this kind of molecular system by avoiding the presence of a ST mixed initial state.

These investigations will be of interest for the scientific community working in the field of quantum computing and molecular spintronics, given the increasing attention devoted to CISS effect as a new tool for quantum technologies working at room temperature.

A | Appendix

Experimental synthetic procedure

All the solvents were dried according to standard procedures. Commercially available reagents were used as obtained from freshly opened containers without further purifications. Phtalimidesulfenyl chloride was prepared from the corresponding commercially available disulfide following the procedure reported in ref.[178] ^{1}H and ^{13}C-NMR spectra were recorded with Varian Mercury Plus 400, using $CDCl_3$ and CD_2Cl_2 as solvents. Residual $CHCl_3$ at $\delta = 7.26$ ppm and residual $CHDCl_2$ at $\delta = 5.32$ ppm were used as the reference of ^{1}H-NMR spectra. Central lines of $CDCl_3$ at $\delta = 77.00$ ppm and CD_2Cl_2 at $\delta = 54.00$ were used as the reference of ^{13}C-NMR spectra. FT-IR spectra were recorded with Spectrum Two FT-IR Spectrometer. ESI-MS spectra were recorded with a JEOL MStation JMS700. Melting points were measured with Stuart SMP50 Automatic Melting Point Apparatus. All the reactions were monitored and R_f was calculated by TLC on commercially available precoated plates (silica gel 60 F 254) and the products were visualized with acidic vanillin solution. Silica gel 60 (230–400 mesh) was used for column chromatography. Dry solvents were obtained by the

PureSolv Micro Solvent Purification System unless otherwise specified. Optical rotation measurements were performed on a JASCO DIP-370 polarimeter (JASCO, Easton, MD, USA) and the specific rotation of compounds was reported as follows: $[\alpha]\lambda$ (c (g/mL), solvent). UV spectra were obtained on a Varian Cary 50 UV-Vis spectrophotometer. The HPLC resolution was performed on a HPLC Waters Alliance 2695 equipped with a 200 μL loop injector and a spectrophotometer UV Waters PDA 2996 using HPLC grade solvents purchased from Merck. The semipreparative resolution was carried out on a CHIRALPAK®IG semipreparative column (250 x 10 mm/ 5μm) purchased from Chiral Technologies Europe. The mobile phase, delivered at a flow rate 3.5 mL/min, was hexane/CH_2Cl_2 70/30 v/v. Enantiomeric excess was measured on a CHIRALPAK®IA analytical column (250 x 4.6 mm/ 5 μm) purchased from Chiral Technologies Europe. The mobile phase, delivered at a flow rate 1.2 mL/min, was hexane/CH_2Cl_2 70/30 v/v. Elemental analysis was measured with a Thermoscientific FlashSmart Elemental Analyzer CHNS/O.

A.1 | Synthesis of thia[4]helicene radical cation

Synthesis of bis-*N*-thiophtalimide. Synthesis of this compound has been reproduced from ref.[118] To a solution of tri-*p*-tolylamine (1 eq.) in dry $CHCl_3$ under a nitrogen atmosphere, phthalimidesulfenyl chloride was added (2.3 eq.). After stirring at 60°C for 24 hours, the reaction mixture was diluted with CH_2Cl_2 (5 mL) and washed with

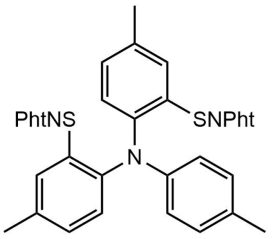

saturated $NaHCO_3$ solution and water. The organic layer was dried over Na_2SO_4, filtered, concentrated under reduced pressure and purified by flash chromatography (CH_2Cl_2/petroleum ether 4:1) to provide a yellow solid.

Synthesis of thia[4]helicene. Synthesis of this compound has been reproduced from ref.[118] To a solution of bis-*N*-thiophtalimide (1 eq.) in dry CH_2Cl_2 (50 mL) was added $BF_3 \cdot Et_2O$ (40 eq.) under nitrogen atmosphere. After stirring for 3 hours at room temperature, the mixture was diluted in CH_2Cl_2 and washed with saturated $NaHCO_3$ solution and a saturated NaF solution. The organic layer was dried over Na_2SO_4 and purified by flash chromatography (CH_2Cl_2/petroleum ether 1:2) to afford a white solid further purified by crystallization from $CHCl_3$.

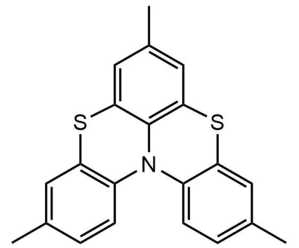

Synthesis of thia[4]helicene radical cation. Synthesis of this compound has been adapted from ref.[15] A solution of $AgSbF_6$ (1.3 eq.) in dry CH_2Cl_2 was added dropwise to a solution of thia[4]helicene (1 eq.) in dry CH_2Cl_2 at room temperature. The dark purple solution was stirred for 1 hour, filtered through a short pad of celite and washed several times with dry CH_2Cl_2. Solvent was removed under reduced pressure to give the thia[4]helicene radical cation in quantitative yield as a purple solid.

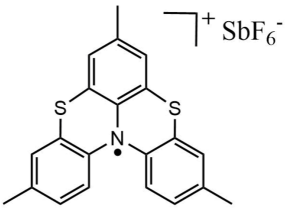

The product was purified by dissolving the crude material into a minimum amount of CH_2Cl_2 and adding hexane to induce the precipitation of the desire pure product.

A.2 | Synthesis of thioacetyl thia[4]helicene radical cation

Synthesis of 4-bromo-2-methoxy-1-methylbenzene.

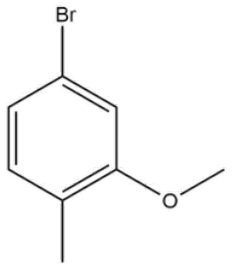

To a solution of K_2CO_3 (2 eq.) and 5-bromo-2-methylphenol (1 eq.) in dry dimethylformamide (DMF, 80 mL), MeI (2 eq.) was added under stirring at 75° C for 2.5 hours. Mixture was diluted with H_2O and washed with Et_2O, Na_2CO_3 and a saturated NaCl solution. The organic layer was dried over Na_2SO_4, filtered and concentrated under reduced pressure to afford a brownish oil.

Synthesis of 3,7-dimethyl-10H-phenothiazine.

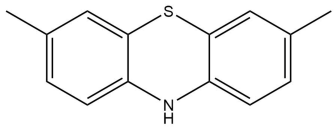

A solid state reaction involving di-*p*-tolylamine (1 eq.), elemental sulfur (2 eq.) and I_2 (cat.) is performed under stirring for 40 minutes at 170° C. After cooling the reaction mixture is diluted in CH_2Cl_2 and washed with H_2O. The organic layer is then concentrated under reduced pressure and purified by flash chromatography (CH_2Cl_2/petroleum ether 1:1) to afford a light brown solid.

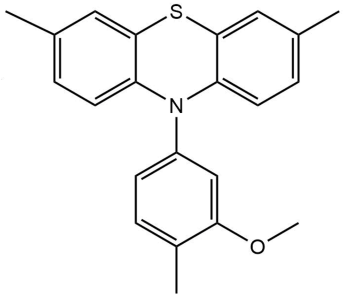

Synthesis of 10-(3-methoxy-4-methylphenyl)-3,7-dimethyl-10H-phenothiazine. Synthesis of this compound has been adapted from ref.[179] To a solution of 3,7-dimethyl-10H-phenothiazine (1 eq.), *xantphos* (cat.) and NaOtBu (1.5 eq.) in dry toluene, 4-bromo-2-methoxy-1-methylbenzene (1.1 eq.) was added under stirring. To the mixture $Pd(OAc)_2$ (cat.) was added and the solution was stirred under nitrogen at 100° C overnight. The solution was diluted with diethyl ether and washed with a saturated solution of NaCl. The organic layer was dried over Na_2SO_4, filtered, concentrated under reduced pressure and purified with flash chromatography (CH_2Cl_2/petroleum ether 1:3) to afford a dark green solid.

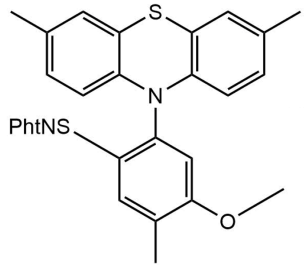

Synthesis of N-Thiophthalimide. Synthesis of this compound has been reproduced from ref.[180] To a solution of 10-(3-methoxy-4-methylphenyl)-3,7-dimethyl-10H-phenothiazine (1.15 eq.) in dry $CHCl_3$ was added a solution of phthalimidesulfenyl chloride (1.38 eq.) in dry $CHCl_3$ under nitrogen atmosphere at 0° C. After stirring at room temperature for 12 hours, the reaction mixture was diluted with CH_2Cl_2, washed with saturated solution of $NaHCO_3$ and water. The organic layer was dried over Na_2SO_4, filtered, concentrated under reduced pressure and purified with flash

chromatography (CH_2Cl_2/petroleum ether 1:1) to afford a pale yellow solid.

Synthesis of 2-methoxy-3,7,11-trimethylbenzo[5,6][1,4] thiazino [2,3,4-*kl*]phenothiazine. Synthesis of this compound has been reproduced from ref.[180] To a solution of N-thiophthalimide (1 eq.) in dry CH_2Cl_2, under a nitrogen atmosphere, $AlCl_3$ was added (2 eq.) at room temperature. The reaction mixture was kept under stirring and monitored by TLC until the starting material disappeared, diluted with CH_2Cl_2, washed with saturated Na_2CO_3 solution and water, filtered and concentrated under reduced pressure. The product was purified with flash chromatography (CH_2Cl_2/petroleum ether 1:10) to afford a pale brown solid.

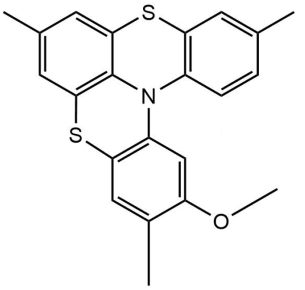

Synthesis of 3,7,11-trimethylbenzo [5,6][1,4]thiazino[2,3,4-*kl*]phenothia -zin-2-ol. Synthesis of this compound has been adapted from ref.[180] To a solution of 2-methoxy-3,7,11-trimethylbenzo [5,6][1,4]thiazino[2,3,4-*kl*]phenothiazine (1 eq.) in dry CH_2Cl_2 a 1 M solution of BBr_3 in dry CH_2Cl_2 (10 eq.) was added under a nitrogen atmosphere. The reaction mixture was stirred for 4 hours at room temperature then was

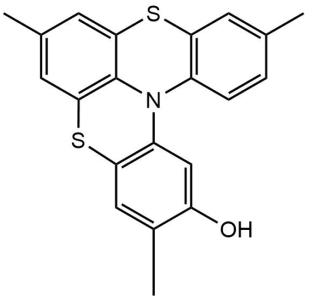

diluted with ethyl acetate, washed with water, dried over Na_2SO_4, filtered and concentrated under reduced pressure. The crude product was purified with flash chromatography (CH_2Cl_2/ethyl acetate 9:1) to afford a grey solid.

Synthesis of 3,7,11-trimethyl[1,4] benzothiazino[2,3,4-*kl*]phenothia zin-2-yl 16-bromohexadecanoate.

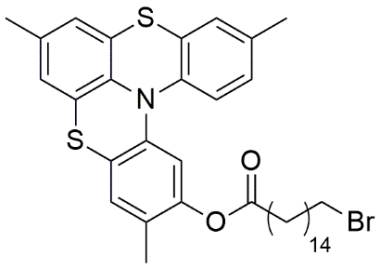

Synthesis of this compound has been developed during this thesis and will be published in the manuscript currently in preparation. A round bottom-flask was charged with: 3,7,11-trimethylbenzo[5,6][1,4]thiazino[2,3,4-*kl*]phenothiazin-2-ol (483 mg, 1.33 mmol), 16-bromohexadecanoic acid (16 mg, 0.13 mmol) and 4-(dimethylamino)pyridine (16 mg, 0.13 mmol). The solids were dissolved in 27 mL of dry CH_2Cl_2 and *N,N'*-diisopropylcarbodiimide (126 mg, 1.73 mmol) was added *via* a syringe. The solution was stirred overnight at room temperature under a nitrogen atmosphere. The suspension was diluted in ethyl acetate and washed with a saturated solution of $NaHCO_3$ (60 mL x 2) and water (60 mL). The organic layer was dried over Na_2SO_4, filtered and concentrated under reduce pressure. The crude material (1.0 g) was purified with flash chromatography (CH_2Cl_2/petroleum ether 1:2, R_f 0.50) to afford a white solid (830 mg, 92% yield). **mp** 74-76 °C. **IR (ATR solid)** ν = 2920 (C-H), 2851 (C-H), 1748 (C=O), 1490 (C=C), 1450 (C=C), 1313 (C-O), 1133 (C-O) cm^{-1}. **Anal. CHNS** for $C_{37}H_{46}BrNO_2S_2$: C, 65.28; H, 6.81; N, 2.06; S, 9.42. Found: C, 65.27; H, 6.86; N, 2.06; S, 9.47. **ESI-MS *m/z* (%)**: 702 (67), 704

(77) $[M + Na]^+$, 1382 (100) $[2M + Na]^+$. **^{1}H-NMR (400 MHz, CD_2Cl_2, δ)**: 7.06-7.09 (m, 2H; Ar H), 7.03 (bs, 1H; Ar H), 6.96 (dd, 1H J=8.2 Hz, J=2.0 Hz; Ar H) ppm 6.80-6.81 (m, 3H; Ar H), 3.43 (t, 2H, J=6.9 Hz, CH_2), 2.51 (t, 2H, J=7.6 Hz; CH_2), 2.29 (s, 3H; CH_3), 2.23 (s, 3H; CH_3), 2.11 (s, 3H, CH_3), 1.86 (2H, J= 7.4 Hz; CH_2), 1.70 (2H, J=7.3 Hz; CH_2), 1.28-1.45 (m, 22H; 11×CH_2), ppm. **^{13}C-NMR (100 MHz, CD_2Cl_2, δ)**: 172.2, 149.4, 142.0, 140.1, 137.4, 135.4, 135.2, 129.8, 128.8, 128.6, 127.2, 127.1, 126.6, 126.5, 125.8, 125.8, 124.2, 120.7, 114.4, 34.8, 34.6, 33.5, 30.21, 30.20 (2C), 30.15, 30.13, 30.03, 30.01, 29.8, 29.7, 29.4, 28.8, 25.5, 20.9, 20.7, 16.0, ppm.

Synthesis of 3,7,11-trimethyl[1,4] benzothiazino[2,3,4-kl]phenothia -zin-2-yl 16-(acetylthio)hexadeca -noate. Synthesis of this compound has been developed during this thesis and will be published in the manuscript currently in preparation. To a suspension of K_2CO_3 (73 mg, 0.53 mmol) in freshly distilled THF, thioacetic acid was added (40 mg, 0.53 mmol). The mixture was stirred for 30 minutes then helicene (300 mg, 0.44 mmol) was added and the reaction was stirred at room temperature for 30 hours under a nitrogen atmosphere. The reaction was diluted with 80 mL of ethyl acetate and washed with water (30 mL × 2). The organic layer was dried over Na_2SO_4, filtered and concentrated under reduced pressure to afford 280 mg of crude material. Purification by flash chromatography (CH_2Cl_2/petroleum ether 2:3, R_f 0.46) gave the product as a white solid (230 mg, 83%). **mp** 72-74 °C. **IR (ATR solid)** ν = 2922 (C-H), 2852 (C-H), 1757 (C=O), 1690

(C=O), 1486 (C=C), 1449 (C=C), 1133 (C-O)cm^{-1}. **Anal. CHNS** for $C_{39}H_{49}NO_3S_3$: C, 69.29; H, 7.31; N, 2.07; S, 14.23. Found: C, 69.26; H, 7.33; N, 2.10; S, 14.25. **ESI-MS *m/z* (%)**: 698 (59) $[M+Na]^+$ 1372 (100)$[2M+Na]^+$. **UV-Vis (CH_2Cl_2)**: $\lambda_{max}(\epsilon)$ = 314 nm (9172). **^{1}H-NMR (400 MHz, CD_2Cl_2, δ)**: 7.10 (d, 1H, J=8.2 Hz; Ar H), 7.02 (s, 1H; Ar H), 6.99 (bs, 1H; Ar H), 6.93 (dd, 1H, J=1.8 Hz, J=8.2 Hz; Ar H), 6.81 (s, 1H; Ar H), 6.76-6.77 (m, 2H, Ar H), 2.86 (t, 2H, J=7.4Hz, CH_2), 2.49 (t, 2H, J=7.6 Hz, CH_2), 2.32 (s, 3H, CH_3), 2.27 (s, 3H, CH_3) 2.20 (s, 3H, CH_3), 2.09 (s, 3H, CH_3), 1.71 (2H, J=7.6Hz; CH_2), 1.56 (2H, J=7.1 Hz; CH_2), 1.25-1.36 (m, 22H; 11 x CH_2), ppm. **^{13}C-NMR (100 MHz, CD_2Cl_2, δ)**: 196.2, 171.9, 148.8, 141.6, 139.8, 137.0, 134.7, 134.4, 129.4, 128.4, 128.2, 126.7, 126.4, 126.2, 126.1, 125.44, 125.37, 123.9, 120.3, 114.1, 34.3, 30.8, 29.76 (2C), 29.75, 29.70 (2C), 29.64, 29.61, 29.56, 29.4, 29.30 (2C), 29.26, 29.0, 25.1, 20.7, 20.5, 15.8, ppm.

Synthesis of 3,7,11 -trimethyl[1,4] benzothiazino [2,3,4-kl]phenothia -zin-2-yl 16-(acetyl -thio)hexadecanoate hexafluoroantimoniate radical cation.

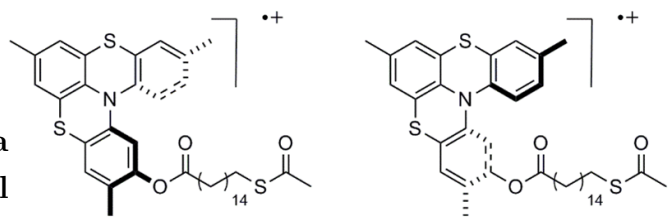

Synthesis of this compound has been developed during this thesis and will be published in the manuscript currently in preparation. To a solution of enantiopure neutral helicene (25 mg, 0.04 mmol) in 2 mL of dry CH_2Cl_2, $AgSbF_6$ (17 mg, 0,05 mmol) is added. The dark solution is stirred at room temperature for 1 hour, then filtered through a sintered glass funnel

and concentrated under reduced pressure. Dissolution of the crude material into a minimum amount of CH_2Cl_2 and addition of hexane led to the precipitation of the desired product as a dark blue solid (27 mg, 80%). **mp** 151-154 °C. **UV-Vis (CH_2Cl_2)**: $\lambda_{max}(\epsilon) = 573$ nm (8140), 396 nm (3150), 313 nm (15530). **Anal. CHNS** for $C_{39}H_{49}F_6NO_3S_3Sb$: C, 51.38; H, 5.42; N, 1.54; S, 10.55. Found: C, 51.40; H, 5.47; N, 1.58; S, 10.65.

B | Appendix

B.1 | Experimental section

Below all the experimental details about instrumentation and procedures will be reported.

XPS XPS experiments described in Chapter 4 and in Chapter 5 were performed using a micro-focused monochromatic Al K_α radiation source (1486.6 eV, model SPECS XR-MS Focus 600) and a multichannel detector electron analyzer (model SPECS Phoibos 150 1DLD) with a pass energy of 40 eV to ensure appropriate resolution. XPS experiments described in Chapter 6 were carried out using a non-monochromatized Mg K_α radiation (1253.6 eV) and a hemispherical electron/ion energy analyser VSW mounting a 16-channel detector. The operating parameters of the X-ray source were 12 kV and 12 mA. Spectra were acquired in a fixed analyser transmission mode with pass energy of 44.0 eV.
The spectra were measured in normal emission with the X-ray source mounted at 54.44° with respect to the analyzer. Spectra were deconvoluted using CasaXPS software with mixed Gaussian and Lorentzian

contributions for each component. The background was fitted using the Shirley or linear method.

ToF-SIMS ToF-SIMS characterization was performed at the University of Siena with a TRIFT III spectrometer (Physical Electronics, Chanhassen, MN) equipped with a gold liquid-metal primary ion source. Positive and negative ion spectra were acquired by rastering a pulsed, bunched 22 keV Au^+ primary ion beam over a 100 μm x 100 μm sample area maintaining static SIMS conditions. Positive-ion spectra were calibrated to $C_2H_5^+$ (m/z=29.039), $C_7H_8^+$ (m/z=92.063) and $C_7H_5S^+$(m/z = 121.011). Negative-ion spectra were calibrated to CH^- (m/z = 13.008), F^- (m/z = 18.998) and $C_6H_6^-$ (m/z = 78.047). Mass resolution ($m/\Delta m$) was up to $5 \cdot 10^3$ depending on the sample.

CW-EPR CW X-band EPR spectra were recorded on a Bruker Elexsys E500 spectrometer equipped with an SHQ cavity. EPR spectral simulations were performed using software EasySpin.[119]

tr-EPR All tr-EPR spectra were recorded on a Bruker Elexsys E580 Xband spectrometer equipped with a dielectric ring resonator (ER 4118X-MD5). The sample temperature was maintained using a helium gas-flow cryostat Oxford Instruments CF9350 and controlled with an Oxford Instruments ITC503. Laser excitation at different wavelengths was provided by a Litron AURORA II opto-parametric oscillator (OPO) tuneable laser (model number: A23-39-21, 21 Hz repetition rate, E/pulse $\sim$ 2 mJ, λ= 410–700 nm, pulse duration 7 ns). The laser beam was coupled into the resonator through an optical window. No effects of laser beam polarization are detected, which suggests the

laser beam is non-polarized at the sample position. tr-EPR experiments were performed by direct detection with the transient recorder without lock-in amplification. The instrument response time was about 200 ns. The spectra were acquired with 2 mW microwave power and averaging 100 transient signals at each field position. The magnetic field was measured with a Bruker ER035M NMR Gaussmeter. After data acquisition, baseline correction in both time and field dimensions was performed. The transient EPR spectrum at different time delays after the laser pulse was extracted from the corrected dataset. The reported tr-EPR spectra were averaged over a time window of 0.2 ms.

XNCD experiment XNCD experiments were performed in total electron yield (TEY)[181] detection mode at APE-HE beamline[182] at Elettra synchrotron. Samples were prepared inside a glovebox under N_2 atmosphere and transferred to the fast entry of the chamber via a UHV suitcase to avoid any contact with air and minimize atmospheric contamination. To remove the contribution of the adventitious carbon present in the beamline optical path, each signal was normalized by using a reference XAS at carbon K edge acquired on a freshly sputtered gold reference sample: each measurement has been repeated twice, first monitoring the I/I_0 on the real sample and then repeating the same measurement of the gold single crystal, then a ratio between the two spectra has been adopted as the final spectrum for each polarization. In that way, the obtained absorption signal is attributable only to the carbon atoms of the sample. XNCD spectrum has been evaluated as the difference between the cross sections measured using left and right circularly polarized light ($\sigma^L - \sigma^R$), by normalizing to 1 the average of the two XAS spectra at 290 eV (in the post edge energy region) and

taking into account the degree of circular polarization of about 95%.

STM STM measurements were carried out under UHV conditions at 30 K using a variable temperature (VT)-STM Omicron (model XA VT-STM) with Pt/Ir tip.

mc-AFM Substrates were prepared by e-beam evaporation depositing on a clean Si wafer an adlayer of Ti (10 nm) followed by Ni (100 nm) and Au (10 nm). The substrate was then cleaned by immersing it in boiling acetone for 10 minutes and in boiling ethanol for additional 10 minutes. Finally, the substrate was kept under UV/ozone atmosphere for 15 minutes. Mc-AFM experiment was performed using a multimode magnetic scanning probe microscopy (SPM) system equipped with Beetle type Ambient AFM and an electromagnet with R9 electronic controller (RHK Technology). *I-V* measurements were performed under ± 0.5 T magnetic field at room temperature applying voltage ramps between ± 0.3 V with a Pt coated tip (DPE-XSC11, μmasch) in contact mode (applied force ca. 8-10 nN). At least 150 curves were scanned for each point, several points were investigated all over the surface for a proper statistical analysis.

MR device fabrication Devices were fabricated by optical lithography followed by e-beam evaporation. On a pre-cleaned Si wafer 2 μm-wide Ti adlayer (8 nm) and Au (60 nm) were deposited by evaporation. The substrate was then cleaned by immersing it in boiling acetone for 10 minutes and in boiling ethanol for additional 10 minutes. Finally, the substrate was kept under UV/ozone atmosphere for 15 minutes. On top of gold layer, a self-assembled monolayer of

molecules was deposited following the procedure previously described. Finally, as top electrode, insulating buffer layer of MgO (2 nm), Ni (40 nm) and Au (20 nm) were evaporated using a shadow mask with a line width of 20 μm. The device was subsequently attached to a cryogenic chip carrier and electrically connected by wire bonder (Au wire). All electrical measurements were carried out within a cryogenics system made by Cryogenics, Ltd.. A magnetic field up to 1 T was applied perpendicular to the sample plane and the resistance of the device was measured using the standard four-probe method.[183] A constant current of 0.5 mA was applied using a Keithley current source (Model 2400) and the voltage across the junction was measured using a Keithley nanovoltmeter (Model 2182A).

Optical spectroscopy UV-Vis spectra were recorded at room temperature by using a Cary 5000 spectrophotometer (Agilent) in the range 400–800 nm. The PL spectra were measured at room temperature using an excitation wavelength (λ_{ex}) of 400 nm on a FluoroMax P (Horiba). The measurements were performed using quartz cuvettes with a path length of 1 cm. PL spectra were normalized for the optical density of the same solution at the maximum of the excitonic peak. Time-resolved photoluminescence (TRPL) measurements were carried out using the time-correlated single-photon counting (TCSPC) technique. The experimental apparatus is based on the FluoroMax P spectrofluorometer detection unit (grating monochromator and photomultiplier tube), powered by the FluoroHub Single Photon Counting unit. The excitation source was a blue pulsed Horiba NanoLED, generating picosecond pulses in the UV (375 nm). The instrument response function (IRF) for the whole apparatus was determined by means of

scattered light detection using a reference sample of LUDOX®colloidal silica. LED radiation was focused by means of a spherical lens on a sample holder, and sample emission was collected with a 90° geometry to minimize scattering interferences.

Bibliography

[1] Thompson, S. E. & Parthasarathy, S. Moore's law: the future of Si microelectronics. *Mater. Today* **9**, 20–25 (2006).

[2] Meindl, J. Beyond Moore's Law: the interconnect era. *Comput. Sci. Eng.* **5**, 20–24 (2003).

[3] Wolf, S. A. *et al.* Spintronics: A Spin-Based Electronics Vision for the Future. *Science* **294**, 1488–1495 (2001).

[4] Heinrich, A. J. *et al.* Quantum-coherent nanoscience. *Nat. Nanotechnol.* **16**, 1318–1329 (2021).

[5] Žutić, I., Fabian, J. & Das Sarma, S. Spintronics: Fundamentals and applications. *Rev. Mod. Phys.* **76**, 323–410 (2004).

[6] Thompson, S. M. The discovery, development and future of GMR: The Nobel Prize 2007. *J. Phys. D. Appl. Phys.* **41**, 093001 (2008).

[7] Sun, D., Ehrenfreund, E. & Valy Vardeny, Z. The first decade of organic spintronics research. *Chem. Comm.* **50**, 1781–1793 (2014).

[8] Dediu, V. A., Hueso, L. E., Bergenti, I. & Taliani, C. Spin routes in organic semiconductors. *Nat. Mater.* **8**, 707–716 (2009).

[9] Xiong, Z. H., Wu, D., Valy Vardeny, Z. & Shi, J. Giant magnetoresistance in organic spin-valves. *Nature* **427**, 821–824 (2004).

[10] Ray, K., Ananthavel, S. P., Waldeck, D. H. & Naaman, R. Asymmetric Scattering of Polarized Electrons by Organized Organic Films of Chiral Molecules. *Science* **283**, 814–816 (1999).

[11] Naaman, R., Paltiel, Y. & Waldeck, D. H. Chiral molecules and the electron spin. *Nat. Rev. Chem.* **3**, 250–260 (2019).

[12] Mondal, P. C., Mtangi, W. & Fontanesi, C. Chiro-Spintronics: Spin-Dependent Electrochemistry and Water Splitting Using Chiral Molecular Films. *Small Methods* **2**, 1700313 (2018).

[13] Aiello, C. D. *et al.* A Chirality-Based Quantum Leap. *ACS Nano* **16**, 4989–5035 (2022).

[14] Bloom, B. P., Waldeck, A. R. & Waldeck, D. H. Homochirality and chiral-induced spin selectivity: A new spin on the origin of life. *Proc. Natl. Acad. Sci.* **119** (2022).

[15] Menichetti, S. *et al.* Thia-bridged triarylamine heterohelicene radical cations as redox-driven molecular switches. *Chem. Comm.* **51**, 11452–11454 (2015).

[16] Kelvin, L. W. T. *Baltimore lectures on molecular dynamics and the wave theory of light* (CUP Archive, 1904).

[17] Brandt, J. R., Salerno, F. & Fuchter, M. J. The added value of small-molecule chirality in technological applications. *Nat. Rev. Chem.* **1**, 0045 (2017).

[18] Pasteur, L. Sur les relations qui peuvent exister entre la forme crystalline, la composition chimique et le sens de la polarization rotatoire. *Ann. Chim. Phys.* **24**, 442–459 (1848).

[19] Condon, E. U. Theories of Optical Rotatory Power. *Rev. Mod. Phys.* **9**, 432–457 (1937).

[20] Gal, J. Molecular Chirality in Chemistry and Biology: Historical Milestones. *Helv. Chim. Acta* **96**, 1617–1657 (2013).

[21] Bentley, R. Chirality in Biology. In *Encycl. Mol. Cell Biol. Mol. Med.* (Wiley-VCH Verlag GmbH & Co. KGaA, Weinheim, Germany, 2006).

[22] Barron, L. D. Symmetry and Chirality: Where Physics Shakes Hands with Chemistry and Biology. *Isr. J. Chem.* **61**, 517–529 (2021).

[23] Bonner, W. A. The origin and amplification of biomolecular chirality. *Orig. Life Evol. Biosph.* **21**, 59–111 (1991).

[24] Blackmond, D. G. The origin of biological homochirality. *Philos. Trans. R. Soc. B Biol. Sci.* **366**, 2878–2884 (2011).

[25] Chen, Y. & Ma, W. The origin of biological homochirality along with the origin of life. *PLoS Comput. Biol.* **16**, e1007592 (2020).

[26] Kim, J. H. & Scialli, A. R. Thalidomide: The Tragedy of Birth Defects and the Effective Treatment of Disease. *Toxicol. Sci.* **122**, 1–6 (2011).

[27] Ribó, J. M. Chirality: The Backbone of Chemistry as a Natural Science. *Symmetry* **12**, 1982 (2020).

[28] Sanchez, F. & Sobolev, K. Nanotechnology in concrete – A review. *Constr. Build. Mater.* **24**, 2060–2071 (2010).

[29] Li, Y. *et al.* Chiral Transition Metal Oxides: Synthesis, Chiral Origins, and Perspectives. *Adv. Mater.* **32**, 1905585 (2020).

[30] Hazen, R. M., Filley, T. R. & Goodfriend, G. A. Selective adsorption of L- and D-amino acids on calcite: Implications for biochemical homochirality. *Proc. Natl. Acad. Sci.* **98**, 5487–5490 (2001).

[31] McFadden, C. F., Cremer, P. S. & Gellman, A. J. Adsorption of Chiral Alcohols on "Chiral" Metal Surfaces. *Langmuir* **12**, 2483–2487 (1996).

[32] Sholl, D. S. Adsorption of Chiral Hydrocarbons on Chiral Platinum Surfaces. *Langmuir* **14**, 862–867 (1998).

[33] Baber, A. E., Gellman, A. J., Sholl, D. S. & Sykes, E. C. H. The Real Structure of Naturally Chiral Cu(643). *J. Phys. Chem. C* **112**, 11086–11089 (2008).

[34] Kosters, D. *et al.* Core–Shell Plasmonic Nanohelices. *ACS Photonics* **4**, 1858–1863 (2017).

[35] Gansel, J. K. *et al.* Gold Helix Photonic Metamaterial as Broadband Circular Polarizer. *Science* **325**, 1513–1515 (2009).

[36] Singh, M., Kaur, N. & Comini, E. The role of self-assembled monolayers in electronic devices. *J. Mater. Chem. C* **8**, 3938–3955 (2020).

[37] Vericat, C., Vela, M. E., Benitez, G., Carro, P. & Salvarezza, R. C. Self-assembled monolayers of thiols and dithiols on gold: new challenges for a well-known system. *Chem. Soc. Rev.* **39**, 1805 (2010).

[38] Arya, S. K., Solanki, P. R., Datta, M. & Malhotra, B. D. Recent advances in self-assembled monolayers based biomolecular electronic devices. *Biosens. Bioelectron.* **24**, 2810–2817 (2009).

[39] Ferretti, S., Paynter, S., Russell, D. A., Sapsford, K. E. & Richardson, D. J. Self-assembled monolayers: a versatile tool for the formulation of bio-surfaces. *TrAC Trends Anal. Chem.* **19**, 530–540 (2000).

[40] Cracknell, A. Tables of the irreducible representations of the 17 two-dimensional space groups and their relevance to quantum mechanical eigenstates for surfaces and thin films. *Thin Solid Films* **21**, 107–127 (1974).

[41] Chen, Q., Frankel, D. & Richardson, N. Chemisorption induced chirality: glycine on Cu. *Surf. Sci.* **497**, 37–46 (2002).

[42] Böhringer, M., Morgenstern, K., Schneider, W.-D. & Berndt, R. Separation of a Racemic Mixture of Two-Dimensional Molecular Clusters by Scanning Tunneling Microscopy. *Angew. Chem. Int. Ed.* **38**, 821–823 (1999).

[43] Atanasoska, L., Buchholz, J. & Somorjai, G. Low-energy electron diffraction study of the surface structures of adsorbed amino acid monolayers and ordered films deposited on copper crystal surfaces. *Surf. Sci.* **72**, 189–207 (1978).

[44] Fu, Y.-S. *et al.* Reversible Chiral Switching of Bis(phthalocyaninato) Terbium(III) on a Metal Surface. *Nano Lett.* **12**, 3931–3935 (2012).

[45] Krukowski, P. *et al.* Study of stereochemical crystallization of racemic mixtures of [5] and [7]thiaheterohelicene molecules on Ag(111) surface by scanning tunneling microscopy and Raman scattering spectroscopy. *Appl. Surf. Sci.* **589**, 152860 (2022).

[46] Parschau, M., Fasel, R. & Ernst, K.-H. Coverage and Enantiomeric Excess Dependent Enantiomorphism in Two-Dimensional Molecular Crystals. *Cryst. Growth Des.* **8**, 1890–1896 (2008).

[47] Seibel, J., Parschau, M. & Ernst, K.-H. Two-Dimensional Crystallization of Enantiopure and Racemic Heptahelicene on Ag(111) and Au(111). *J. Phys. Chem. C* **118**, 29135–29141 (2014).

[48] Balandina, T. *et al.* Self-assembly of an asymmetrically functionalized [6]helicene at liquid/solid interfaces. *Chem. Comm.* **49**, 2207 (2013).

[49] Tao, F. & Bernasek, S. L. Complexity in the Self-Assembly of Bifunctional Molecules on HOPG: The Influence of Solvent Functionality on Self-Assembled Structures. *Langmuir* **23**, 3513–3522 (2007).

[50] Kiran, V. *et al.* Helicenes-A New Class of Organic Spin Filter. *Adv. Mater.* **28**, 1957–1962 (2016).

[51] Naaman, R. & Waldeck, D. H. Chiral-Induced Spin Selectivity Effect. *J. Phys. Chem. Lett.* **3**, 2178–2187 (2012).

[52] Kox, A. J. The discovery of the electron: II. The Zeeman effect. *Eur. J. Phys.* **18**, 139–144 (1997).

[53] Cornia, A. & Seneor, P. The molecular way. *Nat. Mater.* **16**, 505–506 (2017).

[54] Ladd, T. D. *et al.* Quantum computers. *Nature* **464**, 45–53 (2010).

[55] Gaita-Ariño, A., Luis, F., Hill, S. & Coronado, E. Molecular spins for quantum computation. *Nat. Chem.* **11**, 301–309 (2019).

[56] Chappert, C., Fert, A. & Van Dau, F. N. The emergence of spin electronics in data storage. *Nat. Mater.* **6**, 813–823 (2007).

[57] Baibich, M. N. *et al.* Giant Magnetoresistance of (001)Fe/(001)Cr Magnetic Superlattices. *Phys. Rev. Lett.* **61**, 2472–2475 (1988).

[58] Yu, Z. G. Spin-Orbit Coupling, Spin Relaxation, and Spin Diffusion in Organic Solids. *Phys. Rev. Lett.* **106**, 106602 (2011).

[59] McClure, D. S. Spin Orbit Interaction in Aromatic Molecules. *J. Chem. Phys.* **20**, 682–686 (1952).

[60] Gunther, H. *NMR spectroscopy: basic principles, concepts, and applications in chemistry* (John Wiley & Sons, New York, 1995).

[61] Sanvito, S. Molecular spintronics. *Chem. Soc. Rev.* **40**, 3336 (2011).

[62] Poggini, L. *et al.* Nitronyl nitroxide radicals at the interface: a hybrid architecture for spintronics. *Rend. Lincei. Sci. Fis. e Nat.* **29**, 623–630 (2018).

[63] Cucinotta, G. *et al.* Tuning of a Vertical Spin Valve with a Monolayer of Single Molecule Magnets. *Adv. Funct. Mater.* **27**, 1703600 (2017).

[64] Poggini, L. *et al.* An Organic Spin Valve Embedding a Self-Assembled Monolayer of Organic Radicals. *Adv. Mater. Interfaces* **3**, 1500855 (2016).

[65] Pescia, D. & Meier, F. Spin polarized photoemission from gold using circularly polarized light. *Surf. Sci.* **117**, 302–309 (1982).

[66] Naaman, R. & Waldeck, D. H. Spintronics and Chirality: Spin Selectivity in Electron Transport Through Chiral Molecules. *Annu. Rev. Phys. Chem.* **66**, 263–281 (2015).

[67] Xie, Z. *et al.* Spin Specific Electron Conduction through DNA Oligomers. *Nano Lett.* **11**, 4652–4655 (2011).

[68] Lanza, M. *Conductive Atomic Force Microscopy: Applications in Nanomaterials* (2017).

[69] Bullard, G. *et al.* Low-Resistance Molecular Wires Propagate Spin-Polarized Currents. *J. Am. Chem. Soc.* **141**, 14707–14711 (2019).

[70] Tedrow, P. M. & Meservey, R. Spin Polarization of Electrons Tunneling from Films of Fe, Co, Ni, and Gd. *Phys. Rev. B* **7**, 318–326 (1973).

[71] Waldeck, D. H., Naaman, R. & Paltiel, Y. The spin selectivity effect in chiral materials. *APL Mater.* **9**, 040902 (2021).

[72] Sanvito, S. The rise of spinterface science. *Nat. Phys.* **6**, 562–564 (2010).

[73] Kulkarni, C. *et al.* Highly Efficient and Tunable Filtering of Electrons' Spin by Supramolecular Chirality of Nanofiber-Based Materials. *Adv. Mater.* **32**, 1904965 (2020).

[74] Mondal, A. K. *et al.* Long-Range Spin-Selective Transport in Chiral Metal–Organic Crystals with Temperature-Activated Magnetization. *ACS Nano* **14**, 16624–16633 (2020).

[75] Cuevas, J. C. & Scheer, E. The birth of molecular electronics. In *Mol. Electron.*, 3–18 (World Scientific, 2017).

[76] Gao, W. *et al.* Determining the adsorption energies of small molecules with the intrinsic properties of adsorbates and substrates. *Nat. Comm.* **11**, 1196 (2020).

[77] Jiang, G., Song, Y., Guo, X., Zhang, D. & Zhu, D. Organic Functional Molecules towards Information Processing and High-Density Information Storage. *Adv. Mater.* **20**, 2888–2898 (2008).

[78] Sanvito, S. Molecular spintronics. *Chem. Soc. Rev.* **40**, 3336 (2011).

[79] Rai, D. & Galperin, M. Electrically Driven Spin Currents in DNA. *J. Phys. Chem. C* **117**, 13730–13737 (2013).

[80] Suda, M. *et al.* Light-driven molecular switch for reconfigurable spin filters. *Nat. Comm.* **10**, 2455 (2019).

[81] Rodríguez, R. *et al.* Mutual Monomer Orientation To Bias the Supramolecular Polymerization of [6]Helicenes and the Resulting Circularly Polarized Light and Spin Filtering Properties. *J. Am. Chem. Soc.* **144**, 7709–7719 (2022).

[82] Varade, V. *et al.* Bacteriorhodopsin based non-magnetic spin filters for biomolecular spintronics. *Phys. Chem. Chem. Phys.* **20**, 1091–1097 (2018).

[83] Mathew, S. P., Mondal, P. C., Moshe, H., Mastai, Y. & Naaman, R. Non-magnetic organic/inorganic spin injector at room temperature. *Appl. Phys. Lett.* **105**, 242408 (2014).

[84] Bloom, B. P., Kiran, V., Varade, V., Naaman, R. & Waldeck, D. H. Spin Selective Charge Transport through Cysteine Capped CdSe Quantum Dots. *Nano Lett.* **16**, 4583–4589 (2016).

[85] Eckshtain-Levi, M. *et al.* Cold denaturation induces inversion of dipole and spin transfer in chiral peptide monolayers. *Nat. Comm.* **7**, 10744 (2016).

[86] Sang, Y. *et al.* Temperature Dependence of Charge and Spin Transfer in Azurin. *J. Phys. Chem. C* **125**, 9875–9883 (2021).

[87] Fransson, J. Vibrational origin of exchange splitting and chiral-induced spin selectivity. *Phys. Rev. B* **102**, 235416 (2020).

[88] Mishra, S. *et al.* Spin Filtering Along Chiral Polymers. *Angew. Chem. Int. Ed.* **59**, 14671–14676 (2020).

[89] Fontanesi, C. Spin-dependent electrochemistry: A novel paradigm. *Curr. Opin. Electrochem.* **7**, 36–41 (2018).

[90] Mondal, P. C., Fontanesi, C., Waldeck, D. H. & Naaman, R. Field and Chirality Effects on Electrochemical Charge Transfer Rates: Spin Dependent Electrochemistry. *ACS Nano* **9**, 3377–3384 (2015).

[91] Ghosh, K. B. *et al.* Controlling Chemical Selectivity in Electrocatalysis with Chiral CuO-Coated Electrodes. *J. Phys. Chem. C* **123**, 3024–3031 (2019).

[92] Deng, Y., Handoko, A. D., Du, Y., Xi, S. & Yeo, B. S. In Situ Raman Spectroscopy of Copper and Copper Oxide Surfaces during Electrochemical Oxygen Evolution Reaction: Identification of Cu III Oxides as Catalytically Active Species. *ACS Catal.* **6**, 2473–2481 (2016).

[93] Naaman, R. & Waldeck, D. H. Chiral-Induced Spin Selectivity Effect. *J. Phys. Chem. Lett.* **3**, 2178–2187 (2012).

[94] Winkler, R. *Spin-Orbit Coupling Effects in Two-Dimensional Electron and Hole Systems* (Springer, New York, 2003).

[95] Dianat, A. *et al.* Role of Exchange Interactions in the Magnetic Response and Intermolecular Recognition of Chiral Molecules. *Nano Lett.* **20**, 7077–7086 (2020).

[96] Maslyuk, V. V., Gutierrez, R., Dianat, A., Mujica, V. & Cuniberti, G. Enhanced Magnetoresistance in Chiral Molecular Junctions. *J. Phys. Chem. Lett.* **9**, 5453–5459 (2018).

[97] Yang, X., van der Wal, C. H. & van Wees, B. J. Detecting Chirality in Two-Terminal Electronic Nanodevices. *Nano Lett.* **20**, 6148–6154 (2020).

[98] Santos, J. I. *et al.* Chirality-Induced Electron Spin Polarization and Enantiospecific Response in Solid-State Cross-Polarization Nuclear Magnetic Resonance. *ACS Nano* **12**, 11426–11433 (2018).

[99] Varela, S., Mujica, V. & Medina, E. Effective spin-orbit couplings in an analytical tight-binding model of DNA: Spin filtering and chiral spin transport. *Phys. Rev. B* **93**, 155436 (2016).

[100] Matityahu, S., Utsumi, Y., Aharony, A., Entin-Wohlman, O. & Balseiro, C. A. Spin-dependent transport through a chiral molecule in the presence of spin-orbit interaction and nonunitary effects. *Phys. Rev. B* **93**, 075407 (2016).

[101] Geyer, M., Gutierrez, R. & Cuniberti, G. Effective Hamiltonian model for helically constrained quantum systems within adiabatic perturbation theory: Application to the chirality-induced spin selectivity (CISS) effect. *J. Chem. Phys.* **152**, 214105 (2020).

[102] Rosenberg, R. A. *et al.* Kinetic Energy Dependence of Spin Filtering of Electrons Transmitted through Organized Layers of DNA. *J. Phys. Chem. C* **117**, 22307–22313 (2013).

[103] Medina, E., González-Arraga, L. A., Finkelstein-Shapiro, D., Berche, B. & Mujica, V. Continuum model for chiral induced spin selectivity in helical molecules. *J. Chem. Phys.* **142**, 194308 (2015).

[104] Nolting, C., Mayer, S. & Kessler, J. Electron dichroism - new data and an experimental cross-check. *J. Phys. B At. Mol. Opt. Phys.* **30**, 5491–5499 (1997).

[105] Medina, E., López, F., Ratner, M. A. & Mujica, V. Chiral molecular films as electron polarizers and polarization modulators. *EPL* **99**, 17006 (2012).

[106] Dianat, A. *et al.* Role of Exchange Interactions in the Magnetic Response and Intermolecular Recognition of Chiral Molecules. *Nano Lett.* **20**, 7077–7086 (2020).

[107] Liu, Y., Xiao, J., Koo, J. & Yan, B. Chirality-driven topological electronic structure of DNA-like materials. *Nat. Mater.* **20**, 638–644 (2021).

[108] Alwan, S. & Dubi, Y. Spinterface Origin for the Chirality-Induced Spin-Selectivity Effect. *J. Am. Chem. Soc.* **143**, 14235–14241 (2021).

[109] Ji, L., Shi, J., Wei, J., Yu, T. & Huang, W. Air-Stable Organic Radicals: New-Generation Materials for Flexible Electronics? *Adv. Mater.* **32**, 1908015 (2020).

[110] Ratera, I. & Veciana, J. Playing with organic radicals as building blocks for functional molecular materials. *Chem. Soc. Rev.* **41**, 303–349 (2012).

[111] Herrmann, C., Solomon, G. C. & Ratner, M. A. Organic Radicals As Spin Filters. *J. Am. Chem. Soc.* **132**, 3682–3684 (2010).

[112] Poggini, L. *et al.* An Organic Spin Valve Embedding a Self-Assembled Monolayer of Organic Radicals. *Adv. Mater. Interfaces* **3**, 1500855 (2016).

[113] Raman, K. V. *et al.* Interface-engineered templates for molecular spin memory devices. *Nature* **493**, 509–513 (2013).

[114] Bajaj, A., Kaur, P., Sud, A., Berritta, M. & Ali, M. E. Anomalous Effect of Quantum Interference in Organic Spin Filters. *J. Phys. Chem. C* **124**, 24361–24371 (2020).

[115] Bajaj, A. & Ali, M. E. Tuning of spin-polarized current in high spin organic molecules. *Phys. B Condens. Matter* **595**, 412396 (2020).

[116] Smeu, M., Monti, O. L. A. & McGrath, D. Phenalenyls as tunable excellent molecular conductors and switchable spin filters. *Phys. Chem. Chem. Phys.* **23**, 24106–24110 (2021).

[117] Giaconi, N. *et al.* Stabilization of an Enantiopure Sub-monolayer of Helicene Radical Cations on a Au(111) Surface through Noncovalent Interactions. *Angew. Chem. Int. Ed.* **60**, 15276–15280 (2021).

[118] Lamanna, G. *et al.* Efficient Thia-Bridged Triarylamine Heterohelicenes: Synthesis, Resolution, and Absolute Configuration Determination. *Chem. Eur. J.* **14**, 5747–5750 (2008).

[119] Stoll, S. & Schweiger, A. EasySpin, a comprehensive software package for spectral simulation and analysis in EPR. *J. Magn. Reson.* **178**, 42–55 (2006).

[120] Yang, Y. & Wang, C. Hierarchical construction of self-assembled low-dimensional molecular architectures observed by using scanning tunneling microscopy. *Chem. Soc. Rev.* **38**, 2576 (2009).

[121] Love, J. C., Estroff, L. A., Kriebel, J. K., Nuzzo, R. G. & Whitesides, G. M. Self-Assembled Monolayers of Thiolates on Metals as a Form of Nanotechnology. *Chem. Rev.* **105**, 1103–1170 (2005).

[122] Dishner, M. H., Ivey, M. M., Gorer, S., Hemminger, J. C. & Feher, F. J. Preparation of gold thin films by epitaxial growth on mica and the effect of flame annealing. *J. Vac. Sci. Technol. A Vacuum, Surfaces, Film.* **16**, 3295–3300 (1998).

[123] Moro, F. *et al.* Electronic and Magnetic Properties of Mn_{12} Molecular Magnets on Sulfonate and Carboxylic Acid Prefunctionalized Gold Surfaces. *J. Phys. Chem. C* **116**, 14936–14942 (2012).

[124] Wan, L.-J., Terashima, M., Noda, H. & Osawa, M. Molecular Orientation and Ordered Structure of Benzenethiol Adsorbed on Gold(111). *J. Phys. Chem. B* **104**, 3563–3569 (2000).

[125] Abb, S., Savu, S.-A., Caneschi, A., Chassé, T. & Casu, M. B. Paramagnetic Nitronyl Nitroxide Radicals on Al_2O_3(11–20) Single Crystals: Nanoscale Assembly, Morphology, Electronic Structure, And Paramagnetic Character toward Future Applications. *ACS Appl. Mater. Interfaces* **5**, 13006–13011 (2013).

[126] Mannini, M. *et al.* Self-Assembled Organic Radicals on Au(111) Surfaces: A Combined ToF-SIMS, STM, and ESR Study. *Langmuir* **23**, 2389–2397 (2007).

[127] Auditore, A. *et al.* ToF-SIMS investigation of functional mixed aromatic thiol monolayers on gold. *Appl. Surf. Sci.* **231-232**, 314–317 (2004).

[128] Lloveras, V., Badetti, E., Veciana, J. & Vidal-Gancedo, J. Dynamics of intramolecular spin exchange interaction of a nitronyl nitroxide diradical in solution and on surfaces. *Nanoscale* **8**, 5049–5058 (2016).

[129] Longhi, G. *et al.* Chiroptical properties of the ground and excited states of two thia-bridged triarylamine heterohelicenes. *J. Photochem. Photobiol. A* **331**, 138–145 (2016).

[130] Zhang, Y., Rouxel, J. R., Autschbach, J., Govind, N. & Mukamel, S. X-ray circular dichroism signals: a unique probe of local molecular chirality. *Chem. Sci.* **8**, 5969–5978 (2017).

[131] Turchini, S. *et al.* Core Electron Transitions as a Probe for Molecular Chirality: Natural Circular Dichroism at the Carbon K-edge of Methyloxirane. *J. Am. Chem. Soc.* **126**, 4532–4533 (2004).

[132] Dor, O. B., Yochelis, S., Ohldag, H. & Paltiel, Y. Optical Chiral Induced Spin Selectivity XMCD Study. *Chimia* **72**, 379 (2018).

[133] Heravi, M. M., Kheilkordi, Z., Zadsirjan, V., Heydari, M. & Malmir, M. Buchwald-Hartwig reaction: An overview. *J. Organomet. Chem.* **861**, 17–104 (2018).

[134] Lupi, M. *et al.* Resolution of a Configurationally Stable Hetero[4]helicene. *Molecules* **27**, 1160 (2022).

[135] Narasimhan, S. & Vanderbilt, D. Elastic stress domains and the herringbone reconstruction on Au(111). *Phys. Rev. Lett.* **69**, 1564–1567 (1992).

[136] Edinger, K., Goelzhaeuser, A., Demota, K., Woell, C. & Grunze, M. Formation of self-assembled monolayers of n-alkanethiols on gold: a scanning tunneling microscopy study on the modification of substrate morphology. *Langmuir* **9**, 4–8 (1993).

[137] Yim, K.-H. *et al.* Phase-Separated Thin Film Structures for Efficient Polymer Blend Light-Emitting Diodes. *Nano Lett.* **10**, 385–392 (2010).

[138] Atzori, M. *et al.* Thermal and light-induced spin transition in a nanometric film of a new high-vacuum processable spin crossover complex. *J. Mater. Chem. C* **6**, 8885–8889 (2018).

[139] Distefano, G. *et al.* Intense shake-up satellites in the XPS spectra of planar and sterically hindered N-piperidyl-nitrobenzenes and -nitrothiophens. *Chem. Phys.* **72**, 267–279 (1982).

[140] Deleuze, M. S. Valence one-electron and shake-up ionization bands of polycyclic aromatic hydrocarbons. II. Azulene, phenanthrene, pyrene, chrysene, triphenylene, and perylene. *J. Chem. Phys.* **116**, 7012–7026 (2002).

[141] Jiang, T. *et al.* Thiophene Derivatives on Gold and Molecular Dissociation Processes. *J. Phys. Chem. C* **121**, 27923–27935 (2017).

[142] Whelan, C. M., Smyth, M. R., Barnes, C. J., Brown, N. M. & Anderson, C. A. An XPS study of heterocyclic thiol self-assembly on Au(111). *Appl. Surf. Sci.* **134**, 144–158 (1998).

[143] Cometto, F. P. *et al.* Decomposition of Methylthiolate Monolayers on Au(111) Prepared from Dimethyl Disulfide in Solution Phase. *J. Phys. Chem. C* **114**, 10183–10194 (2010).

[144] Bullard, G. *et al.* Low-Resistance Molecular Wires Propagate Spin-Polarized Currents. *J. Am. Chem. Soc.* **141**, 14707–14711 (2019).

[145] Kettner, M. *et al.* Chirality-Dependent Electron Spin Filtering by Molecular Monolayers of Helicenes. *J. Phys. Chem. Lett.* **9**, 2025–2030 (2018).

[146] Evers, F. *et al.* Theory of Chirality Induced Spin Selectivity: Progress and Challenges. *Adv. Mater.* **34**, 2106629 (2022).

[147] Pan, T.-R., Guo, A.-M. & Sun, Q.-F. Spin-polarized electron transport through helicene molecular junctions. *Phys. Rev. B* **94**, 235448 (2016).

[148] Göhler, B. *et al.* Spin Selectivity in Electron Transmission Through Self-Assembled Monolayers of Double-Stranded DNA. *Science* **331**, 894–897 (2011).

[149] Kiran, V., Cohen, S. R. & Naaman, R. Structure dependent spin selectivity in electron transport through oligopeptides. *J. Chem. Phys.* **146**, 092302 (2017).

[150] Das, T. K., Tassinari, F., Naaman, R. & Fransson, J. Temperature-Dependent Chiral-Induced Spin Selectivity Effect: Experiments and Theory. *J. Phys. Chem. C* **126**, 3257–3264 (2022).

[151] Fransson, J. Charge Redistribution and Spin Polarization Driven by Correlation Induced Electron Exchange in Chiral Molecules. *Nano Lett.* **21**, 3026–3032 (2021).

[152] Chen, X., Wang, X. & Fang, D. A review on C1s XPS-spectra for some kinds of carbon materials. *Fuller. Nanotub.* **28**, 1048–1058 (2020).

[153] Rieß, J. *et al.* XPS studies on dispersed and immobilised carbon nitrides used for dye degradation. *Photochem. Photobiol. Sci.* **18**, 1833–1839 (2019).

[154] Joyner, R. W. & Lincoln Vogel, F. X-ray photoelectron spectroscopy studies of SbF_5 intercalated graphite. *Synth. Met.* **4**, 85–90 (1981).

[155] Poneti, G. *et al.* Thermal and optical control of electronic states in a single layer of switchable paramagnetic molecules. *Chem. Sci.* **6**, 2268–2274 (2015).

[156] Torres-Cavanillas, R. *et al.* Reinforced Room-Temperature Spin Filtering in Chiral Paramagnetic Metallopeptides. *J. Am. Chem. Soc.* **142**, 17572–17580 (2020).

[157] Saito, G. & Yoshida, Y. Development of Conductive Organic Molecular Assemblies: Organic Metals, Superconductors, and Exotic Functional Materials. *Bull. Chem. Soc. Jpn.* **80**, 1–137 (2007).

[158] Abendroth, J. M. *et al.* Spin Selectivity in Photoinduced Charge-Transfer Mediated by Chiral Molecules. *ACS Nano* **13**, 4928–4946 (2019).

[159] Fay, T. P. & Limmer, D. T. Origin of Chirality Induced Spin Selectivity in Photoinduced Electron Transfer. *Nano Lett.* **21**, 6696–6702 (2021).

[160] Matxain, J. M. *et al.* Chirality Induced Spin Selectivity of Photoexcited Electrons in Carbon-Sulfur [n]Helicenes. *ChemPhotoChem* **3**, 770–777 (2019).

[161] Morris-Cohen, A. J., Donakowski, M. D., Knowles, K. E. & Weiss, E. A. The Effect of a Common Purification Procedure on the Chemical Composition of the Surfaces of CdSe Quantum Dots Synthesized with Trioctylphosphine Oxide. *J. Phys. Chem. C* **114**, 897–906 (2010).

[162] Privitera, A. *et al.* Direct detection of spin polarization in photoinduced charge transfer through a chiral bridge. *Chem. Sci.* **13**, 12208–12218 (2022).

[163] Dai, Q. *et al.* Facile synthesis of magic-sized CdSe and CdTe nanocrystals with tunable existence periods. *Nanotechnology* **18**, 405603 (2007).

[164] Tomasini, C., Luppi, G. & Monari, M. Oxazolidin-2-one-Containing Pseudopeptides That Fold into β-Bend Ribbon Spirals. *J. Am. Chem. Soc.* **128**, 2410–2420 (2006).

[165] Kordatos, K. *et al.* Novel Versatile Fullerene Synthons. *J. Org. Chem.* **66**, 4915–4920 (2001).

[166] Kicsák, M. *et al.* A three-component reagent system for rapid and mild removal of O-, N- and S-trityl protecting groups. *Org. Biomol. Chem.* **14**, 3190–3192 (2016).

[167] Jasieniak, J., Califano, M. & Watkins, S. E. Size-Dependent Valence and Conduction Band-Edge Energies of Semiconductor Nanocrystals. *ACS Nano* **5**, 5888–5902 (2011).

[168] Karakawa, M., Nagai, T., Adachi, K., Ie, Y. & Aso, Y. Precise control over reduction potential of fulleropyrrolidines for organic photovoltaic materials. *RSC Adv.* **7**, 7122–7129 (2017).

[169] Wuister, S. F., de Mello Donegá, C. & Meijerink, A. Influence of Thiol Capping on the Exciton Luminescence and Decay Kinetics of CdTe and CdSe Quantum Dots. *J. Phys. Chem. B* **108**, 17393–17397 (2004).

[170] Vasquez, R. P., Brain, R. A., Ross, D. & Yeh, N.-C. Epitaxial C_{60} Film on Si(111) by XPS. *Surf. Sci. Spectra* **1**, 242–245 (1992).

[171] Keller, A. *et al.* Tuning the hydrophobicity of mica surfaces by hyperthermal Ar ion irradiation. *J. Chem. Phys.* **134**, 104705 (2011).

[172] Lau, K. H. A., Huang, C., Yakovlev, N., Chen, Z. K. & O'Shea, S. J. Direct Adsorption and Monolayer Self-Assembly of Acetyl-Protected Dithiols. *Langmuir* **22**, 2968–2971 (2006).

[173] Tour, J. M. *et al.* Self-Assembled Monolayers and Multilayers of Conjugated Thiols, .alpha.,.omega.-Dithiols, and Thioacetyl-Containing Adsorbates. Understanding Attachments between Potential Molecular Wires and Gold Surfaces. *J. Am. Chem. Soc.* **117**, 9529–9534 (1995).

[174] Ospina, R., Rincón-Ortiz, S. A. & Rodriguez-Pereira, J. Cadmium selenide by XPS. *Surf. Sci. Spectra* **27**, 014021 (2020).

[175] Liu, S., Zhang, X., Yu, Y. & Zou, G. Bandgap engineered and high monochromatic electrochemiluminescence from dual-stabilizers-capped CdSe nanocrystals with practical application potential. *Biosens. Bioelectron.* **55**, 203–208 (2014).

[176] Righetto, M. *et al.* Engineering interactions in QDs–PCBM blends: a surface chemistry approach. *Nanoscale* **10**, 11913–11922 (2018).

[177] Olshansky, J. H. *et al.* Using Photoexcited Core/Shell Quantum Dots To Spin Polarize Appended Radical Qubits. *J. Am. Chem. Soc.* **142**, 13590–13597 (2020).

[178] Viglianisi, C. *et al.* Regioselective Electrophilic Access to Naphtho[1,2-b:8,7-b]- and -[1,2-b:5,6-b]dithiophenes. *J. Org. Chem.* **78**, 3496–3502 (2013).

[179] Dahl, T., Tornøe, C. W., Bang-Andersen, B., Nielsen, P. & Jørgensen, M. Palladium-Catalyzed Three-Component Approach to Promazine with Formation of One Carbon–Sulfur and Two Carbon–Nitrogen Bonds. *Angew. Chem. Int. Ed.* **47**, 1726–1728 (2008).

[180] Menichetti, S. *et al.* Thia-Bridged Triarylamine Hetero[4]Helicenes: Regioselective Synthesis and Functionalization. *Eur. J. Org. Chem.* **2019**, 168–175 (2019).

[181] Henke, B. L., Liesegang, J. & Smith, S. D. Soft-x-ray-induced secondary-electron emission from semiconductors and insulators: Models and measurements. *Phys. Rev. B* **19**, 3004–3021 (1979).

[182] Panaccione, G. *et al.* Advanced photoelectric effect experiment beamline at Elettra: A surface science laboratory coupled with Synchrotron Radiation. *Rev. Sci. Instrum.* **80**, 043105 (2009).

[183] Schroder, D. K. *Semiconductor Material and Device Characterization* (2006).

Acknowledgements

This thesis is the result of the contribution of many people that during these three years were involved in these projects. I would like to express my deep gratitude to all of them for their support and their help.

First and foremost, I would like to express my sincere gratitude to Professor Matteo Mannini, my supervisor, for his invaluable guidance, unwavering support, and visionary insights, without which the completion of this thesis would not have been possible. I am truly grateful for his ability to inspire me and cultivate my appreciation for scientific research.

I would also like to extend my heartfelt appreciation to Dr. Lorenzo Poggini for his moral and scientific support throughout my research. Our numerous discussions and exchange of ideas have significantly contributed to my work.

Furthermore, I would like to acknowledge Prof. Lorenzo Sorace, Prof. Andrea Caneschi, and Prof. Roberta Sessoli. It was an enormous privilege to work and learn under their guidance.

I want also to thank the entire outstanding team of LaMM for not only providing me with periods of hard work but also for offering me

moments of pure enjoyment. A special acknowledgment goes to Fabio and Sorre; you have become friends, more than colleagues.
Thanks also to Prof. Stefano Menichetti, Dr. Caterina Viglianisi and Michela Lupi that helped me with the synthesis of the helicene molecules that I studied in my research.
I cannot forget my family and my old friends who supported me at every stage of this path, supporting me when I needed to and encouraging me when I encountered difficulties. You have been a source of strength and motivation for me.
Finally, I dedicate a special thought to my love, Elisa, I met you halfway through this journey, but you have been the person who has best understood and supported me during difficult times. Thank you for being by my side and for making each of these days more serene.

Florence, March 2023

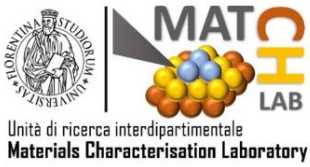
MAT
CH
LAB
Unità di ricerca interdipartimentale
Materials Characterisation Laboratory


LaMM
Laboratorio di Magnetismo Molecolare


FLORENTINA STUDIORUM UNIVERSITAS


iCCOM
ISTITUTO DI CHIMICA DEI COMPOSTI ORGANOMETALLICI
Consiglio Nazionale delle Ricerche

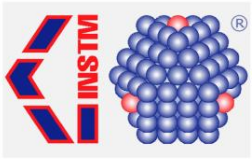
INSTM